UNIVERSITÀ DEGLI STUDI DI PADOVA

UNIVERSITÀ DEGLI STUDI DI PADOVA

Dipartimento di Ingegneria Industriale DII

Corso di Laurea Magistrale in Ingegneria dell'Energia Elettrica

Performance Analysis of Electric Drives using Slotless Motors

Relatori:
Prof. Nicola Bianchi
Prof. Marta Molinas -NTNU-

Correlatore:
Ravindra Babu Ummaneni
-Principal Electrical Engineer at
Alva Motor Solutions-

Studente:
Matteo Leandro
1154957

Anno accademico 2018/2019

Contents

1 Introduction **1**

2 Slotted and Slot-less PM Machines **3**

2.1 Slotted PM Machines Operating Characteristics 4

2.1.1 Fundamentals of Electromagnetic Torque Generation 4

2.2 Slot-less PM Machines Characteristics and Operation 9

2.2.1 Slot-less Machine Operation 10

3 Permanent Magnet Synchronous and Brush-less DC Motor Drives **13**

3.1 PM Brush-less DC Motor Drive 14

3.2 PM Synchronous Motor Drive 17

3.3 Power Electronics and Inverter Modelòing Assumptions 18

3.3.1 Fundamental on Switching Dynamics 18

3.3.2 Wide-bandgap Semiconductor Potentials 20

4 Alva Prototype (*Thor*) **21**

4.1 Double air-gap topology 21

4.2 Stator configuration 22

4.3 Halbach array pattern 23

4.4 System data 25

5 Permanent Magnet Brush-less DC Machine Drive Modelling **27**

5.1 Permanent Magnet BLDC motor modelling 28

5.2 Design of Current and Speed Controllers 34

5.2.1 System Identification in the Laplace Domain 34
5.2.2 Anti wind-up system 44
5.3 MATLAB-Simulink® Implementation -*PWM Trapezoidal Control*- . . . 46
5.3.1 Simulation Results of the BLDC Drive System 49

6 PM Synchronous Motor Drives Modelling **53**
6.1 Permanent Magnet Synchronous Motor Modelling 53
6.2 PMSM Model in a Rotating Reference System 55
6.2.1 PI Controllers Design in the *dq* System 56
6.3 MATLAB-Simulink® Implementation -*PMSM Space Vector Modulation*- 58
6.3.1 Simulation Results of the PMSM Drive System 60

7 Finite Element Loss Analysis With non-Sinusoidal Current **65**
7.0.1 Results from the Loss Analysis 67

8 Experimental Validation **71**

9 Conclusions **77**

A Air-gap flux density for surface-mounted permanent magnets **81**

B Air-gap flux density for Halbach array arrangement **83**

C *Clarke* transformation **87**

D *Park* transformation **89**

Chapter 1

Introduction

The growing idea of going towards a massive electrification, starting from industrial processes down to household applications and daily needs involving energy consumption, has been of a paramount concern for reducing the CO_2 emissions. In this regard, requiring high efficiency solutions on both power generation and power consumption sides, plays a crucial role. Being electric motors and generators a fundamental part in the aforementioned two applications, the high efficiency demand has been introducing many challenges when designing a rotating electrical machine, especially if a cost-effective solution needs to be achieved. The latter point, along with the common slotted topology of electrical machines, have led to a general standardisation of the whole production process, and thus to a low flexibility in terms of final solution.
Having a technology which is capable of providing high flexibility solutions, could make a difference in all those projects where the feasibility analysis fails because of the absence of an optimal solution in the electrical machine side.
Within this wide context, *Alva Motor Solutions* has commenced the development of a novel technology in the stator production phase. In its first iteration, this process allows the production of slot-less stators with a high flexibility in terms of final winding configuration. The innovative stator production process is accompanied by the all different stages involved in the production process of an electrical machine, starting from the electromagnetic and mechanical design, up to the different stages to get the final assembly according to the initial specifications. Nonetheless, the interest for *Alva* in delivering the best solution depending on the application, led the group to investigate and troubleshoot any issue related to the control of these electrical machines when fed by a power converter.
In so far as electric motors and generators are called to operate in wide speed ranges, a typical system configuration shows the electrical machine coupled either to a power source or a load by means of a power converter. This means that the overall system must be considered when evaluating the performance of the electric machine itself. In most of the cases, the type of converter to be used can be conveniently chosen in order to match the performance of the machine. However, in other cases, some different solutions need to be adopted, when technological limitations occur on the power converter side.
The aim of this work, is firstly to highlight the main differences between slotted and slot-less machines in order to highlight the reason why more care should be taken when dealing with the control of slot-less machines. Furthermore, the work proposes a solu-

tion for analysing the performance of an electric machine when controlled by means of a power inverter; the method follows the idea of the so called "circuit-coupled Finite Element Analysis (FEA)" of electrical machines, which is already implemented in some commercial software. This "framework" has been developed in such a way that it could be completely automated by linking the different steps of the analysis (design of the controllers, switching algorithm to be used, FEA). Different solutions for improving the system efficiency are presented along with simulation and experimental results which are conveniently compared for validating the framework.

Chapter 2

Slotted and Slot-less PM Machines

The adoption of permanent magnet (PM) brush-less machines is becoming the first choice among all the different topology when high efficiency represents the paramount concern in terms of initial specifications. The absence of a rotating field winding removes the need of brushes which means both reducing the maintenance costs and increasing the overall efficiency, since no active losses exist in the rotor and the friction losses are drastically lessened. Nevertheless, the absence of rotating windings leads to a reduction in the rotor inertia which means that faster mechanical dynamics can be easily achieved. As a drawback the high cost of permanent magnet materials should be considered during the production phase; furthermore, the magnets themselves are the main component affecting the machine rating because of the temperature limits and the risk of demagnetisation, which affect the overload capacity (as pointed out in [11]). An exhaustive introduction to PMs and their main characteristics is reported in [18] with particular concern for rotating electrical machines; with regard to the latter, the same source offers an overview of the main arrangements and magnetization patterns for PMs. Of particular interest is the Halbach magnets arrangement, which is characteristic of the machine to be tested in this work. Conventionally, a PM brushless electric motor has a slotted shaped iron core which holds the stator winding (conveniently distributed along its whole periphery) and a rotor which can assume different configurations (with PMs or without -considering Synchronous Reluctance Machines-) depending on the performances to be achieved. A thorough classification of these machines can be found in [18].
If the stator has a so called slot-less topology, i.e. the stator is a simple ring and the three-phase winding is kept in the right position by means of epoxy resins, then some performance improvements can be achieved especially at high speeds; moreover, a smooth torque profile is characteristic for this kind of motor topology.
It is not the scope of this work to describe the design procedure of electric motors; however, in this chapter, some equations which are typically used during the design phase of electric machines will be recalled in the following to highlight the main operating differences between slot-less and slotted motors; finally, the motor to be tested will be introduced.

2.1 Slotted PM Machines Operating Characteristics

During the design phase of an electric machine, characteristic equations describing its behaviour depending on design parameters are typically used in order to match the specifications with convenient design choices. It is therefore fairly easy to estimate the size and the motor ratings, starting form requirements such as torque, speed, supply voltage and rated frequency. In this section, the torque generation principle for electrical machines will be described, with particular concern to the main parameters affecting it; in this regard, the contribution of the stator teeth will be highlighted as well as the inherent effect on the machine performance.

2.1.1 Fundamentals of Electromagnetic Torque Generation

The motor structure depicted in *Figure 5.1* will now be considered in order to have a visualization of the main quantities that will be introduced in the following. The motor section shows a slotted stator and an inner rotor with surface-mounted permanent magnets; the three-phase winding is conveniently distributed in the stator slots. The ideal operating condition for synchronous machines is to have a sinusoidal distribution for both stator and rotor fields at the air-gap, this ensure a smooth interaction in terms of torque. However, none of the two flux distributions are usually satisfying the aforementioned condition; in fact, the former one would be sinusoidal, if and only if, each phase winding was sinusoidally distributed (the number of conductors which make up a phase winding varies sinusoidally) along the stator bore periphery and a perfectly sinusoidal current was to flow through the phase windings, whereas the latter one would be close to sinusoidal if the magnets where conveniently shaped and/or magnetized in order to get the sinusoidal distribution (without considering the slot effect on the flux density variation as explained in). The technical challenges related to these requirements, together with practical unfeasibility (sinusoidally distributed winding and perfectly sinusoidal current), lead to having magnetic fields at the air gap which are all but not sinusoidal. As the interaction between the fundamental component of these flux distributions is the cause of the main torque generation, the existence of higher space harmonics is typically neglected in a preliminary design phase (even though many design choices are defined along the process in order to minimise them).
The most effective way to relate the torque equation to design quantities is to consider the principle of force generation on a current-carrying wire derived from the Lorentz force law, which states that the force (F) acting on a conductor in a magnetic field (B) carrying a given current (I) is proportional to its length (l) according to:

$$F = B \cdot I \cdot l \tag{2.1}$$

this equation is valid for any stator conductor, by considering the current which is carrying and the magnetic field that is facing. A further step towards the definition of the torque equation is to consider the contribution of the magnetic flux density distribution at the air gap as well as the current distribution. In order to do this two fundamental design quantities need to be introduced which are the *magnetic loading*

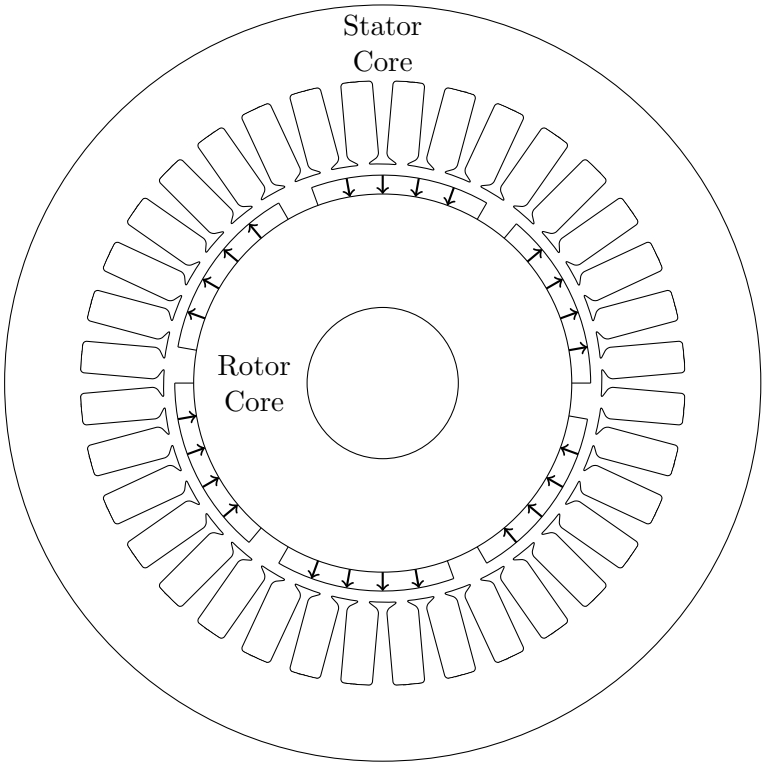

Figure 2.1: *Surface mounted PM machine structure*

($\hat{B}$) and the *electric loading* ($\hat{K_s}$); these two quantities are the main design parameters describing the ratings of an electric machine.

Magnetic Loading

The magnetic loading can also be defined as the peak value of the fundamental of the flux density distribution at the air-gap. The resulting value would depend on the type of magnets to be used as well as on their distribution in the rotor (Halbach array, surface-mounted). If the surface-mounted configuration with radially magnetised magnets (*Figure 2.1*) is to be considered, the air gap flux density distribution can be approximated as in *Figure 2.2* (blue waveform) where each magnet is supposed to span 150 electrical degrees out of 180 degrees of the pole pitch.
The fundamental peak value (or magnetic loading) comes out from the Fourier analysis of the flux distribution, resulting in:

$$\hat{B}_{g1} = \frac{4}{\pi} \cdot \hat{B}_g \cdot \sin(\alpha_{me}) \tag{2.2}$$

In order to estimate the peak value of the flux density distribution the operating magnetic circuit of a magnet can be taken into account. If the latter and its equivalent magnetic network are considered (*Figure 2.3*) than the air-gap flux density can be calculated (as explained in appendix A) as a solution of the equivalent network where: $\mathcal{R}_m$ is the magnet reluctance which considers those flux lines which do not pass the air gap but get back through the magnet itself, $\mathcal{R}_g$ is the air-gap reluctance and $\mathcal{R}_{Fe}$ is

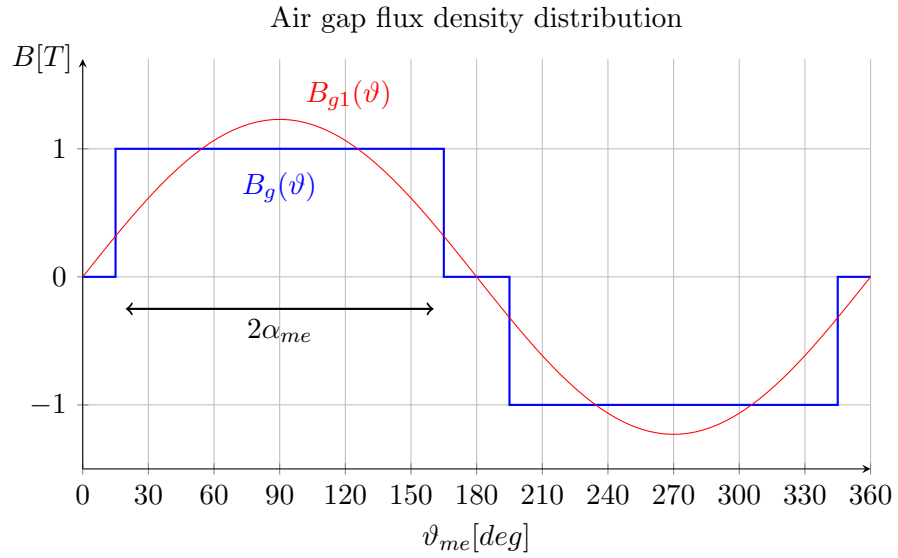

Figure 2.2: *Normalised air-gap flux density over a pole*

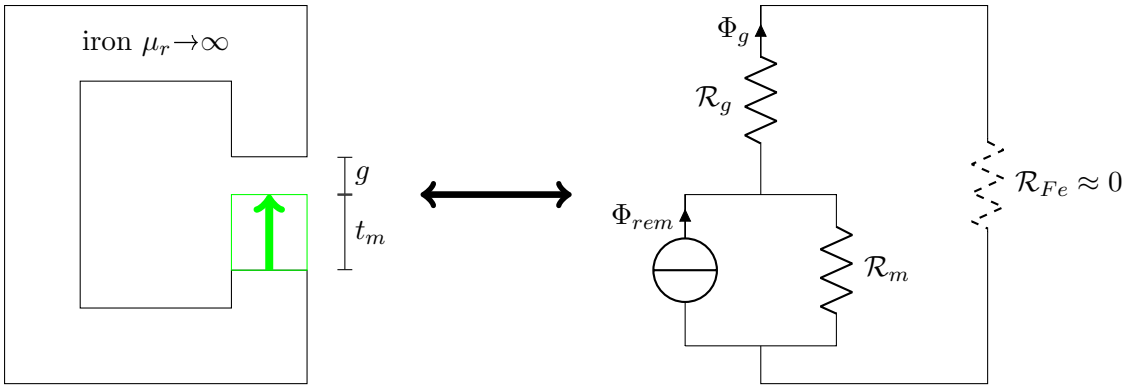

Figure 2.3: *Magnetic circuit and equivalent network of a surface-mounted PM*

the iron reluctance which can be neglected as long as the permeability is much higher than than the air one; resulting in:

$$B_g = \frac{B_{rem}}{\frac{S_g}{S_m} + \mu_{rec}\frac{g}{tm}} \tag{2.3}$$

The equation shows a dependency on the air-gap thickness which is not constant along the stator bore because of the slot-openings; this leads to a variation on the operating point of the magnet locally, and hence, on the air-gap flux density. Moreover, the iron in electrical machine is usually designed in order to make it work close to the saturation limit in order to reduce both material cost and weight, because of the lower iron volume needed; this might lead to have a non negligible iron reluctance when solving the magnetic network and therefore the air-gap flux density would be lower. Both these phenomena are usually considered during the design phase by just defining an equivalent air-gap which is wider than the physical one. With the definition of this "new" air-gap (2.3) holds, and gives a lower value which is meant to be much closer to a real case.

There are two further undesired phenomenon related to slot openings and iron saturation that will be now discussed from a fundamental point of view:

- Eddy currents in the magnets: it has be pointed out that the operating point of each magnet varies along the magnet itself depending on weather it is facing a stator slot or not. This means that while the rotor is rotating each point of each magnet (at least on the surface facing the stator) is crossed by a variable flux with a frequency which depends on the speed and the number of slots. For this reason eddy currents are induced in the magnets causing higher machine losses, increase in the magnets' temperature and hence, higher risk of demagnetisation;

- Cogging torque: a typical phenomenon characterising most of slotted PM machine is the so called cogging torque, which is the tendency of the rotor to maintain a preferential position when a torque is applied to the shaft. This is due to the fact that the magnets tend to align the rotor in such a position that, on average, the magnets meet a minimum reluctance with the stator surface.

- Torque ripple: the torque variation when the motor is energised is mainly due to the cogging phenomenon as well as other design parameters among which, the saturation in the stator teeth due to the magnetic field produced by the stator current. This aspect is described in [3]; it must be noted that some different solutions can be adopted to reduce the cogging torque in slotted motors; however, these solutions determine generally a de-rating in the machine performance as thoroughly discussed in [6].

It is worth mentioning that the iron saturation is also affected by the stator magnetic field, which can contribute to the equivalent air-gap increase, leading to a lower flux density in the air-gap itself. As it will be discussed, this phenomenon is more relevant for slotted motors than for slot-less motors. Since the torque capability is dependent on both the magnetic loading and the electric loading, considering that the former tends to decrease if the latter is increased, it can be typical for slotted motors not to have a torque which is linearly dependent on the motor phase current. However, if the machine is designed in such a way that the iron is not saturated in the whole operating range, then the torque could follow a linear dependency on the current, as a drawback the machine will be more heavier and with a higher production cost due to the more iron volume needed.
When the Halbach array disposition of the magnets is considered, the equivalent magnetic network analysis becomes more complicated and dependent on more parameters than it was for radial magnets. By comparing the results in [7] where radial magnets are considered with the ones in [8] where a Halbach array is considered for the same machine it can be noticed that the latter gives around 12% magnetic loading increase (if the only fundamental of the distributions is considered). The increase in the flux density is not the only advantage of using a Halbach array disposition; even though it has been proved that a back-iron for Halbach arrays can determine a further increment in the flux density, as discussed in [16], the back iron is typically not needed because of a self-shielding behaviour leading to a potential overall mass reduction [29].

Electric Loading

The concept behind the electric loading (or linear current density) definition is to consider an equivalent current distributed along the air gap, which considers both the fact that a three-phase winding is existing and it's distribution pattern in the stator slots. In order to define it, some useful parameters need to be introduced:

- N_s represents the total number of series conductor per phase; it can be defined for any winding configuration as:

$$N_s = \frac{Q_s \cdot n_{cs}}{3}$$

  where n_{cs} is the number of conductors in a slot which belong to a series connected coil (which means that if some parallel connections are existing between conductors lying in the same slot, then n_{cs} is given by the number of conductors in a slot divided by the number of parallel connections) and Q_s is the total number of stator slots.

- K_w is the *winding factor* which considers the winding distribution on the stator and, in particular, its effect on the fundamental of the stator field distribution

The electric loading is defined as it follows:

$$\hat{K}_s = \frac{3 \cdot K_w \cdot N_s \cdot \hat{I}_{ph}}{\pi \cdot D} \tag{2.4}$$

where $\hat{I}_{ph}$ is the peak phase current and D is the stator diameter.Regarding the phase current, it is worth to mention that for a winding designed with parallel connections, it can be higher if compared to a series connected winding, if the current density in the windings is kept at the same value; therefore, the electrical loading would not change for the two winding configurations Having now both the relations for the magnetic loading and the current loading, the acting traction force on can be computed as a position dependent expression by replacing flux density and current in (2.1) with the related distributions dependent on the angular position (ϑ_m), as it follows:

$$F(\vartheta_m) = \hat{K}_s(\vartheta_m) \cdot \hat{B}_g(\vartheta_m) \cdot L_a \tag{2.5}$$

where L_a now is more specifically the active length of the stator winding.
It is easy to prove that the maximum torque capability can be achieved when the two sinusoidal distribution are in phase; according to *Figure 2.4* the previous statement appears to be obvious, in fact, any displacement between the electric loading and magnetic loading distributions will cause a reduction in the peak value of the force and hence, its average value. This is true if the machine to be considered has no magnetic anisotropy; in such a case the so called reluctance effect can improve the torque capability if a convenient displacement between electric loading and magnetic loading distributions exists. Considering the case of isotropic machines under the optimal operating condition depicted in *Figure 2.4* the resulting surface traction (F_{surf}) acting in the air-gap can be found by first computing the average force under a pole:

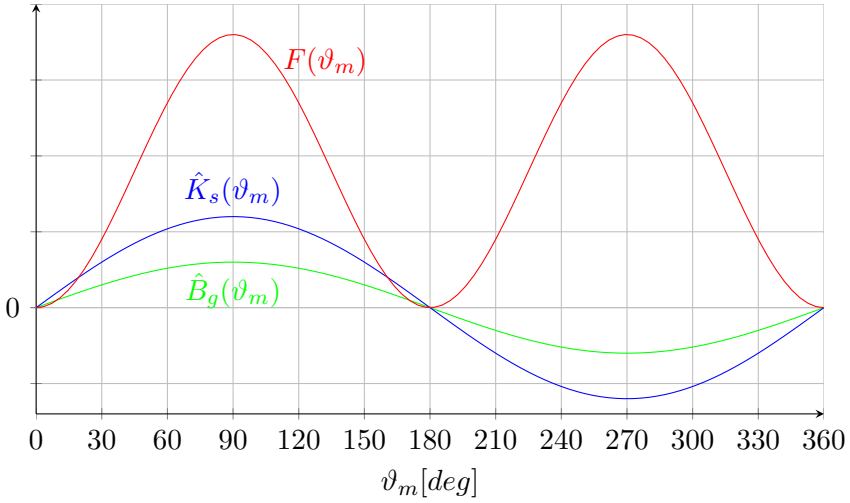

Figure 2.4: *Force distribution along the stator bore*

$$\begin{aligned} F_{avg,pole} = \frac{1}{\pi}\int_o^{\pi} F(\vartheta_m)d\vartheta_m &= \frac{1}{\pi}\int_o^{\pi} \hat{K}_s \cdot \hat{B}_g \cdot L_a \cdot \sin^2(\vartheta_m)d\vartheta_m \\ &= \frac{1}{\pi}\cdot \hat{K}_s \cdot \hat{B}_g \cdot L_a \cdot \left[\frac{\vartheta_m}{2} - \frac{\sin(2\cdot\vartheta_m}{4})\right]_0^{\pi} \\ &= \frac{1}{2}\cdot \hat{K}_s \cdot \hat{B}_g \cdot L_a \end{aligned} \tag{2.6}$$

and then multiplying it by the whole bore length as it follows:

$$F_{surf} = F_{avg,pole}\cdot\pi\cdot D = \frac{1}{2}\cdot\hat{K}_s\cdot\hat{B}_g\cdot L_a\cdot\pi\cdot D \tag{2.7}$$

The acting torque is then computed by multiplying the surface traction by the arm at the air-gap, giving the final torque equation as:

$$M = F_{surf}\cdot\frac{D}{2} = \frac{\pi}{4}\cdot\hat{K}_s\cdot\hat{B}_g\cdot L_a\cdot D^2 \tag{2.8}$$

this equation will be used in the following as an important comparison point between slot-less and slotted machines.

2.2 Slot-less PM Machines Characteristics and Operation

The typical structure of a slot-less machine (*Figure 2.5*) as compared to the slotted one (*Figure 2.1*) shows its main peculiarity in the stator topology. From a structural point of view, the teeth, in a slotted machine, compose the holding structure for the stator winding. The slot-less configuration, introduces an important challenge in the stator manufacturing process; as a convenient stiffness for the stator ring needs to be achieved,

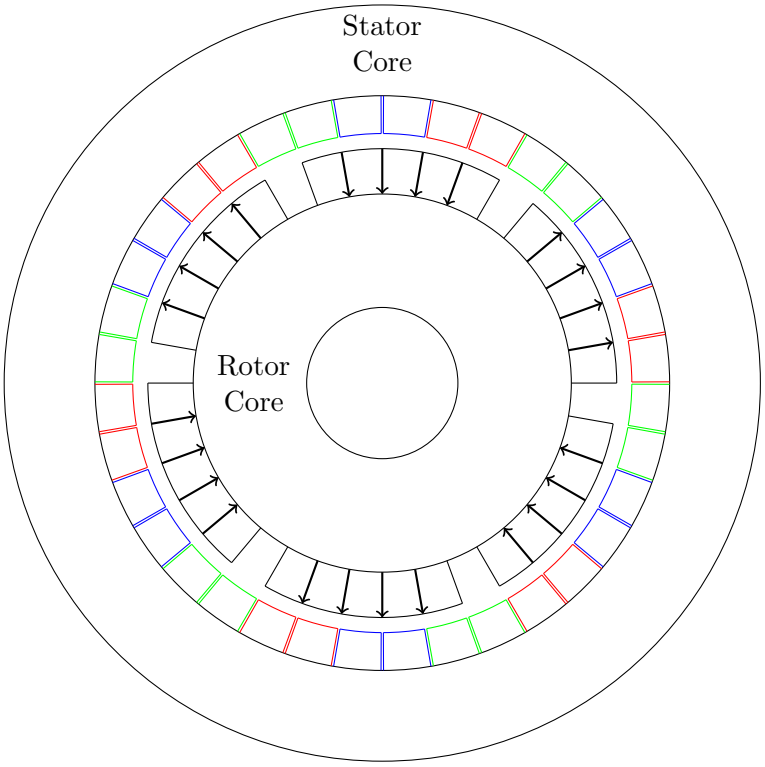

Figure 2.5: *Slot-less SPM machine structure*

the winding is encapsulated in resins by means of suitable moulding processes.
On the other hand the winding configuration for a slot-less machine is not bound by the stator core topology; this introduce an important potential for slot-less machines when the production flexibility is to be considered. Furthermore, as of today, the equipment involved in the winding process for slotted machines, requires important capital investments [17] which make the stator to be one of the most costly part in the production chain of slotted electrical machines. For this reason the output tends to be a standard product suitable for mass production, inhibiting the way of tailored solutions. In this regard, Alva Motor Solutions is taking its first steps towards the definition of a new production process for slot-less machines, by both taking advantage of the inherent potential flexibility of the stator configuration, and facing thoroughly the other production phases, to make the overall manufacturing process as flexible as possible.

2.2.1 Slot-less Machine Operation

The physics behind the operation of an electric machine is the same being it slot-less or slotted. The three phase stator winding energised by a three phase AC current produces a rotating magnetic field which, interacting with the rotor magnetic field (stationary with respect to the rotor itself), makes the rotor to spin. However, slot-less machines exhibit different performance with respect to slotted motors according to the following points:

- Each and every of the phenomena related to the teeth existence vanishes i.e. no

cogging torque and hence, very low torque ripple under load conditions; the air-gap flux density follows a smooth waveform without those notches due to the slot-openings, which means that magnets eddy currents reduce noticeably. The latter is a reason why slot-less machines are particularly suitable for high speed applications, since eddy current losses tend to increase with the speed squared.

- The wider magnetic air-gap of slot-less machine, with respect to slotted ones, lead to a lower torque capability and also to a lower phase inductance as it will be discussed in the following with the related effects.

Wide air-gap Effect on Operating Conditions

While for slotted machines the magnetic air-gap corresponds to the mechanical one, in slot-less machines the stator thickness contributes to the increase in the magnetic air-gap thickness. As mentioned before, this has a double effect on the machine performance/characteristics.
Considering (2.3) it is clear that the wider the air-gap, the lower the magnetic loading for a given magnet thickness; and since the magnet thickness has an inherent upper bound considering the relation between the magnetic loading increase and the higher magnets cost, it means that the torque capability is lower for slot-less machines. Furthermore, while in slotted machines, the iron surrounding the stator windings acts as an heat sink improving the thermal dissipation, in slot-less machines the windings are thermally insulated by the surrounding resin, which limits the amount of heat that can be dissipated; this can lead to higher copper temperature if the same copper losses is to be considered for two similar slotted and slot-less winding configurations. This aspect acts as a limiting factor for the electric loading which cannot be increased disregarding the thermal behaviour. This means that for a given size (diameter and axial length) and a given cooling system, a slot-less machine has an intrinsic lower torque capability, if compared with a slotted one, because of a lower maximum value for both the magnetic loading and the electric loading according to (2.8).
The most intuitive way to highlight the fact that slot-less machines have an inherent low phase inductance is to think about the magnetic circuit of a phase winding; as the definition of self-inductance (L_{self}) of a coil fulfil the following equation:

$$L_{self} = \frac{N^2}{\mathcal{R}_{eq}} \tag{2.9}$$

where N is the number of turns and $\mathcal{R}$is the equivalent reluctance of the magnetic circuit, which is typically approximated as the reluctance of the non ferromagnetic path (i.e. magnetic air-gap); as long as the latter is typically wider for slot-less machines and since the expression for the air-gap reluctance follows the following relation:

$$\mathcal{R}_{eq} = \frac{g}{\mu_0 \cdot S_{pole}} \tag{2.10}$$

where S_{pole} is the air-gap surface over a pole; it is clear that, the wider the air-gap, the lower the inductance value. Even though the final value of the phase inductance will also be affected by the existence of the other windings (which are magnetically coupled

with each other) as well as the end-windings, the self inductance calculation can give the order of magnitude of the final inductance value. As reported in [24] the inductance for slot-less machine can be 1/10 to 1/100 with respect to conventional machines; and this is not only due to the wider air-gap, but also to other design parameters such as the equivalent number of series conductor per phase (N_s), and the number of poles.
The effects related to the low inductance value will be thoroughly discussed in the following chapters.

Chapter 3

Permanent Magnet Synchronous and Brush-less DC Motor Drives

The scope of an electric drive system, is to control a mechanical load by means of an electric actuator controlling quantities such as speed, torque or position. *Figure 3.1* shows a general scheme of an electric drive system; the entire chain source+inverter+motor+load can be bidirectional if the mechanical load becomes a mechanical energy source and the power inverter controls the electrical machine as a generator to control the energy transfer from the mechanical side to the electrical one. Either way, the power converter is controlled by the output of the algorithm implemented in the controller, which handles both reference and measured signals, to provide a suitable energizing state in the electric machine in order to achieve the external reference.

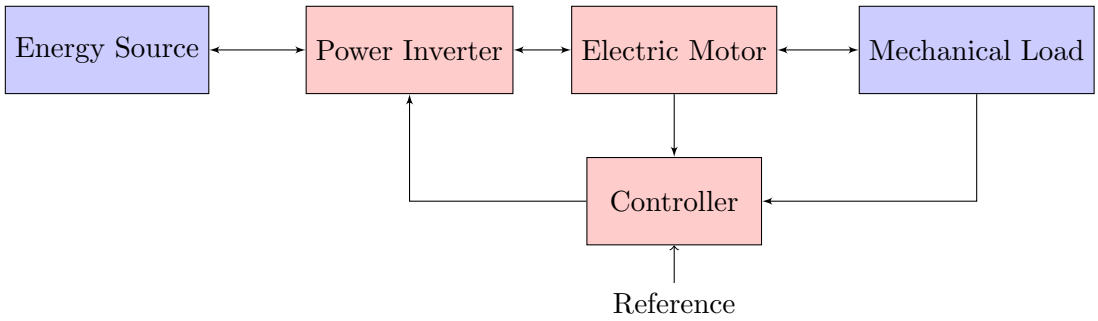

Figure 3.1: *Electric drive system scheme*

In this chapter two of the main solutions adopted in industrial applications will be analysed under different aspects, in order to map out the related peculiarities. The classification between PM Synchronous and Brush-less DC (BLDC) machines is consolidated in the literature as a reference for two differently designed machines, which are identified by different operating behaviour. The classification is mainly oriented to the different types of induced voltage waveform, or back electromotive force (back-emf), which can be measured at the motor terminals. A synchronous PM machine is designed in order to get an induced voltage waveform which is closed to a sinusoid wave whereas, a BLDC machine shows a back-emf waveform which resembles a trapezoidal wave. The way in which these two type of machines are controlled, is a consequence of the afore-

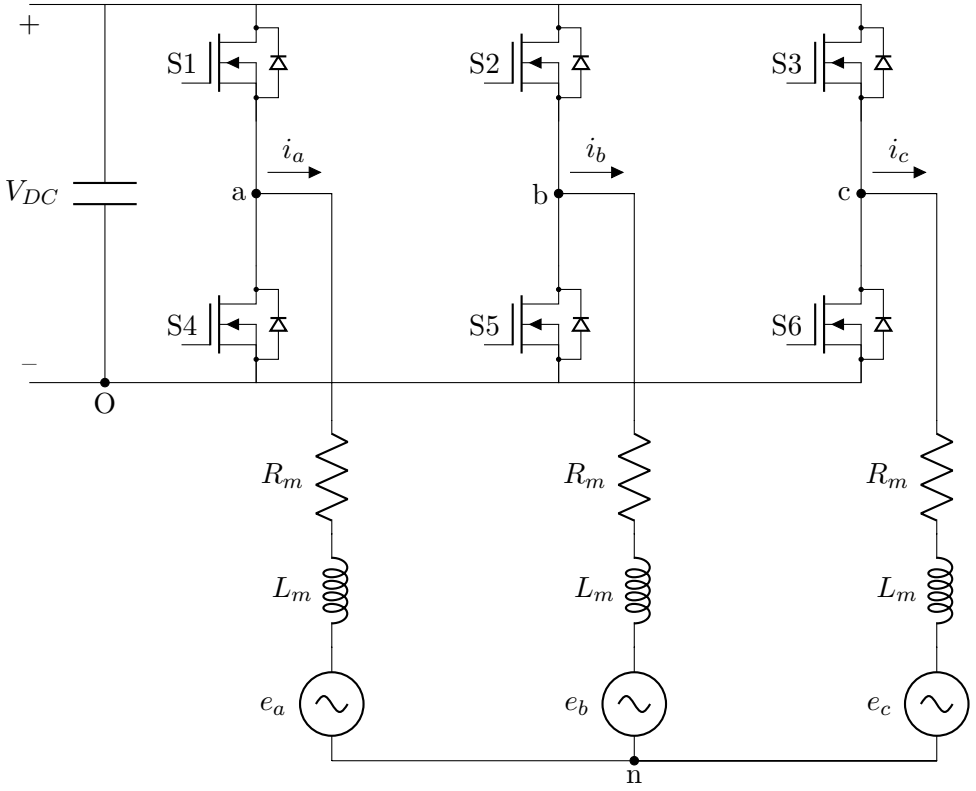

Figure 3.2: *electric circuit of a three-phase inverter fed motor*

mentioned characteristics and hence, one typically refers to either *"sinusoidal control"* or *"trapezoidal control"* respectively. The two different controls define the switching pattern at the power inverter; the latter, in turn, decides the current waveform flowing in the motor.
In *Figure 3.2* the generic representation of an inverter fed three-phase motor is shown, and it will be taken as a reference for both the PM synchronous and BLDC motor drives; as it will be discussed the difference for the two solutions is in the back-emf waveform (represented as a voltage source for each phase) and in the applied voltage which is decided by the way in which the switches are controlled.
Without loss of generality, as a first stage the switches will be considered as ideal devices with zero delay switching state. Finally, the real behaviour of a power switch will be considered with particular concern for the effects on the overall system.

3.1 PM Brush-less DC Motor Drive

Despite of the name, a PM brush-less DC (PMBLDC) motor is nothing more than an AC machine, considering that the current flowing in the armature winding is alternating. The reason why it is called DC, is due to the fact that the operation principle resembles the one of a brushed DC motor, where the mechanical commutator is replaced by a power inverter, ensuring that the current flowing in each phase winding is decided by the rotor position, so that the motor keeps rotating under the torque action decided by the supply system.
The operation principle can be explained by merging the circuit shown in *Figure 3.2*

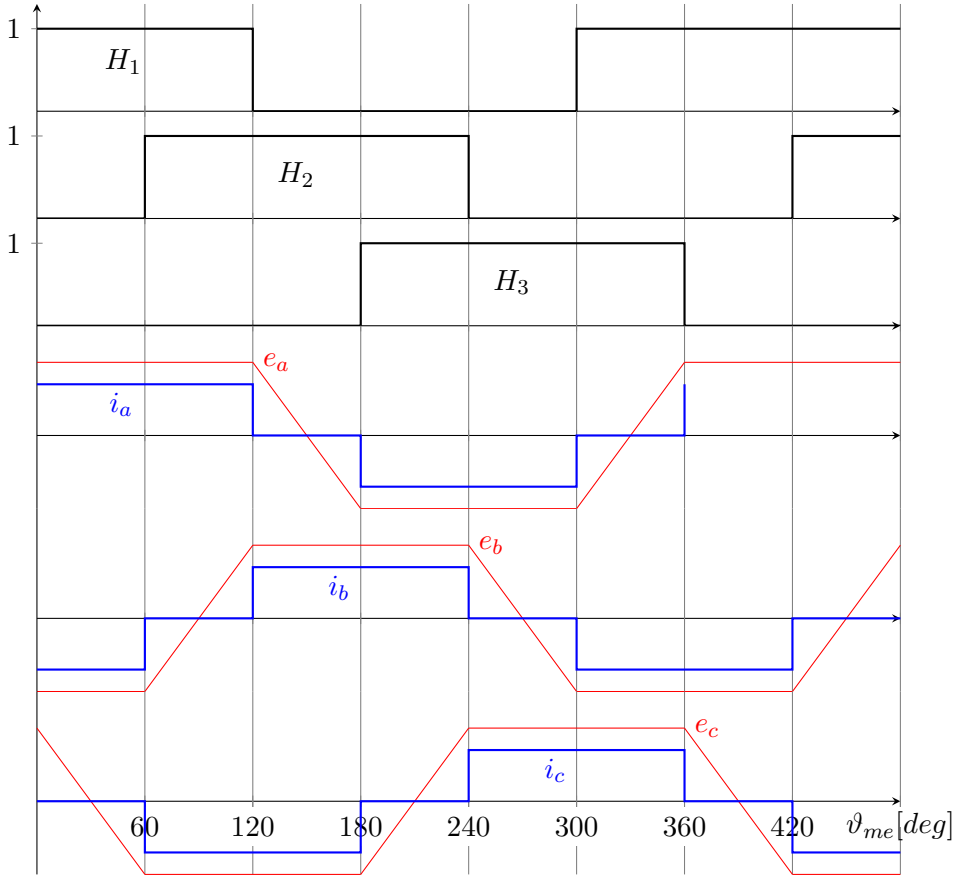

Figure 3.3: *Hall effect sensors output, Ideal back-emf and current waveforms for a PMBLDC motor*

and the waveforms depicted in *Figure 3.3*. In particular, the first set of waveforms in *Figure 3.3* (black waves) represents the output of the three Hall effect sensors mounted on the motor to sense the passage of the magnets, and hence, to detect the rotor position; any pulse represents the passage from a rotor polarity to another, in front of the sensors. This information is used to properly control the inverter. The back-emf waveform itself contains information regarding the rotor position; a proper operation of a BLDC motor requires the phase current to be in phase with respect to the back-emf. Disregarding the way in which the rotor position is detected, which can be either with a sensor-less approach (considering the back-emf waveform) or by means of sensors (such as Hall effect sensors), the current is forced to flow as shown in *Figure 3.3* (blue waveforms), by conveniently controlling the switches of the inverter.
In Table 3.1 all the possible conduction states at the power inverter are summarized. It can be noted that in the trapezoidal control of a BLDC motor the inverter is applying voltage to two of the three phases,and hence, only two phases are conducting at any instant.
A different expression for the electromagnetic torque comes out from the motor power balance (as it will be proved in the following chapter); so that, the torque equation can be written as it follows:

$$m = \frac{1}{\omega_m}(e_a \cdot i_a + e_b \cdot i_b + e_c \cdot i_c) \tag{3.1}$$

Switching state	Electric angular coordinate	Sensors output			Firing signals to		Phase current		
		H_1	H_2	H_3			i_a	i_b	i_c
0	0°-60°	1	0	0	S1	S5	+	-	off
1	60°-120°	1	1	0	S1	S6	+	off	-
2	120°-180°	0	1	0	S2	S6	off	+	-
3	180°-240°	0	1	1	S2	S4	-	+	off
4	240°-300°	0	0	1	S3	S4	-	off	+
5	300°-360°	1	0	1	S3	S5	off	-	+

Table 3.1: *Inverter switching states*

Therefore, according to the ideal current and back-emf waveforms, a BLDC motor would exhibit a merely constant torque. However, in a real case, neither the current nor the back-emf follow the ideal scenario. The back-emf can be similar to a trapezoid if a convenient magnet shape and winding distribution is adopted. On the current side, a sudden variation, following the so called quasi-squared waveform depicted in *Figure 3.3*, is physically not possible. The latter statement is proved by the existence of an inductive behaviour for each and every the motor windings (represented as an inductance for each phase representation in *Figure 3.2*); this means that the current variation follows the solution of an RL circuit, and hence, the lower the inductance, the faster the current variation. Though, the existence of a non-zero rise and fall time in the phase current, during the commutation instants, leads to torque notches; such a phenomenon is also known as commutation effect.
One could say that in order to minimize the commutation effect, the lower the inductance, the better. However the trapezoidal control is typically coupled with Pulse Width Modulation (PWM) control of the power inverter, to ensure speed control when the DC input voltage is fixed. And this control introduces current variation at the switching frequency of the power inverter.
The operating condition depicted in *Figure 3.3* would generate a certain torque (depending on the motor) which makes the motor to rotate at a given speed (if the mechanical load is considered as a constant breaking torque). Thus, the peak value of the current should be varied in order to control the motor torque, and thence to regulate the speed. A PWM technique is adopted to pursue the latter task, and a suitable control algorithm makes sure that the goal is achieved by defining the duty cycle for the PWM control. The aim is to vary the voltage applied to the two conducting phases by chopping the input DC voltage at high frequency (switching frequency) to get the required average voltage needed to achieve a given current, along with a given torque. There are two different PWM techniques:

- **Bipolar (hard) PWM switching**: considering that each switching state in Table 3.1 involves the upper switch for the phase carrying a positive current, and the lower switch for the phase conducting a negative current; the bipolar PWM applies the chopping PWM signal to both the switches, and hence, to both the inverter legs (since the switches of a leg receive signals which are complementary to each other). This method allows a four-quadrant operation, meaning that the

current can flow with opposite signs with respect to the ones displayed in Table 3.1; as a drawback the voltage varying between $\pm V_{DC}$ leads to high current ripple.

- **Unipolar (soft) PWM switching**: this technique establishes a PWM control only for the leg where the upper switch is turned on (e.g. between 0°-60° S1 and S4 are control with two complementary PWM signals whereas S5 is left on). In this way the applied voltage varies between $+V_{DC}$ and 0, this ensures lower current ripple with respect to the bipolar PWM switching, but it also means that the operation in 4 quadrants is available only with a convenient modification in the control algorithm.

Back to the inductance issue; considering that typical switching frequency for electric drives systems are limited around some tens of kHz, it might be that a low inductance value leads to wide current variations around the required value, due to the inverter switching. A phase current having high harmonic content at high frequencies generates harmonic fields rotating in the motor at high speeds, increasing the total amount of losses, and therefore, the overall efficiency drops.
The latter comment highlights what the main issue of electric drives using slot-less machines is. The inherent low inductance value of this type of machines would typically lead to high current ripple. So different solutions, such as additional external inductors and higher switching frequency inverters will be considered in the following chapters, highlighting both advantages and drawbacks for both the different solutions.
Under trapezoidal control the mechanical speed (n) of the rotor is related to the frequency (f) of the quasi-square waveform according to the usual relation:

$$n = \frac{60 \cdot f}{p}$$

this means that only the fundamental of the quasi-square waveform rotates synchronously with rotor; all the other current harmonics behave as the fundamental one, generating rotating magnetic fields which rotate faster in the air-gap. Therefore, these harmonic fields are origin of additional losses in both the rotor and the stator. As reported in [19] having non-sinusoidal current waveforms in PM synchronous machines leads to higher overall losses.
Even though the high efficiency might not be the primary characteristic for BLDC motors under trapezoidal control, the related drive system boasts other advantages such as cheap and reliable sensor solution (the Hall effect sensors are a cheap and low-weight solution) and ease of implementation in the control algorithm (the Hall effect sensors gives directly the firing signals which are easily processed by a dedicated driver circuit controlling the inverter switches).
A PMBLDC drive model will be described in this work but without any focus on the performance evaluation with respect to the motor described in Chapter 4 being it designed for a sinusoidal control.

3.2 PM Synchronous Motor Drive

Differently from a PMBLDC machine, a PM synchronous motor (PMSM) is conveniently designed in order to get a back-emf which is as sinusoidal as possible. This type

of machine exhibits an inherent high efficiency and smooth torque operation in so far as the phase current is sinusoidal. This means that the algorithm controlling the power inverter is different from the one described for the trapezoidal control. The sinusoidal control requires the duty cycle of each inverter leg to vary sinusoidally; in this way, the phase voltage is still a chopped signal (varying sinusoidally on average), and the current waveform of each phase follows a sinusoid, because of the current response of a phase winding due to its inductive behaviour.
The issue of the current ripple, due to the switching at the power inverter, remains a problem as it is for the trapezoidal control. Which means that during the design phase of an electric drive system, any component of the system needs to be conveniently designed to achieve the ideal operating conditions of the system itself, and the choice of a proper control algorithm alone results to be not enough.
There are many different implementations for the sinusoidal PWM control; at the beginning, the well-known carrier-based PWM techniques [15] were used, when analogue circuits where more widespread than the digital ones. As of today, the same algorithm can be implemented in a more common digital controller, and many other different algorithms has been developed to achieve different improvements such as lower switching losses, lower harmonic content in the output voltage and ease of implementation. It became more and more common nowadays to mention Space Vector Modulation (SVM) when talking about novel electric drives systems, and in [30] the relation between SVM techniques and carrier-based techniques is highlighted. In this work the Symmetrical PWM or SYPWM (according to [30]) is developed for the sinusoidal control because of the better utilisation of the input voltage (higher maximum phase voltage achievable with a given input DC voltage) and the ease of implementation.

3.3 Power Electronics and Inverter Modelòing Assumptions

The power inverter implementation that will be proposed, considers ideal semiconductor devices which means that the whole switching dynamic of the switches is neglected. However, considering the switching frequency increase as a potential solution for the current ripple reduction, it is worth to mention which kind of critical issues are related to this type of solution along with different solutions offered by cutting-edge technologies. Without going too much into the physics governing the operation of these type of devices, in the following, some of the most relevant parameters defining the operational behaviour of a switch will be discussed

3.3.1 Fundamental on Switching Dynamics

The power level of the motor tested in this work, matches with the capabilities of MOSFETs [22], in terms of semiconductor devices, also considering the relatively high switching frequency needed in electrical drives. However, the parameters affecting the switching dynamic will be described disregarding the type of semiconductor device to be used.

One of the first things to be considered for a proper operation of the inverter is the so called *"dead time"*. This parameter is usually set in the driver circuit, which is the

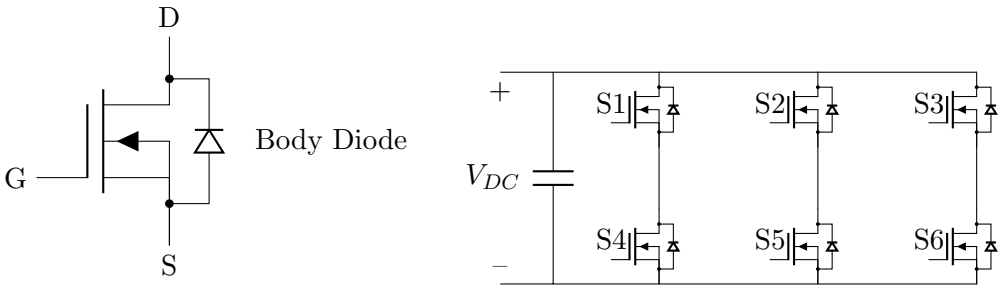

(a) MOSFET with body diode schematic circuit

(b) Inverter scheme

Figure 3.4: *Inverter and MOSFET schemes*

component commanding the commutation of the switches through convenient signals sent to the gate pin (G in *Figure 3.4a*) of the switches themselves. The dead time ensures that the two switches of a same leg are controlled with two signals which are delayed to each other; this denies the possibility of the two switches to be closed at the same instant, thus, avoiding the risk of short-circuit at the power supply (which could destroy the switches in a few commutation cycles). The dead time will be included in the inverter model considering data regarding the switches mounted in the motor controller used in the test-bench setup.

The dead time is typically related to the switching dynamic of the device as well as the minimum duty-cycle required during the PWM operation [26]. As described in [23]and in [9] the switching dynamic of a power switch follows different stages which are dependent on both the device itself (internal capacitances) and the circuit topology in which it is working (parasitic inductances); particularly, in [9] the behaviour of an isolated switch is considered so that the switching performances are assessed by just considering the quality of the device, whereas [23] offers a losses-oriented analysis of the MOSFET switching dynamic under real operating conditions. The latter one, highlights the effect of parasitic inductances given by the source connection to the power converter and the ones related to the device package and PCB conductive traces on the switching dynamic, and, more particularly, on the current variation. It is worth noticing that the switching time specified in the devices' data sheets are usually evaluated under ideal conditions, thus, it should not be used directly to evaluate the maximum switching frequency capability of a switch, and the dead time to be set in the control of the devices.
The non ideality of the switching phase, due to parasitic components, can lead to higher losses in the semiconductor devices; this means that the efficiency of the power inverter drops along with the lifetime expectancy. Moreover, the maximum permissible switching frequency will be lower because of the longer dead time interval required. Taken all together, these considerations lead to say that the increase in the switching frequency of a power inverter is not just a matter of the semiconductor type to be used, but also, and especially, of the circuit topology in which they are called to operate.

Another issue related to parasitic parameters is the one regarding Electromagnetic Interferences (EMIs); even though they have been not the main concern for this work,

it is worth to mention it, because a typical requirement for many motor controllers is the minimum load inductance connected to each inverter leg, which is required to minimize the noise emission due to current variation, along with voltage variations in parasitic elements.

3.3.2 Wide-bandgap Semiconductor Potentials

The wide-bandgap (WBG) semiconductor technology represents a promising solution in the already developed semiconductor industry. As of today, WBG semiconductors technologies cover around 0.05% of the global semiconductor market [2]; the main peculiarities of this kind of devices are the higher withstand voltage due to the wider bandgap and higher maximum operating temperature. Moreover, the enhanced thermal conductivity enables to reduce system cooling requirements. The materials used in WBG semiconductors, ensure also to increase the maximum switching frequency if the packaging design is conveniently adapted, in order to reduce intrinsic parasitic components [2]. However, as mentioned before, focusing on the semiconductor performance is typically not enough when aiming for higher switching frequency, especially when specific restrictions on EMI limitations are added to the set of initial specifications for a motor controller. The drawback of not having a consolidated manufacturing, as it is for standard semiconductor devices, can lead to performance de-rating if compare to experimentally proven ones as well longer lead times.
It is worth to mention that some motor-controller manufacturers are offering solutions with maximum switching frequencies up to more than a hundred kHz [14].

Chapter 4

Alva Prototype (*Thor*)

The aim of this chapter is to introduce the motor tested in this work and validating the choices made during the motor design phase, with particular concern for the stator specifications coming from Alva technology.
As the first iteration of a prototyping phase, *Thor* was meant to be the proof of concept for the novel technology developed by Alva Motor Solutions; which allows the production of unique slot-less stators, when compared to other manufacturers of the same type of machine. The assembly takes the rotating frame from another slot-less motor manufacturer, where the stator has been replaced with the one produced with Alva technology (*Mjöllnir*).

4.1 Double air-gap topology

Figure 4.1 shows the motor topology; in particular *Figure 4.1a* shows the entire section of the motor whereas *Figure 4.1b* shows the part considered for the Finite Element simulations.
The rotor is made up of an inner ring (inner rotating back-iron) and an outer ring where the magnets are placed according to a Halbach array arrangement. The ring in between the two rotating parts, is the schematic representation of the stator, which has been conveniently divided into blocks, each of them representing an equivalent slot.
The double-airgap configuration is the result of some different design, manufacturing, and economic assumptions. As mentioned in the related section of Chapter 2, the operating condition of a slot-less machine makes it suitable for very high speed applications; if the latter condition is considered, along with a configuration with high number of poles, then it means that the fundamental supply frequency needs to reach high values. If a single air-gap topology with stator back-iron were to be considered, then the iron core itself would need to be laminated to reduce both hysteresis and eddy-currents losses; moreover, the higher the number of poles the lower the flux over each pole, which means that a smaller thickness for the back iron is required to carry the flux (if the saturation condition is given [13]). In this regard, requiring this type of ring-shaped lamination with a low radial and axial thickness can be either a challenge from a production point of view or an economically unacceptable solution, especially if low-volume manufacturing is required.

On the other hand, not having a back-iron for the stator, at all, would drastically reduce the torque capability because of the wider magnetic air-gap which would result considering an average flux path. Considering all the previous comments, the double air-gap configuration appears to be the optimal solution. In fact, having a rotating back-iron for the stator eliminates the need of having it laminated; furthermore, the magnetic air-gap results to be well-defined and less wide than the equivalent one without any back-iron.

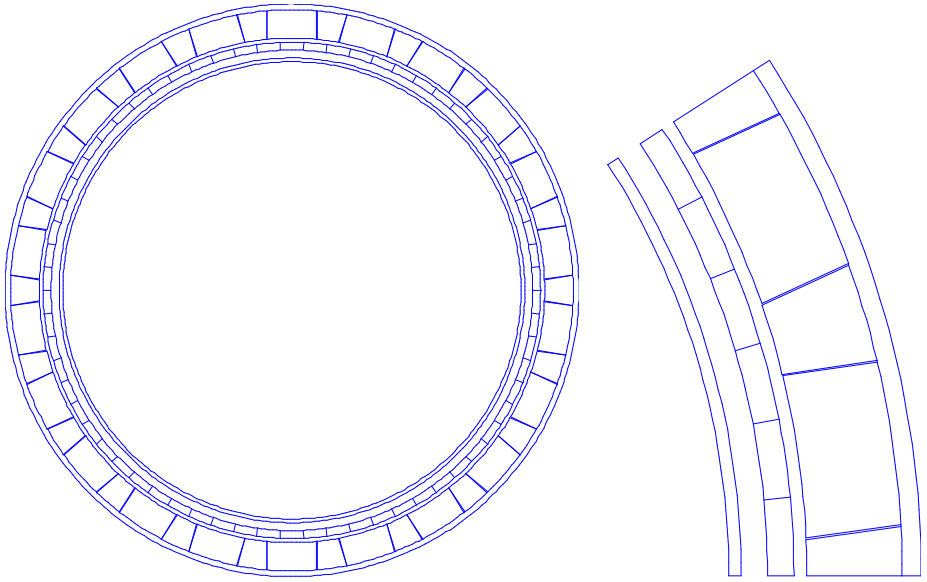

(a) Motor section, ***(b)*** Two poles section,

Figure 4.1: *Tested motor drawings*

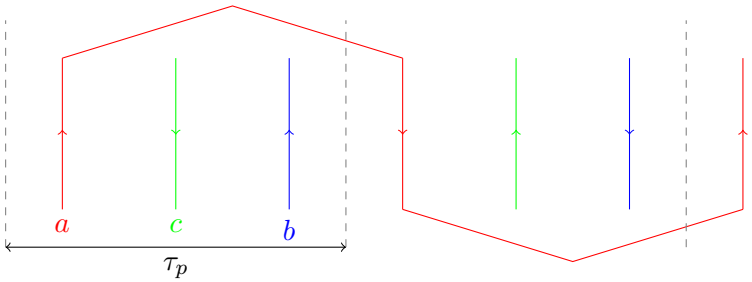

Figure 4.2: *Schematic winding configuration*

4.2 Stator configuration

The stator prototype, has been designed and produced considering Alva technology capability at this prototyping stage. The stator production process uses copper Litz wires; this choice allows Alva to take full advantage of its production technology and, in terms of final machine operation, to ensure high efficiency at very high speed, since the skin effect is drastically reduced. In *Figure 4.2* a schematic representation of the winding is shown over two poles along with the winding pattern for one of the three phases. Despite the "slot-less" configuration, it appears to be useful the definition of

Parameter	Value	Unit of measurement
Outer diameter	76.4	[mm]
Outer back-iron thickness	0.76	[mm]
Magnets thickness	3.81	[mm]
Stator outer diameter	66.21	[mm]
Stator inner diameter	64.1	[mm]
Inner back-iron thickness	0.5	[mm]
Number of poles ($2p$)	22	[-]
Number of slots (Q_s	66	[-]
Number of conductors per slot	6	[-]
Number of strands per litz conductor	30	[-]
Single strand diameter	0.1	[mm]
Number of parallel connections	1	[-]

Table 4.1: *Motor data*

"slot" in order to define related quantities; in this case a "slot" is a stator section (on the active side of the winding) gathering the conductors which belong to the same phase. As *Figure 4.2* the winding is characterized by one slot per pole and per phase ($q = 1$) and in each slot there are 6 conductors, belonging to the same phase, which are connected in series along the stator with the pattern shown. All the useful data for the motor characterization are summarized in Table 4.1.

4.3 Halbach array pattern

The rotor mounts 44 NdFeB magnets on the inner surface of the outer back-iron ring according to a Halbach array arrangement as shown in *Figure 4.1*. The gap in between the magnets (around $0.06mm$) has been set to consider a thin plastic foil and glue which are placed to make the Halbach array structure
As already discussed in the Subsection2.1.1 the adoption of Halbach array patterns brings some useful advantages and when compared to the standard radial magnets configuration. In particular, the inherently higher flux density which can be reached with a Halbach array pattern can bring some improvements in terms of torque capability. However, it is worth to mention that the production process for this kind of magnets pattern tends to be less straightforward than the standard radial magnets arrangement. The outer back-iron absolves to both a mechanical task, supporting the centrifugal force acting on the magnets array, and to the air-gap flux density improvement (as discussed in [16]). All the useful data regarding the magnets are reported in Table 4.2.

In order to define the air-gap flux density for the Halbach arrangement, a model

Parameter		Value	Unit of measurement
Inner array diameter ($D_{m,i}$)		67.26	[mm]
Outer array diameter ($D_{m,o}$)		74.88	[mm]
Tnagentially magnetised magnets	Inner angle	0.3	[fraction of the pole angle]
	Outer angle	0.37	[fraction of the pole angle]
Radially magnetised magnets	Inner angle	0.686	[fraction of the pole angle]
	Outer angle	0.616	[fraction of the pole angle]
Residual induction (B_{rem})		1.35	[T]

Table 4.2: *Magnets data*

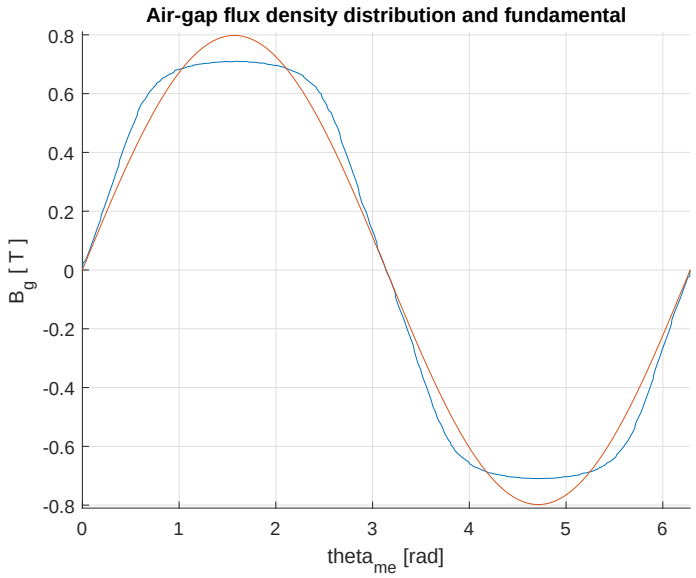

Figure 4.3: *Flux density distribution along the stator from FE analysis*

based on a magnetic network analysis has been developed (appendix B). To prove the effectiveness of the model, the same code which solves the circuit, builds the FE model of the motor to evaluate the flux density along the stator. The result from the FE analysis under no load condition is shown in *Figure 4.3*; the peak of the flux density is $0.71[T]$ and the circuit solution gives $0.72[T]$. However the magnetic network gives no information regarding the flux density distribution, and hence, no way to accurately estimate the fundamental. An approximate solution would be to say that the peak obtained from the circuit solution is relative to a quasi square flux density distribution which is non-zero over the radial magnets and zero elsewhere. Under this hypothesis one could use (2.2) to estimate the peak of the fundamental. In this way the fundamental from the magnetic network is $0.773[T]$ whereas from the FE solution $0.8[T]$. It is worth to point out that the flux density distribution varies a lot with the radial coordinate (as shown in [8]); therefore, in order to estimate the fundamental a further step should be taken to define the flux density distribution depending on the stator position in the air-gap and the magnets geometry.

4.4 System data

The all useful parameters are reported in Table 4.3. These data are measured directly from the prototype and are needed to define the electric drives models. It is worth to mention that the same models could be defined based on analytical estimation of all the useful parameters; however particular care should be given to the inductance estimation especially for the end winding contribution. In fact, even though for slotted machines the end winding inductance can be neglected in most of the cases ()considering the main inductance contribution from the active side of the winding), for slot-less machines the latter statement is no longer valid because of the inherent low inductance value of the active part of the winding [27]. Therefore, a convenient model for estimating the end-winding inductance should be developed depending on the winding configuration.

Parameter	Value	Unit of measurement
Phase resistance (R)	0.209	[Ω]
Phase inductance (L)	5.75	[μH]
Magnets flux (Λ_{mg})	0.00217	[Vs]
Pole pairs (p)	11	[-]
Back-emf constant (K_e)	0.02387	[Vs]
Rotor inertia (J)	1.08e-4	[kgm^3]
Bearing friction coefficient (B)	4e-6	[Nms]
Current limit (I_{lim})	6.2	[A_{rms}]
DC voltage limit (V_{DC})	60	[V]
Maximum speed (n)	10000	[rpm]
Additional inductance (L_{add})	210	[μH]
Switching frequency (L_{add})	25	[kHz]

Table 4.3: *Machine data*

Chapter 5

Permanent Magnet Brush-less DC Machine Drive Modelling

When talking about Brush-less DC (BLDC) motor, one generally refers to a synchronous motor conveniently designed in order to get a back-emf waveform which resembles a trapezoidal wave as much as possible (as mentioned in Section 3.1). In order to take advantage of such a peculiarity a suitable control technique should be adopted in order to get a smooth interaction between stator and rotor magnetic fields i.e. low ripple torque; this aim is fulfilled by controlling the power inverter so that a quasi-squared current is forced into the three-phase winding (as discussed in Section 3.1).
It is worth to notice that the model implementation of an electric drive system cannot be carried out disregarding the type of motor to be controlled nor the type of control technique to be used; indeed, when defining the transfer function based mathematical model of a BLDC motor, the operating principle of such a motor should be reminded, i.e. the fact that two phases are excited simultaneously to get the required torque. The definition of a transfer function based model becomes useful when a dedicated design of speed loop and current/torque loop controllers is required, giving a fast idea of the overall system dynamic under operating limitations (current, voltage). However, this model is not enough, when the objective of a simulation is to obtain the electric drive behaviour depending on the switching pattern at the power inverter; for this purpose the commutation logic should be included, and the time variation of the physical quantities should be considered.
In this chapter, the implementation of both these models is described, and an analytical procedure for tuning the PI controllers for the current and speed loop, is also considered.
It is also worth pointing out that the analysis of this kind of models can represent an important step during the design phase of an electric motor, especially when the motor under consideration is a slot-less or iron-less motor because of the characteristic low inductance, which can lead to specific supply requirement (voltage, switching frequency) to limit the current ripple during the operation. In fact, when the performance and the efficiency of the whole electric drive system are to be considered, having an estimation of the mechanical and electrical behaviour depending on the switching technique, already during the design phase of the motor, can lead to take different design choices to match the required specifications.

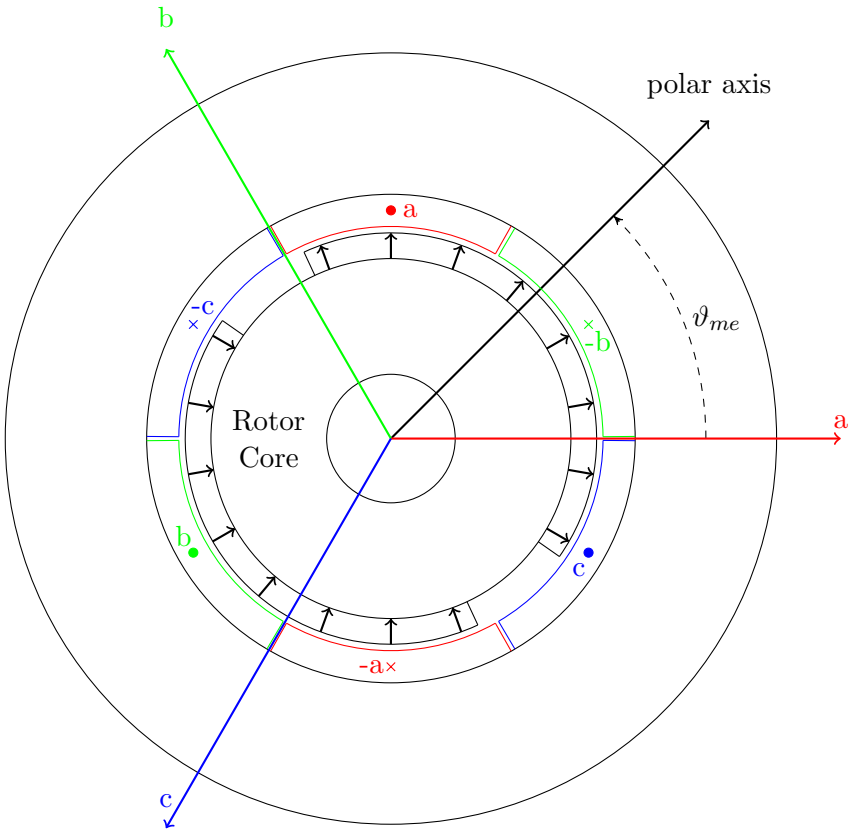

Figure 5.1: *reference PM brush-less, slot-less machine*

5.1 Permanent Magnet BLDC motor modelling

Without loss of generality, the mathematical modelling will now be described by considering the motor rule, which means that the positive sign for the current is referred to the flow from the inverter to the motor windings (as shown in *Figure 3.2*), and the general structure of the machine shown in *Figure 5.1* will be used. Specifically, the machine shown in *Figure 5.1* is referred to a two pole slot-less machine and hence, the mechanical angular coordinate ϑ_m results to be equal to the electrical one (since $p = 1$), whereas in a generic case, let p be the number of pole pairs, then the electrical angular coordinate is given by:

$$\vartheta_{me} = p \cdot \vartheta_m \tag{5.1}$$

The aim is to define an analytical description of the motor on both the electrical and the mechanical side. As a first step, the voltage equation for each phase can be written as:

$$v_x = R \cdot i_x + \frac{d\lambda_x}{dt} \qquad with: \; x = a, b, c \tag{5.2}$$

in order to define explicitly the flux linkage with each phase, some fundamental hypotheses needs to be established:

- Absence of iron magnetic hysteresis (in order for the fluxes to depend only on the currents and not on previous magnetization states);
- Absence of eddy currents in the whole machine;
- Absence of iron magnetic saturation (in order for the mathematical system to be linear);

It can be pointed out that in a real case one tries to achieve the first two hypothesis by using respectively soft ferromagnetic materials and laminated iron cores (for those iron parts facing a varying magnetic field), whereas the iron saturation appears to be an unavoidable property. However, when dealing with slot-less machines the third hypothesis tends to be generally satisfied because of the inherent low saturation which characterizes their operation [5].
Under these assumption, the flux linkage with each phase can be seen as the superposition of both the magnets' flux and the flux generated by the phase currents, as noted in the following:

$$\lambda_x = \lambda_{x,mg} + \lambda_{x,i_{abc}} \tag{5.3}$$

where $\lambda_{x,mg}$ is the flux linkage with the x-phase due to the magnets' flux, and $\lambda_{x,i_{abc}}$ is the flux linkage with the x-phase due to the three-phase current flux. Assuming now a convenient distribution of the phase windings, and an opportune shape of the magnets (or a convenient distribution, if an Halbach array is considered) such that the induced voltage on each phase winding resembles a trapezoidal waveform *Figure 5.2* ("see related chapter"); by applying the superposition principle the phase currents can be zeroed out in order to explicitly write the flux linkage variation effect on each phase due to the magnets' flux only as:

$$e_x = \frac{d\lambda_{x,mg}}{dt} \tag{5.4}$$

which is the definition of back-electromotive force for any type of flux distribution. Particularly if a BLDC machine is to be considered then the ideal back-emf can be expressed as a function of the angular position of the rotor (according to *Figure 5.1*) and the so called *back-emf constant* (K_e) which states the induced voltage on a phase depending on the rotational speed, according to the following equation:

$$\begin{cases} e_a = K_e \cdot \omega_m \cdot f(\vartheta_{me} + 5\pi/6) \\ e_b = K_e \cdot \omega_m \cdot f(\vartheta_{me} + 5\pi/6 - 2\pi/3) \\ e_c = K_e \cdot \omega_m \cdot f(\vartheta_{me} + 5\pi/6 + 2\pi/3) \end{cases} \tag{5.5}$$

where the function $f(\bullet)$ gives the trapezoidal waveform [1] which can be expressed

[1] the additional term $\frac{5\pi}{6}$ in each argument is related to the fact that in *Figure 5.1* the reference for $\vartheta_{me} = 0$ corresponds to the maximum positive linkage flux with the phase a; and hence, the back-emf is crossing the zero with negative derivative in that exact point (being it the derivative of the linkage flux)

analytically over a period as the following piecewise-defined function (in accordance with *Figure 5.2*):

$$f(\vartheta_{me}) = \begin{cases} 1 & \text{if } 0 \leqslant \vartheta_{me} \leqslant 2\pi/3 \\ 1 - 6/\pi(\vartheta_{me} - 2\pi/3) & \text{if } 2\pi/3 \leqslant \vartheta_{me} \leqslant \pi \\ -1 & \text{if } \pi \leqslant \vartheta_{me} \leqslant 5\pi/3 \\ -1 + 6/\pi(\vartheta_{me} - 2\pi/3) & \text{if } 5\pi/3 \leqslant \vartheta_{me} \leqslant 2\pi \end{cases} \tag{5.6}$$

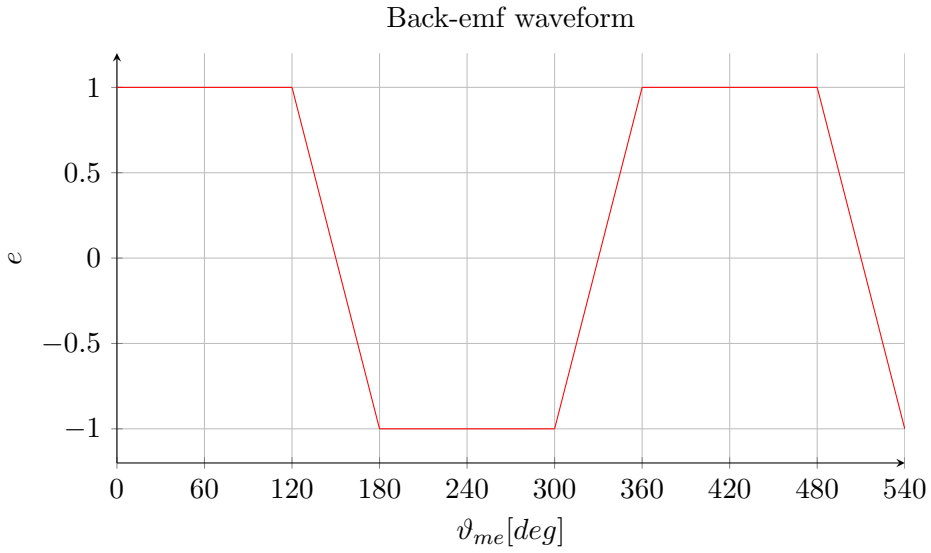

Figure 5.2: *Normalised induced emf on a phase*

In the same manner, the flux linkage with each phase due to the three-phase currents can be obtained by reducing to zero the magnets' flux (which is equivalent to demagnetize the magnets):

$$\begin{cases} \lambda_{a,i_{abc}} = L_a \cdot i_a + M_{ab} \cdot i_b + M_{ac} \cdot i_c \\ \lambda_{b,i_{abc}} = M_{ba} \cdot i_a + L_b \cdot i_b + M_{bc} \cdot i_c \\ \lambda_{c,i_{abc}} = M_{ca} \cdot i_a + M_{cb} \cdot i_b + L_c \cdot i_c \end{cases} \tag{5.7}$$

from *Figure 5.1* it can be noticed that the magnetic axis of a phase has a component which is demagnetizing with respect to the magnetic axis of the other two phases; furthermore, for construction, the mutual coupling is the same between all the three phases, leading to the definition of a unique mutual inductance coefficient (M_{ss}), defined as:

$$M_{ab} = M_{ba} = M_{ac} = M_{ca} = M_{bc} = M_{cb} = M_{ss} = - \mid M_{ss} \mid \tag{5.8}$$

similarly, a unique self inductance coefficient (L_{ss}) can be defined as:

$$L_a = L_b = L_c = L_{ss} \tag{5.9}$$

It is worth pointing out that these inductance coefficients are constant being the saturation effect neglected for hypothesis.
By enforcing that the three-phase system is balanced, i.e. no homopolar current component exists in any of the three phases, which is equivalent to say:

$$i_a + i_b + i_c = 0 \tag{5.10}$$

considering 5.9 and 5.8, the current dependent flux linkage equation 5.7 can be rewritten as:

$$\lambda_{x,i} = L_{ss} \cdot i_x + (- \mid M_{ss} \mid) \cdot (-i_x) = i_x \cdot (L_{ss} + \mid M_{ss} \mid) = L_s \cdot i_x \tag{5.11}$$

where L_s is the so called *synchronous inductance*. Even though from 5.11, the flux linkage with a phase seems to be only dependent on the current of that very phase, it is worth noting that the synchronous inductance takes implicitly into account the contribution of the other two phases' flux. The definition of the synchronous inductance allows to write 5.11 in a different and more intuitive fashion as it follows:

$$\lambda_{x,i_{abc}} = L_s \cdot i_x \tag{5.12}$$

as a result, considering 5.3, 6.1 and 5.12 the voltage equation 5.2 e.g. for the phase *"a"* can be rewritten in its final form as:

$$\begin{aligned} v_a &= R \cdot i_a + \frac{d}{dt}(\lambda_{a,i_{abc}} + \lambda_{a,mg}) \\ &= R \cdot i_a + L \cdot \frac{di_a}{dt} + \frac{d\lambda_{a,mg}}{dt} \\ &= R \cdot i_a + L \cdot \frac{di_a}{dt} + K_e \cdot \omega_m \cdot f(\vartheta_{me} + 5\pi/6) \\ &= R \cdot i_a + L \cdot \frac{di_a}{dt} + e_a \end{aligned} \tag{5.13}$$

therefore, the generalized stator voltage equation (5.2) can be written in its final form as:

$$v_x = R \cdot i_x + L \cdot \frac{di_x}{dt} + e_x \tag{5.14}$$

and the electrical angular frequency ω_{me} can be related to the electrical angular coordinate ϑ_{me} according to:

$$\omega_{me} = p \cdot \omega_m = p \cdot \frac{d\vartheta}{dt} = \frac{d\vartheta_{me}}{dt} \tag{5.15}$$

Considering the phase voltage equation as written in 5.14, the instantaneous electric power consumption of the motor can then be evaluated as it follows:

$$\begin{aligned} p &= v_a \cdot i_a + v_b \cdot i_b + v_c \cdot i_c \\ &= R \cdot (i_a^2 + i_b^2 + i_c^2) \\ &\quad + \frac{d}{dt}\left(\frac{1}{2} \cdot L \cdot i_a^2 + \frac{1}{2} \cdot L \cdot i_b^2 + \frac{1}{2} \cdot L \cdot i_c^2\right) \\ &\quad + (e_a \cdot i_a + e_b \cdot i_b + e_c \cdot i_c) \end{aligned} \tag{5.16}$$

The power expression has been conveniently split into three contributions. The first one considers the conduction loss; the second one has been opportunely rearranged in order to highlight the magnetic energy contribution and hence, it considers the magnetic energy variation [2]; as a consequence, the last term must be the expression of the mechanical power, or output power, being all the other loss contributions (eddy current loss, iron loss, proximity loss) neglected for hypothesis.
Considering the following expression for the mechanical power:

$$p_m = e_a \cdot i_a + e_b \cdot i_b + e_c \cdot i_c = m \cdot \omega_m \tag{5.17}$$

and therefore the torque equation can now be written as:

$$m = \frac{1}{\omega_m}(e_a \cdot i_a + e_b \cdot i_b + e_c \cdot i_c) \tag{5.18}$$

It is observed that the dependency on the mechanical speed would not allow to simulate the dynamic behaviour of the system starting from a static initial condition $\omega_m = 0$. In this regard the torque equation can be rewritten by replacing the back-emfs with the related explicit expressions (5.4), obtaining:

$$m = K_e \cdot (f(\vartheta_{me}) \cdot i_a + f(\vartheta_{me} - 2\pi/3) \cdot i_b + f(\vartheta_{me} + 2\pi/3) \cdot i_c) \tag{5.19}$$

Dynamically, the rotational speed of the motor follows the torque balance of a simplified system with mechanical inertia J, friction coefficient B and load torque m_l according to:

$$m - m_l = B \cdot \omega_m + J \cdot \frac{d\omega_m}{dt} \tag{5.20}$$

All the equations which have been written so far, are valid for any kind of electric motor apart from the back-emf expressions.
The implementation of the motor model could follow two different approaches; one could either rewrite all the differential equations with equivalent transfer functions or they can be conveniently gathered up in a state-space representation of the system.

[2] the $\frac{1}{2}$ factor comes out to bring the current (time dependent function) into the derivative operator

The latter one appears to be particularly suitable for a Simulink® implementation due to the compactness given by the related state-space block already implemented.
In order to minimize the size of the state-space model and hence, the number of equations to be solved, the phase voltage equations (5.14) can be conveniently combined as it follows:

$$v_{ab} = v_a - v_b = R \cdot (i_a - i_b) + L\frac{d}{dt}(i_a - i_b) + e_{ab}$$
$$v_{bc} = v_b - v_c = R \cdot (i_b - i_c) + L\frac{d}{dt}(i_b - i_c) + e_{bc}$$
$$\Downarrow$$
$$2 \cdot v_{ab} + v_{bc} = 2 \cdot (v_{ab} - e_{ab}) + (v_{bc} - e_{bc}) = 3 \cdot R \cdot i_a + 3 \cdot L \cdot \frac{di_a}{dt}$$
$$v_{bc} - v_{ab} = v_{bc} - v_{ab} + e_{ab} - e_{bc} = 3 \cdot R \cdot i_b + 3 \cdot L \cdot \frac{di_b}{dt}$$
$$\Downarrow$$
$$\frac{di_a}{dt} = -\frac{R}{L} \cdot i_a + \frac{2}{3 \cdot L}(v_{ab} - e_{ab}) + \frac{1}{3 \cdot L}(v_{bc} - e_{bc}) \tag{5.21}$$
$$\frac{di_b}{dt} = -\frac{R}{L} \cdot i_b - \frac{1}{3 \cdot L}(v_{ab} - e_{ab}) + \frac{1}{3 \cdot L}(v_{bc} - e_{bc}) \tag{5.22}$$

it is worth noting that 5.10 has been used to express i_c as a function of the other phase currents.
Finally, equations 5.15, 5.20, 5.21 and 5.22 can be gathered up under the following state-space structure:

$$\dot{\mathbf{x}} = [\mathbf{A}]\mathbf{x} + [\mathbf{B}]\mathbf{u}$$
$$\mathbf{y} = [\mathbf{C}]\mathbf{x}$$

Where $\mathbf{u}$ is the input of the system, $\mathbf{y}$ is the output and $\mathbf{x}$ is the state set of variables. Therefore, for a general three-phase motor the state-space model can be explicitly written as:

$$\begin{bmatrix} \frac{di_a}{dt} \\ \frac{di_b}{dt} \\ \frac{d\omega_m}{dt} \\ \frac{d\vartheta_m}{dt} \end{bmatrix} = \begin{bmatrix} -\frac{R}{L} & 0 & 0 & 0 \\ 0 & -\frac{R}{L} & 0 & 0 \\ 0 & 0 & -\frac{B}{J} & 0 \\ 0 & 0 & 1 & 0 \end{bmatrix} \begin{bmatrix} i_a \\ i_b \\ \omega_m \\ \vartheta_m \end{bmatrix} + \begin{bmatrix} -\frac{2}{3 \cdot L} & \frac{1}{3 \cdot L} & 0 \\ -\frac{1}{3 \cdot L} & \frac{1}{3 \cdot L} & 0 \\ 0 & 0 & \frac{1}{J} \\ 0 & 0 & 0 \end{bmatrix} \begin{bmatrix} v_{ab} - e_{eb} \\ v_{bc} - e_{bc} \\ m - m_l \end{bmatrix}$$
$$\begin{bmatrix} i_a \\ i_b \\ i_c \\ \omega_m \\ \vartheta_m \end{bmatrix} = \begin{bmatrix} 1 & 0 & 0 & 0 \\ 0 & 1 & 0 & 0 \\ -1 & -1 & 0 & 0 \\ 0 & 0 & 0 & 1 \end{bmatrix} \begin{bmatrix} i_a \\ i_b \\ \omega_m \\ \vartheta_m \end{bmatrix} \tag{5.23}$$

At this point, the solution of the state-space model will be dependent on both the type of control demanded from the inverter to run the motor and the type of motor (if different back-emf waveforms are to be considered). This means that the system behaviour can be studied, for different control algorithms, on both the electrical side (electric dynamic, current ripple) and the mechanical side (torque ripple, speed variation).

5.2 Design of Current and Speed Controllers

The dynamic of an electric drive system on both the electrical side (current variation) and the mechanical side (speed variation) is a matter of the system itself (i.e. all the parameters needed to define the model described in section 5.1) and of the controller, which handles a given input (typically the error from a feedback and the reference value) to gives an optimized output to achieve the reference value. A Proportional-Integral (PI) controller is a typical implementation for both speed and current controllers because it appears to be enough (in terms of implementation) in order to achieve typical dynamic and stability requirements. In this section the procedure for designing the PI controllers will be discussed and the resulting dynamic behaviour will be shown along with the wind-up issue and the related solution. It is worth to mention that the PM-BLDC drive model has been defined considering the measured data from the prototype; in particular, the back-emf constant is related to a sinusoidal waveform. However, the same parameter will be used to identify the trapezoidal back-emf waveform typical for a PMBLDC control.

5.2.1 System Identification in the Laplace Domain

The goal is to represent the physical system of the drive as a simple input-output (I/O) model. For this purpose, the inverter switching pattern is neglected and a simplified representation of the inverter itself is considered instead. The peculiarity of having two conducting phases at any instant is also considered. Once the aforementioned system is defined, the PI controllers fro both the current loop and the speed loop can be conveniently designed by means of the Bode plot analysis.

Current loop and PI current controller

As a first step, (5.14) needs to be represented in the Laplace domain. As described in Section 3.1 the inverter applies the voltage at two phases at a time and as shown in *Figure 3.3* the back-emf waveforms of the conducting phases exhibit opposite signs. Therefore, the voltage equation in the Laplace domain can be rewritten as:

$$v_{inv} = (R_s + sL_s) \cdot i + 2 \cdot K_e \cdot \omega_m \tag{5.24}$$

where v_{inv} is the output voltage from the inverter. The dependency on the rotational speed for the back-emf enforces the introduction of the mechanical behaviour in the

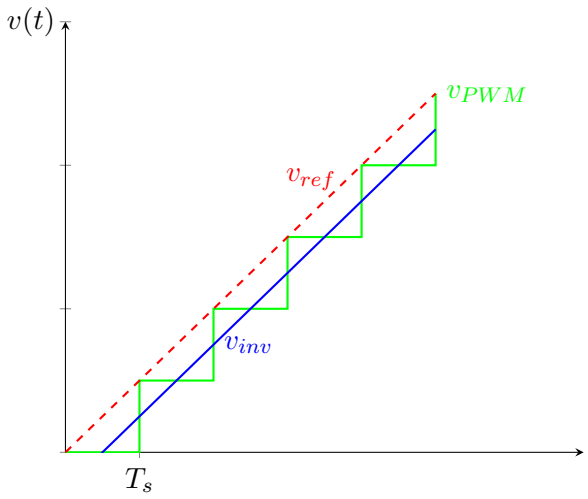

Figure 5.3: *Simplified representation for the inverter behaviour*

system; and in particular (5.20) and (5.19); the latter one, in particular, becomes (for any instant):

$$m = 2 \cdot K_e \cdot i \tag{5.25}$$

The easiest representation of the inverter is based on its inherent behaviour for which, once the reference voltage is decided (by th current controller), and translated into a suitable PWM signal, that very voltage is obtained as the average over a switching period; considering that the voltage can vary in any switching period (according to the reference input), then, globally, the voltage waveform will follow a signal which is delayed, with respect to the reference one, by half of the switching period (as depicted in *Figure 5.3*). Therefore, a good block representation of the inverter in the Laplace domain could be the one shown in *Figure 5.4* where $v_{inv,id}$ would be the v_{inv} represented in *Figure 5.3* but in this case Δv_{inv} accounts for any voltage drop which can occur at the power inverter, and the term $exp\left(-s\frac{T_s}{2}\right)$ represents the time delay of half a switching period in the Laplace domain. The inverter model can be further simplified if the internal voltage drop is neglected and considering the switching period (T_s) small enough the time delay can be written as its truncated Taylor series expansion as it follows:

$$exp\left(-s\frac{T_s}{2}\right) = \frac{1}{exp\left(s\frac{T_s}{2}\right)} \cong \frac{1}{s\frac{Ts}{2}+1} = \frac{1}{s\tau_c+1} \tag{5.26}$$

So, finally, the block diagram of the system in the Laplace domain can be represented as in *Figure 5.5*.

As a first step, in the design phase of the current controller, the I/O system ($Y(s)$) expression which relates the inverter voltage with the motor current needs to be found;

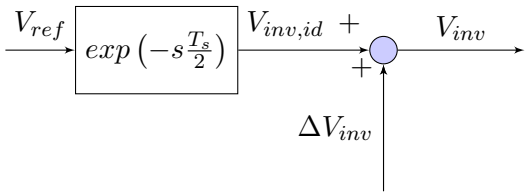

Figure 5.4: *Complete inverter block diagram in the Laplace domain*

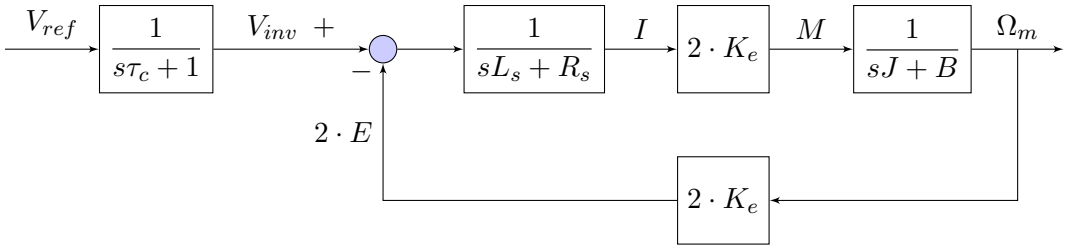

Figure 5.5: *PMBLDC drive model in the Laplace domain*

the procedure is straightforward if *Figure 5.5* is considered; though, the step-by-step procedure is described in the following:

$$\begin{aligned} I = (U_{inv} - 2K_e\Omega_m)\cdot\frac{1}{sL_s+R_s} \quad ; \quad 2K_e\Omega_m = \left(2K_e\cdot\frac{1}{sJ+B}\cdot 2K_e\right) I \quad \Rightarrow \\ \Rightarrow \quad I\left(1+2K_e\cdot\frac{1}{sJ+B}\cdot\frac{2K_e}{sL_s+R_s}\right) = \frac{V_{inv}}{sL_s+R_s} \quad \Rightarrow \\ \Rightarrow \quad Y(s) = \frac{I}{V_{inv}} = \frac{sJ+B}{(sL_s+R_s)(sJ+B)+4K_e^2} \end{aligned} \tag{5.27}$$

The definition of $Y(s)$ simplifies the system so that the current controller $C_i(s)$ can be introduced in the block diagram as shown in *Figure 5.6*.

The system to be controlled ($GH_R(s)$) is then given by:

$$\begin{aligned} GH_R(s) = G_inv(s)Y(s) &= \frac{1}{(s\tau_c+1)}\frac{sJ+B}{(sL_s+R_s)(sJ+B)+4K_e^2} \\ &= \frac{sJ+B}{(s\tau_c+1)[s^2JL_s+s(JR_s+BL_s)+R_sB+4K_e^2]} \end{aligned} \tag{5.28}$$

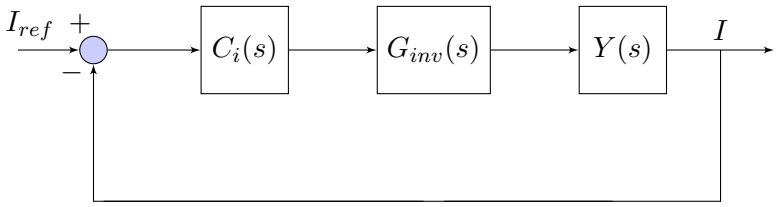

Figure 5.6: *Feedback current loop*

The analysis of this transfer function by means of the Bode plot theory, requires it to be written in a proper form so that the roots of the polynomial at the numerator (*zeroes*), and at the denominator (*poles*) are highlighted in order to clearly define the position of poles and zeroes in the frequency domain (*break points*). This type of approach can be helpful when studying the dynamic of the system depending on the drive parameters, and hence, it could be used for designing the system in order to achieve specific performance. However this was partially the goal of this work which rather aims to define a convenient relation between the inverter time constant (τ_c) and the electric time constant of the motor ($\tau_e = L/R$) to fulfil both a good controllability (fast and stable dynamic) and good overall performance (low current ripple); in this regard, technological constraints and limitations must also be considered.
For this particular case, the switching frequency was set as a constraint to $25kHz$ as related to the motor controller available in-house. Thus, the only variable to be modified is the electric time constant of the motor, and since increasing the resistance would lead to an increase in the conduction losses, the only parameter which was set as a variable is the inductance value. Forasmuch as the prototype was designed to operate under sinusoidal control, the procedure for choosing a suitable additional inductor will be described in the related chapter; however the model simulations and the experimental validation were conducted considering an additional inductor available in-house.

PI current loop controller design For designing the PI current loop controller ($C_i(s)$) the following procedure has been used. As a first step the transfer function of the PI controller is defined as:

$$C_i(s) = K_{I,i}\frac{1 + s\tau_{r,i}}{s} \quad with \quad \tau_{r,i} = \frac{K_{P,i}}{K_{I,i}} \tag{5.29}$$

where $K_{P,i}$ and $K_{I,i}$ are respectively the proportional and integral gains to be conveniently tuned. The resulting controlled transfer function ($GH(s)$) can be written as:

$$\begin{aligned} GH(s) &= GH_R(s)C_i(s) \\ &= K_{I,i}\frac{1 + s\tau_{r,i}}{s}\frac{sJ + B}{(s\tau_c + 1)[s^2JL_s + s(JR_s + BL_s) + R_sB + 4K_e^2]} \end{aligned} \tag{5.30}$$

The PI coefficients need to be tuned depending on the frequency response of the open loop transfer function ($GH_R(s)$); by means of the Bode plot analysis one could set predefined specifications in order to achieve fast and stable dynamic for the closed loop system. It must be noted that in the implementation of the PMBLDC drive model (*Figure 5.5*) any disturbance, such as the load torque, was neglected; this does not affect the stability of the closed loop system because of the existence of the integral gain which ensures an intrinsic disturbance rejection.
Firstly, the bode plot of the open loop transfer function ($GH_R(s)$) is considered; by looking at both the magnitude plot *Figure 5.7a* and the phase plot *Figure 5.7c* it can be noticed that the first two break points at low frequency (respectively of a zero and

a pole) are not affecting what happens at higher frequency. In fact, those two points are strictly related to the mechanical dynamic of the system (or the mechanical time constant J/B) which is inherently slow if compared to the typical electric dynamics.
In order to set properly the PI coefficients two important properties should be recalled:

1. The Bode plot of the controlled loop transfer function $GH(s) = GH_R(s)C_i(s)$ is nothing more than the sum of the two bode plots of $GH_R(s)$ and $C_i(s)$ respectively, for the magnitude and for the phase;
2. The requirement of fast dynamic and stability of the system are related respectively to: the bandwidth (BW_i) of the controlled transfer function (defined as the frequency at which the magnitude plot crosses the zero of the y-axis), and the phase margin (m_φ) of the controlled transfer function (defined as the phase which occurs at the BW_i frequency plus 180)

in particular, the higher the bandwidth BW_i the faster the dynamic and a typical specification for the phase margin m_φ is an angle between $45 \div 60$. An automatic code was implemented to perform the design of the PI controller according to specifications of BW_i and m_φ to be given as an input. In particular, the phase margin specification is set first to define the position of the zero (given by $1/\tau_{r,i}$) which belongs to the PI transfer function, and the the bandwidth specification decides the value of the proportional coefficient with respect to the integral one. It can be noticed from the phase plot of the PI controller (*Figure 5.7d*) that the effect on the closed loop transfer function is to shift the phase plot of the open loop transfer function (*Figure 5.7c*) of -90 until the break point of the controller occurs; this means that once the phase margin is decided (according to its definition) the bandwidth must be lower than a given value; in fact, the phase of the $GH_R(s)$ represents the upper limit for the phase that the controlled transfer function $GH(s)$ could have.

It is worth to notice that the two break points at high frequency for the open loop transfer function are very close to each other (*Figure 5.7a-Figure 5.7c*); those two break points are related to the electric time constant (τ_e) of the motor and to the commutation time constant (τ_c) of the inverter which are (referring to the data in Table 4.3):

$$\tau_e = \frac{L}{R} = 2.512^{-5} \quad ; \quad \tau_c = \frac{T_{sw}}{2} = \frac{1}{2 \cdot f_{sw}} = 2^{-5} \tag{5.31}$$

if one were to look only at the design of the PI controller, the relative position of the break point $1/\tau_e$ with respect to $1/\tau_c$ would not really affect the PI design procedure and nor the dynamic of the system when described with its transfer function form. The problem occurs when a physical meaning is given to the different transfer function blocks. As a matter of fact, having an electric time constant which is conveniently lower with respect to the commutation one is of paramount importance; in fact, it is worth bearing in mind that the commutation at the power inverter si needed to build the required current waveform (disregarding the type of waveform needed) and if the electric time constant is close to the switching period, then the current variation around the mean value, that the switching pattern is called to enforce, gets wider; this defines a high harmonic content in the current waveform, along with higher losses (as already

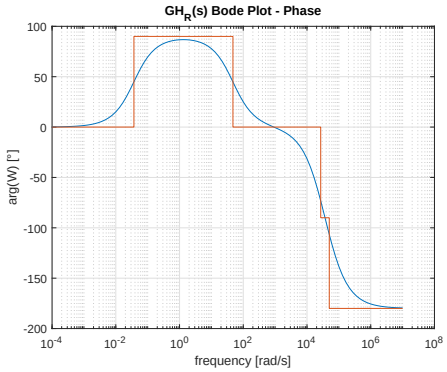

(a) $GH_R(s)$ magnitude plot,

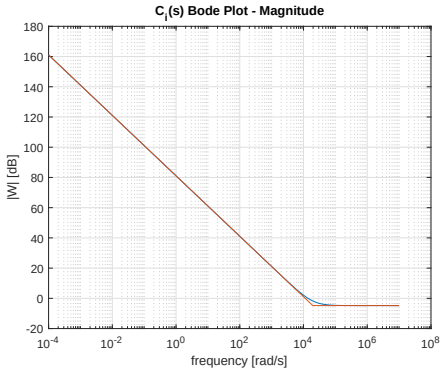

(b) $C_i(s)$ magnitude plot

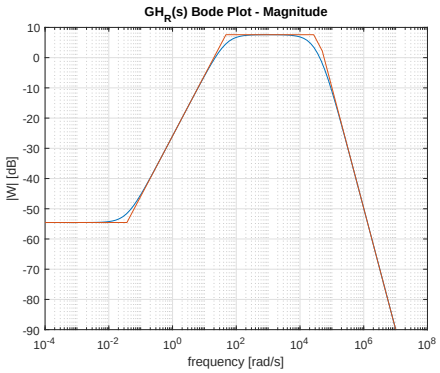

(c) $GH_R(s)$ phase plot

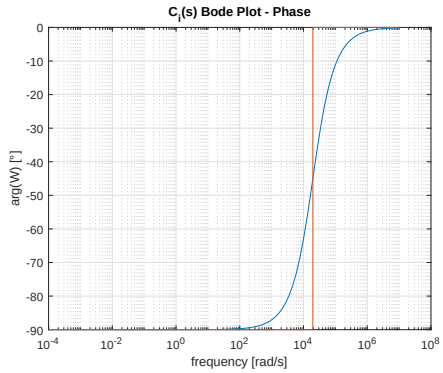

(d) $C_i(s)$ phase plot,

Figure 5.7: *$GH_R(s)$ and $C_i(s)$ asymptotic (red) and real (blue) Bode plot*

mentioned).

As it will be proved in the implementation of the electric drive considering the inverter switching, the operation of the motor considered in this work, under the predefined supply conditions, appears to be not acceptable in view of a high efficiency operation. For this reason the adoption of additional inductors is considered as a practical solution for the aforementioned problem.
In both of the cases (with and without additional inductors) the PI design is performed according to the following specifications:

$$\begin{cases} BW_i = \sqrt{\frac{1}{\tau_e} \cdot \frac{1}{\tau_c}} \\ m_\varphi = 60 \end{cases} \tag{5.32}$$

The solution with additional inductors requires to connect between the motor terminals and the inverter output an additional inductor for each phase; the inductance value for the filter inductor adopted for this work was $210\mu H$. As it will be mentioned, for this case study, a much smaller inductance could have been used. The bode plot of the open loop transfer function considering the additional inductors is shown in *Figure 5.8a* where the two breakpoints at high frequency ($1/\tau_e$ and $1/\tau_c$) are now one decade apart from each other.

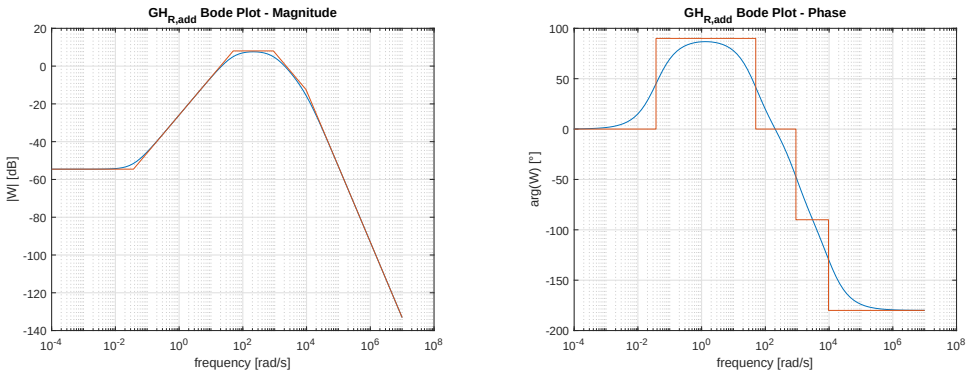

(a) $GH_{R,add}(s)$ magnitude plot, ***(b)*** $GH_{R,add}(s)$ phase plot

Figure 5.8: *$GH_{R,add}(s)$ asymptotic (red) and real (blue) Bode plots*

Parameter	Without additional inductors	With additional inductors
Bandwidth [rad/s]	37000	3035
Phase margin [deg]	60	60
Proportional coefficient [-]	0.7581	1.25
Integral coefficient $[s^{-1}]$	16089	2202

Table 5.1: *PI design data*

The resulting proportional and integral coefficients are reported in Table 5.1, along with the specifications for bandwidth and phase margin.

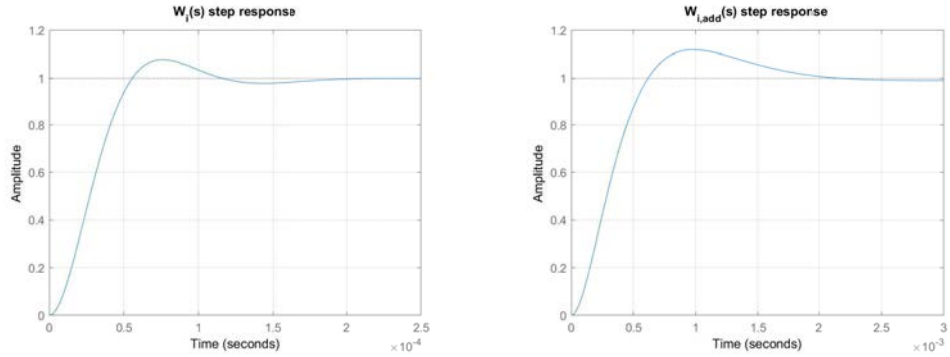

(a) $W_i(s)$ step response, ***(b)*** $W_{i,add}(s)$ step response,

Figure 5.9: *Step response for the current loop with and without additional inductors*

As a verification the code gives also the step response of the closed-loop transfer function($W_i(s)$) as an output *Figure 5.9*. As known from the control theory, the closed-loop transfer function can be expressed as:

$$W_i(s) = \frac{GH(s)}{1 + GH(s)H(s)} \tag{5.33}$$

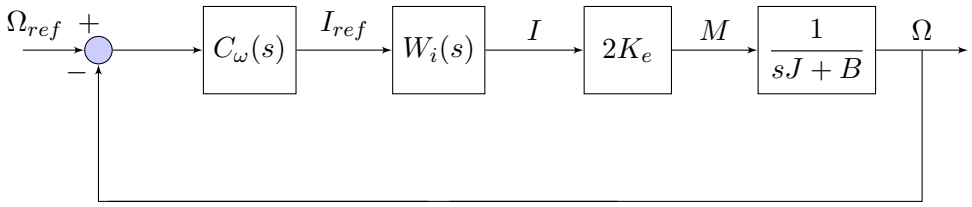

Figure 5.10: *Feedback speed loop*

where $H(s)$ is the feedback transfer function (in this case itis assumed to be a unitary gain).

In both cases a slight overshoot was accepted (since limited to less than 10%); it can be noted that the solution without additional inductors offers a faster dynamic because of the higher bandwidth of the current loop.
It is worth to point out that the increase in the switching frequency would lead to an increase in the upper limit of the bandwidth, and thus to a faster dynamic. The fast current variation is then transduced by the electric motor in fast torque variation; if this feature is coupled with a proper mechanical design with the aim of minimising the rotor inertia then the fast dynamic would be transmitted to the mechanical side as well. This type of performance could play a crucial role in those applications where fast motion is needed (CNC machining, 3D printing, robotics applications)

PI speed loop controller design The speed loop block diagram is represented in *Figure 5.9*. Considering the inherent complexity of an analytic expression for the current loop transfer function ($W_i(s)$); a simplified form can be defined to facilitate the design of the PI controller for the speed loop. For the purpose of simplifying the current loop transfer function in a general way, the Bode plots of the controlled transfer function ($GH(s)$) are considered (*Figure 5.10*) to study the asymptotic behaviour of the closed-loop transfer function ($W_i(s)$) as it follows:

$$W_i(s) = \frac{GH(s)}{1 + GH(s)H(s)} = \begin{cases} \frac{1}{H(s)} = 1 & \text{if } GH(s) \gg 1 \\ GH(s) & \text{if } GH(s) \ll 1 \end{cases} \tag{5.34}$$

in particular,at high frequency (i.e. when $GH(s) \ll 1$) it can be noticed that the controlled transfer function ($GH(s)$) behaves approximately as a second order system with two stable poles; considering, as it generally should be, that $\tau_c l \tau_e$ then the simplified version of the $W_i(s)$ can be written as:

$$W_i(s) = \frac{1}{(1 + s\frac{1}{BW_{i,[rad/s]}})(1 + s\tau_c)} \tag{5.35}$$

The speed loop non regulated transfer function ($GH_{R,\omega}$) is then given by:

$$GH_{R,\omega} = W_i(s)\frac{2K_e}{sJ + B} \tag{5.36}$$

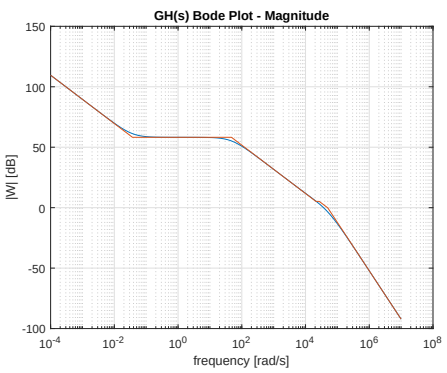

(a) $GH(s)$ magnitude plot,

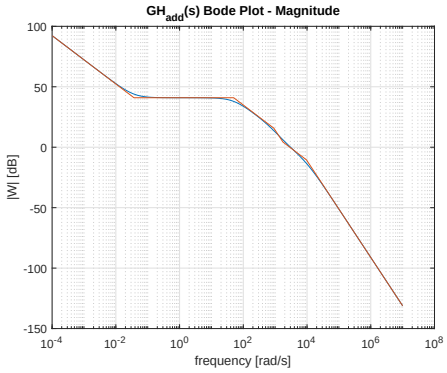

(b) $GH_{add}(s)$ magnitude plot

,

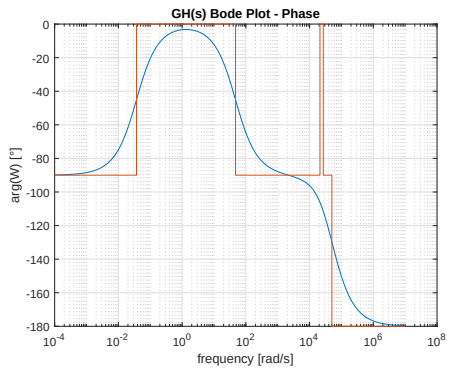

(c) $GH(s)$ phase plot

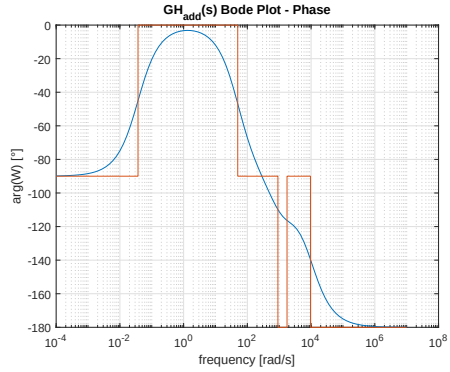

(d) $GH_{add}(s)$ phase plot,

Figure 5.11: *$GH(s)$ and $GH_{add}(s)$ asymptotic (red) and real (blue) Bode plot*

and for the two different cases (with and without additional inductors) the Bode plot of $GH_{R,\omega}(s)$ is depicted in *Figure 5.10*. From the same figure it can be noticed that the zero of the PI controller can be used to cancel the pole of the mechanical transfer function at low frequency, in order to get the maximum phase out of the controlled transfer function, and hence, having more margin to set the speed loop bandwidth.

The procedure implemented in the code for tuning the PI coefficients is the following:

1. The break point of the PI controller is set as:

$$\tau_{r,\omega} = \frac{K_{P,\omega}}{K_{I,\omega}} = \tau_m = \frac{J}{B}$$

2. The bandwidth for the speed loop is set equal to one fifth of the current loop bandwidth (considering that the worst case scenario would be having the two break points of $W_i(s)$ at the same frequency which would also mean having the electric time constant equal to the commutation one)

$$BW_\omega = \frac{BW_i}{5}$$

3. The position of the bandwidth is such that the magnitude contribution of $W_i(s)$ can be approximated at a unitary value ($0[dB]$) and the PI controller exhibit the

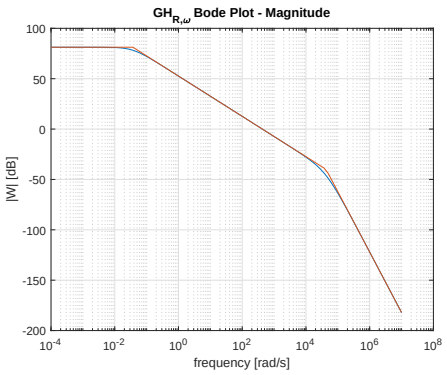

(a) $GH_{R,\omega}(s)$ magnitude plot,

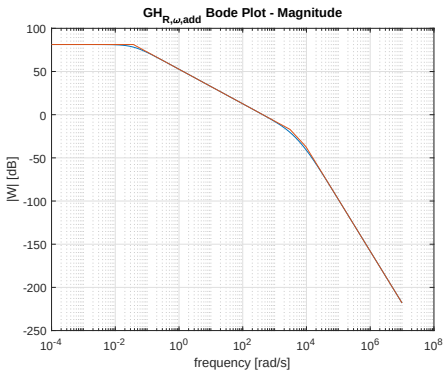

(b) $GH_{R,\omega,add}(s)$ magnitude plot

,

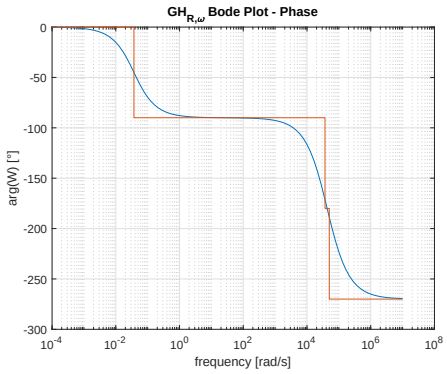

(c) $GH_{R,\omega}(s)$ phase plot

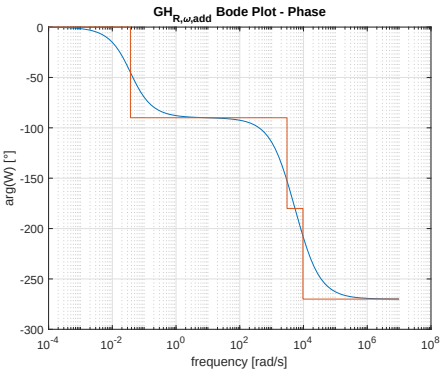

(d) $GH_{R,\omega,add}(s)$ phase plot,

Figure 5.12: *$GH(s)$ and $GH_{add}(s)$ asymptotic (red) and real (blue) Bode plot*

only effect of the proportional coefficient; therefore:

$$|GH(BW_\omega)| = \left|\frac{BW_\omega K_{P,\omega} + K_{I,\omega}}{BW_\omega}\right| \cdot |W_i(BW_\omega)| \cdot \left|\frac{2K_e}{BW_\omega J + B}\right|$$
$$\approx K_{P,\omega} \cdot 1 \cdot \frac{2K_e}{B}\frac{1}{BW_\omega \tau_m} = 1$$

4. The proportional and the integral coefficients can then be computed as:

$$K_{P,\omega} = \frac{J \cdot BW_\omega}{2K_e}$$
$$K_{I,\omega} = \frac{K_{P,\omega}}{\tau_{r,\omega}}$$

The resulting parameters for the speed loop controller are summarized in Table 5.2

Parameter	Without additional inductors	With additional inductors
Bandwidth [rad/s]	7137	4740
Phase margin [deg]	71	73.5
Proportional coefficient [-]	17.17	11.34
Integral coefficient [s^{-1}]	0.636	0.42

Table 5.2: *Speed loop PI parameters*

As done for the current loop the step response of the speed loop has been used as a verification of the method; the results are shown for both cases in *Figure 5.13*

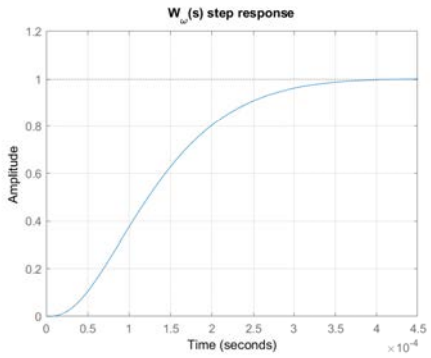

(a) $W_\omega(s)$ step response,

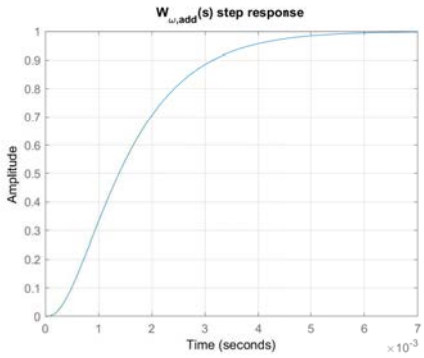

(b) $W_{\omega,add}(s)$ step response,

Figure 5.13: *Step response for the current loop with and without additional inductors*

5.2.2 Anti wind-up system

The step response of both the current loop and the speed loop shown respectively in *Figure 5.9* and *Figure 5.13*, are those that the system would have, if no limit was set for both current and supply voltage.
A phenomenon which may occur when a PI controller is regulating a system, where the output is bounded around limits, that are imposed according to physical constraints of the system itself,is the so called *wind-up*.
When the PI controller receives the error between the reference value and the measured one, the proportional part produce an output reference which is proportional to the error itself whereas the integral output is dependent on the amount of time in which the error persist; both effects are as intense as the relative gains (K_P,K_I) are high. The wind-up occurs typically in the speed loop; whenever the speed reference is such that the reference torque to be set (by the PI controller) is at its maximum value, the speed starts increasing linearly according to the mechanical dynamic of the system; meanwhile, the integral part of the controller stores the persisting error between reference speed and the measured one. As soon as the speed reaches the input reference the proportional output becomes zero but the integral one has reached its maximum value and it keeps acting by enforcing a torque reference which is no longer needed. If the proportional gain is much smaller with respect to the integral gain, and the speed dynamic is relatively slow, then the speed tend to overshoot with respect to the reference value. During the

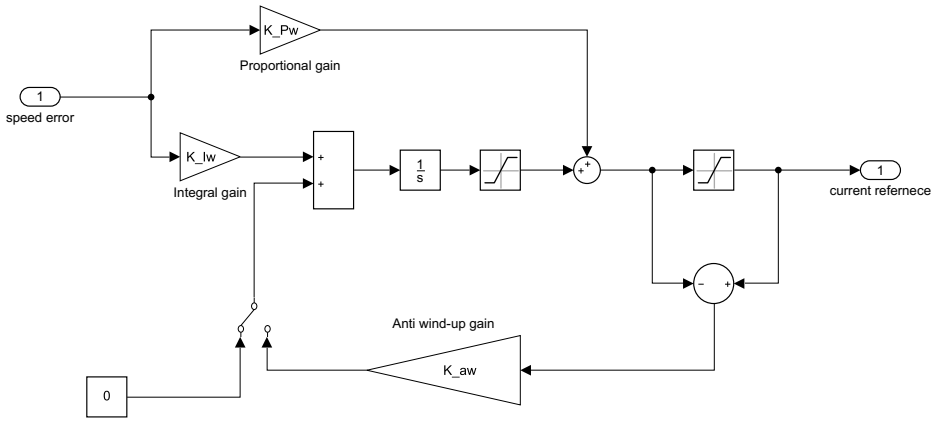

Figure 5.14: *PI controller with anti wind-up*

overshoot phase the proportional gain is acting in the opposite way with respect to the previous phase, and the integral decreases its effect until the maximum of the overshoot when the integral output goes to zero. After the maximum value has been reached, the integral starts storing an opposite error which could make the previous phenomenon to occur in the other direction.
The wind-up effect can compromise the stability of the system, and the speed can reach very high values during the overshooting phase. In order to verify if the drive system implemented in this work suffers this phenomenon, a Simulink® implementation of the transfer function based model, is proposed for the introduction of the operation limits and the anti wind-up system. In *Figure 5.14* the PI controller with the anti wind-up system is shown; the two saturation blocks ensures that neither the whole PI controller and nor the integral alone can exceed the motor current limit. In particular the second saturation block is used to activate the anti wind-up action when the PI controller output is higher than the maximum allowed value; the effect is a mitigation of the integral output even for those cases in which the proportional effect alone would exceed the limits.

The model has been solved by setting a reference speed of 10000[rpm] (maximum speed of the motor) and the resulting speed response with the anti wind-up disabled is shown in *Figure 5.15*. It is clear that the system does not show any wind-up effect, and therefore, the anti wind-up system will be left disabled for all the different simulations. The fact that the system is not prone to the wind-up effect can be explained by considering the PI parameters in Table 5.2 However, considering the PI values reported in Table 5.2 where it can be noticed that the integral coefficient is smaller than the

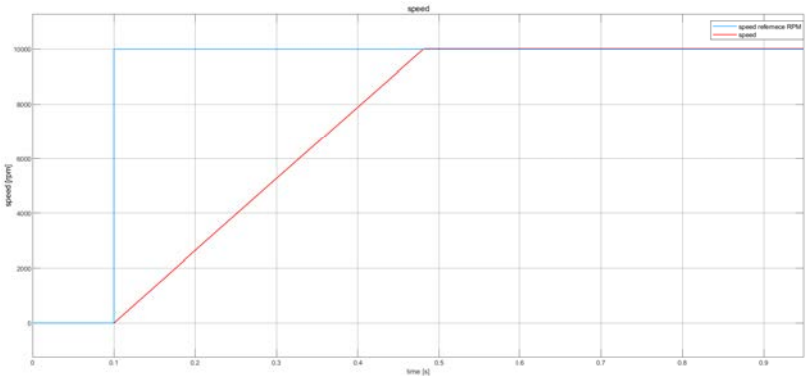

Figure 5.15: *Speed response without anti wind-up*

proportional.

5.3 MATLAB-Simulink® Implementation -*PWM Trapezoidal Control*-

As already mentioned, in this work the only unipolar (soft) PWM switching control is implemented which means that the PWM is applied only to the leg in which the upper switch is turned on (i.e. the leg of the phase which carries a positive current) . In [4] the implementation of the bipolar (hard) PWM switching is described as well. The choice of implementing the unipolar control is mainly due to the fact that it produces less ripple with respect to the bipolar one. However, the implementation that will be described in the following does not allow the brake operation of the motor; therefore, a one quadrant operation is considered.
The whole electric drive system is implemented in Simulink®; the speed and current controller coefficients are given as an output of the same Matlab® code which loads the useful parameters for the drive model to be solved. The current controller gives a reference signal, as an output, which is used to produced the PWM signal for the inverter.

The switching at the power converter is implemented in a Matlab® function which gives directly the input needed from the motor model (implemented as (5.23)).
The switching pattern is implemented considering both the electric circuit scheme of the inverter fed three-phase motor (power inverter *Figure 3.2*), and the conduction states for the trapezoidal control (Table 3.1); the latter ones, in particular, are the conduction states which occur when the PWM signal is high. The output voltage applied by the power inverter, is affected by the commutation phenomenon between two states.
Considering the interval $0° \div 60°$ as an example, at $0°$ the switch S1 is turned on and S6 is turned off; the current "ic" was negative and it takes some time to drop at a zero value. The operating circuit of the power inverter, within this time interval, can be represented as in *Figure 5.16*

The circuit can be solved with the loop current method, and the diode can be replaced with an equivalent voltage which is zero when $ic \neq 0$, and when $ic = 0$ is such that the current in that loop is zero. In this way, the input voltage to the state space

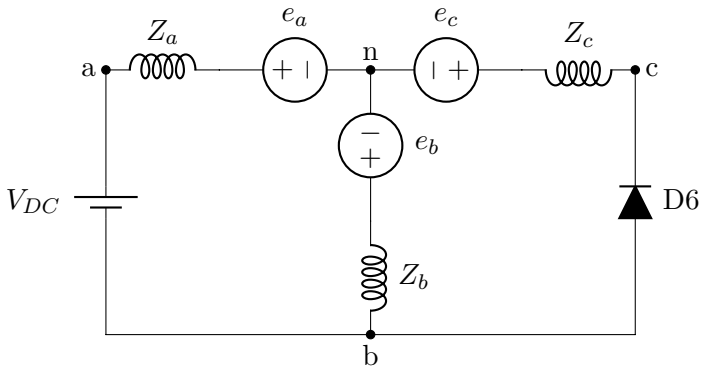

Figure 5.16: *Equivalent circuit between* $0° \div 60°$ *with high PWM signal*

Electric angle interval	Diode current	$v_{ab} - e_{ab}$	$v_{bc} - e_{bc}$
$0° \div 60°$	$i_c \neq 0$	$V_{DC} - e_{ab}$	$-e_{bc}$
	$i_c = 0$	$V_{DC} - e_{ab}$	$(e_{ab} - V_{DC})/2$
$60° \div 120°$	$i_b \neq 0$	$-e_{ab}$	$V_{DC} - e_{bc}$
	$i_b = 0$	$(V_{DC} - e_{ac})/2$	$(V_{DC} - e_{ac})/2$
$120° \div 180°$	$i_a \neq 0$	$-V_{DC} - e_{ab}$	$V_{DC} - e_{bc}$
	$i_a = 0$	$(e_{bc} - V_{DC})/2$	$V_{DC} - e_{bc}$
$180° \div 240°$	$i_c \neq 0$	$-V_{DC} - e_{ab}$	$-e_{bc}$
	$i_c = 0$	$-V_{DC} - e_{ab}$	$(V_{DC} + e_{ab})/2$
$240° \div 300°$	$i_b \neq 0$	$-e_{ab}$	$-V_{DC} - e_{bc}$
	$i_b = 0$	$(-V_{DC} - e_{ac})/2$	$(-V_{DC} - e_{ac})/2$
$300° \div 360°$	$i_a \neq 0$	$V_{DC} - e_{ab}$	$-V_{DC} - e_{bc}$
	$i_a = 0$	$(V_{DC} + e_{bc})/2$	$-V_{DC} - e_{bc}$

Table 5.3: *Input voltages at the motor state space model when PWM=1*

model of the motor can be found for any switching interval. The voltages needed as inputs for the motor model, when the PWM signal is high, are summarized in Table 5.3

On the other hand, the same analysis needs to be performed when the PWM signal is low (PWM=0). Considering again the interval $0° \div 60°$; the current in the phase "a" can be either zero or positive and in both these two cases, the current in the phase "c" can be different from zero because of the commutation from the previous conduction phase. The circuit to be solved in this interval is shown in *Figure 5.16*.

the solution of the circuit related to each conduction interval, when the PWM signal is low, brings to the results reported in Table 5.4

The Simulink® subsystem of the inverter is shown in *Figure 5.18*, where the "*Interpreted MATLAB Fcn*" calls the function in which Table 5.3 and 5.4 are implemented depending on all the inputs shown. In particular, the input "*currents*" is the output of a relay block which says when each of the currents is either equal to or different from zero (as this is the information needed for defining the inverter output)

The inverter output is given as an input to the motor state space model (*Fig-*

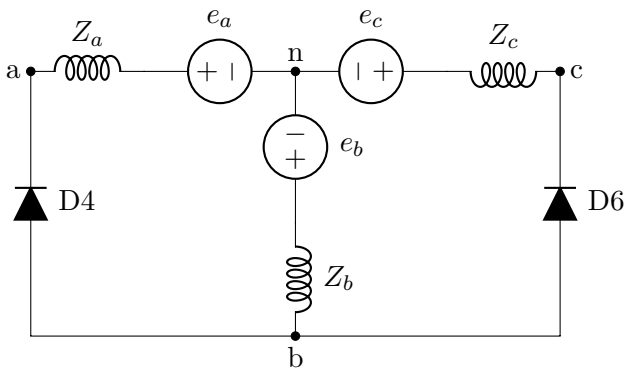

Figure 5.17: *Equivalent circuit between* $0° \div 60°$ *with low PWM signal*

Electric angle interval	Diode current	$v_{ab} - e_{ab}$	$v_{bc} - e_{bc}$
$0° \div 60°$	$i_a \neq 0, i_c \neq 0$	$-e_{ab}$	$-e_{bc}$
	$i_a \neq 0, i_c = 0$	$-e_{ab}$	$e_{ab}/2$
	$i_a = 0, i_c \neq 0$	$e_{bc}/2$	$-e_{bc}$
	$i_c = 0, i_c = 0$	0	0
$60° \div 120°$	$i_a \neq 0, i_c \neq 0$	$-V_{DC} - e_{ab}$	$V_{DC} - e_{bc}$
	$i_a \neq 0, i_c = 0$	$-e_{ac}/2$	$-e_{ac}/2$
	$i_a = 0, i_c \neq 0$	$(e_{bc} - V_{DC})/2$	$V_{DC} - e_{bc}$
	$i_c = 0, i_c = 0$	0	0
$120° \div 180°$	$i_a \neq 0, i_c \neq 0$	$-e_{ab}$	$-e_{bc}$
	$i_a \neq 0, i_c = 0$	$e_{bc}/2$	$-e_{bc}$
	$i_a = 0, i_c \neq 0$	$-e_{ac}/2$	$-e_{ac}/2$
	$i_c = 0, i_c = 0$	0	0
$180° \div 240°$	$i_a \neq 0, i_c \neq 0$	$-e_{ab}$	$-V_{DC} - e_{bc}$
	$i_a \neq 0, i_c = 0$	$-e_{ab}$	$e_{ab}/2$
	$i_a = 0, i_c \neq 0$	$(-V_{DC} - e_{ac})/2$	$(-V_{DC} - e_{ac})/2$
	$i_c = 0, i_c = 0$	0	0
$240° \div 300°$	$i_a \neq 0, i_c \neq 0$	$-e_{ab}$	$-e_{bc}$
	$i_a \neq 0, i_c = 0$	$-e_{ac}/2$	$-e_{ac}/2$
	$i_a = 0, i_c \neq 0$	$-e_{ab}$	$-e_{ab}/2$
	$i_c = 0, i_c = 0$	0	0
$300° \div 360°$	$i_a \neq 0, i_c \neq 0$	$V_{DC} - e_{ab}$	$-e_{bc}$
	$i_a \neq 0, i_c = 0$	$-e_{bc}/2$	$-e_{bc}$
	$i_a = 0, i_c \neq 0$	$V_{DC} - e_{ab}$	$(-V_{DC} + e_{ab})/2$
	$i_c = 0, i_c = 0$	0	0

Table 5.4: *Input voltages at the motor state space model when PWM=0*

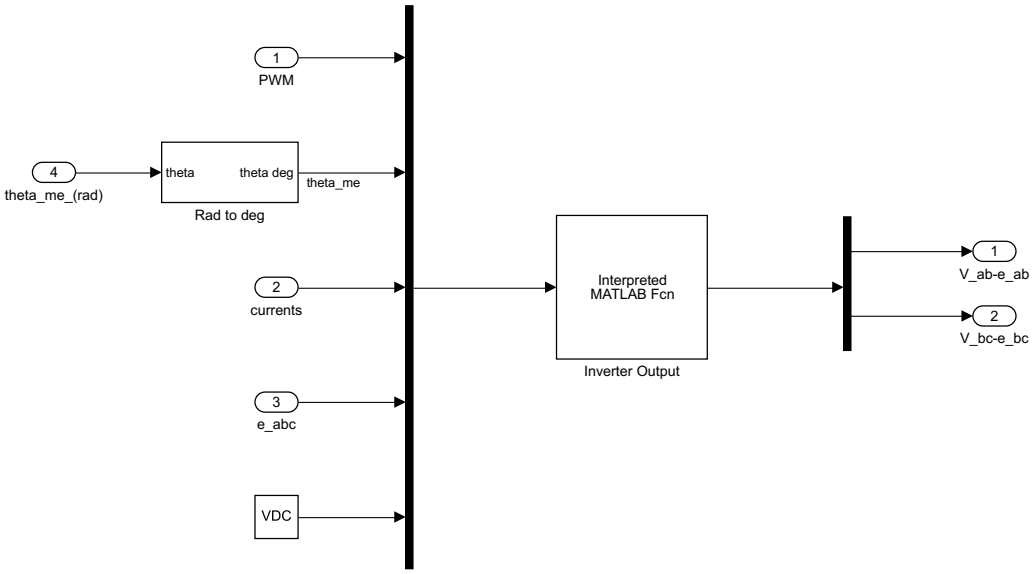

Figure 5.18: *Inverter subsystem*

ure 5.19), along with motor and load torque.
The output currents, speed and position are used for defining the torque (5.19), the trapezoidal back-emfs (5.5) and all the feedbacks needed for the model to operate. It is worth to point out that the current feedback in the model is given as the absolute value of the sum of the three currents, which is (according to the control algorithm) the input DC current; this is one advantage of the trapezoidal control which would require to sense only the DC input current (for control purpose).

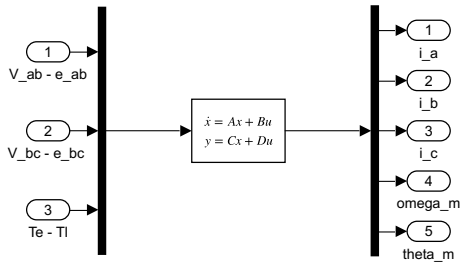

Figure 5.19: *Motor subsystem*

5.3.1 Simulation Results of the BLDC Drive System

The model was solved with a step reference speed of 2500$[rpm]$ and a load torque of 0.2$[Nm]$ acting at 0.11$[s]$. The results for the two different solutions (without ad with additional inductors) are shown and discussed in the following.
Firstly the speed response of the system is shown in *Figure 5.20*; the dynamic is relatively slow if compared with other slotless machines, and this is due to both a relatively high inertia and a low maximum torque.

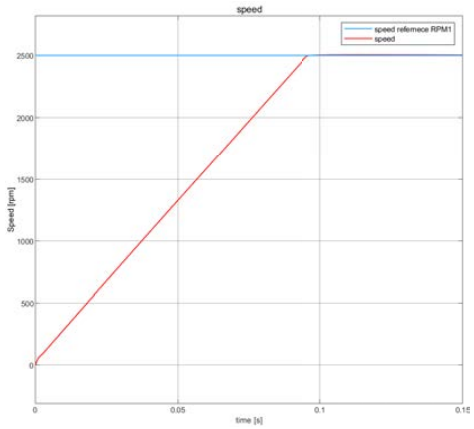

Figure 5.20: *Speed response*

In *Figure 5.21* the resulting current waveforms in the three phases are shown. *Figure 5.21a* and *Figure 5.21b* show the currents for in the whole simulation in the first phase when the motor is accelerating the current is kept at its maximum value until when the speed reaches the reference value, and then, at $0.11[s]$ when the reference torque is applied, the current rises up to the value decided by the controller. As it was already mentioned, the solution without additional inductors produces a wide ripple band around the mean value of the current to be set; furthermore, an increase in the ripple band can be noticed as long as the speed keeps increasing. This phenomenon is due to both an increase in the back-emf which causes a faster current variation and to the response of the current controller to the previous effect, i.e. the PI current controller detects the faster current variation (because of the higher back-emf) and tries to recover this effect by increasing the duty cycle (time in which PWM=1 in the switching period) but the low electric time constant leads to a fast current variation on the opposite direction, and hence, the controller reduces the duty cycle again, but since the beck-emf keeps increasing, then this phenomenon repeats itself in a loop that lead to the increase in the ripple band. This behaviour needs to be considered when fast acceleration at very high speed are demanded from the system, in order to avoid high current values. A possible solution can be to conveniently reduce the dynamic of the current controller.
Even though, the solution with additional inductors shows a much lower current ripple around the switching frequency, it tends to increase the commutation effect typical for this type of control as shown in *Figure 5.21d* where the response of the controller to the commutation effect is also represented; in fact, those current spikes would disappear if the current controller was designed in order to have no overshoots.

Finally, the torque response for the two different solutions are shown in *Figure 5.22*. In particular, *Figure 5.22a* highlights the fact that for the implemented control algorithm a negative torque is not allowed. Moreover the torque ripple follows current ripple leading to a wide ripple band for the solution without inductors, and an amplified commutation effect for the solution with additional inductors, along with torque spikes due to the controller response.

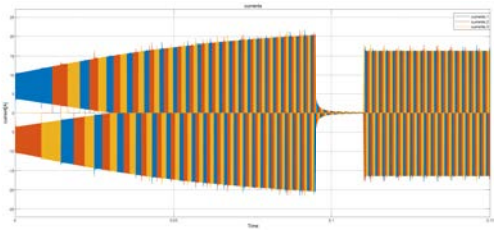

(a) Three-phase current waveform,

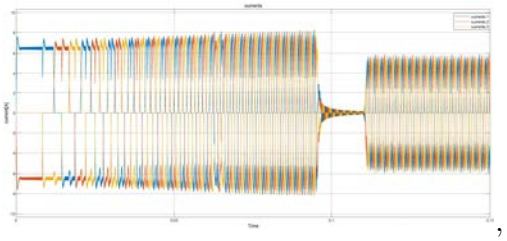

(b) Three-phase current waveform with additional inductors

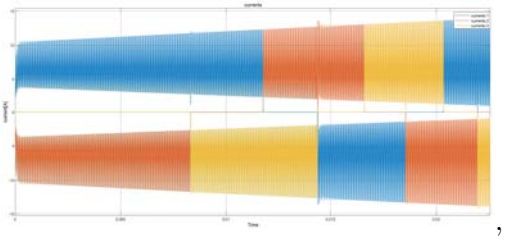

(c) Currents during the starting phase

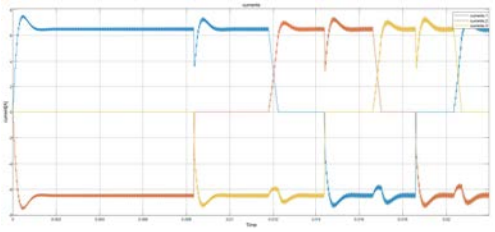

(d) Currents during the starting phase with additional inductors,,

Figure 5.21: *Current waveforms with and without additional inductors*

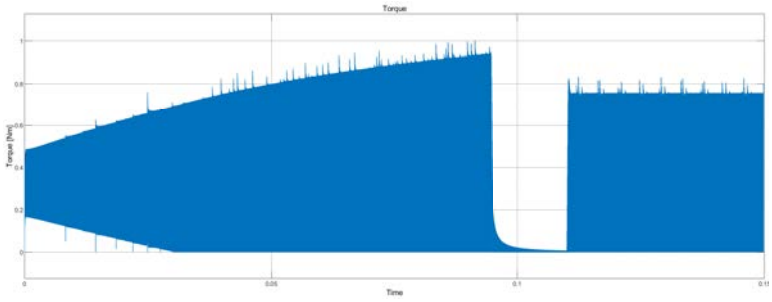

(a) Resulting torque,

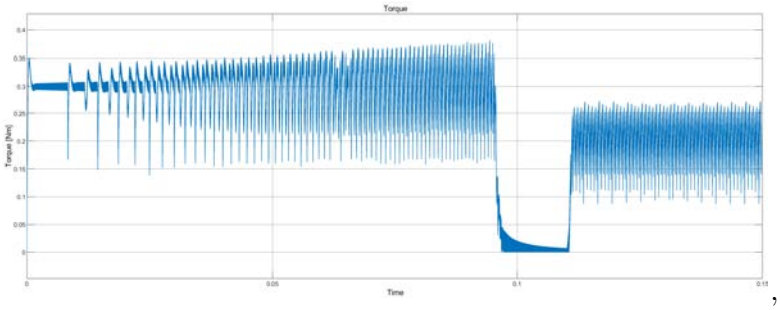

(b) Resulting torque with additional inductors

Figure 5.22: *Torque profiles with and without additional inductors*

Chapter 6

PM Synchronous Motor Drives Modelling

From the previous chapter, the inherent limitations of a BLDC motor control arise as a non-smooth torque response due to either switching ripple or commutation effect; though, a convenient choice for the additional inductors, with the aim of minimizing both the effects, could improve the performance. The main advantage of using the trapezoidal control algorithm is related to the fairly ease of implementation; even though it does not seem intuitive by looking at the model implementation, in a practical case the inverter switching is commanded by conveniently handling the signals from the Hall effect sensors.
In this chapter the typical control of a PM synchronous motor (PMSM) is described, along with the implementation of the related drive model.

6.1 Permanent Magnet Synchronous Motor Modelling

As already mentioned in Section 5.1 the state space model implemented for the BLDC motor is actually valid for any kind of brush-less three-phase PM motor; the only difference lies in the back-emf expression. As already mentioned, a PMSM is designed in order to get a sinusoidal back-emf, and hence, a sinusoidal flux linkage distribution at the air-gap. In (6.1) the flux expressions are explicitly written as a function of the electrical coordinate ϑ_{me}.

$$\begin{cases} \lambda_{a,mg} = \Lambda_{mg} \cdot \cos \vartheta_{me} \\ \lambda_{b,mg} = \Lambda_{mg} \cdot \cos(\vartheta_{me} - 2\pi/3) \\ \lambda_{c,mg} = \Lambda_{mg} \cdot \cos(\vartheta_{me} + 2\pi/3) \end{cases} \tag{6.1}$$

For the sake of completeness, the explicit back-emf equation for each phase is ad-

dressed in the following

$$\begin{cases} e_a = \omega_{me} \cdot \Lambda_{mg} \cdot \cos(\vartheta_{me} + \pi/2) \\ e_b = \omega_{me} \cdot \Lambda_{mg} \cdot \cos(\vartheta_{me} + \pi/2 - 2\pi/3) \\ e_c = \omega_{me} \cdot \Lambda_{mg} \cdot \cos(\vartheta_{me} + \pi/2 + 2\pi/3) \end{cases} \tag{6.2}$$

The amplitude of the back-emf can be related to the back-emf constant as done for the BLDC machine. According to its definition, the back-emf constant can now be expressed as:

$$K_e = p \cdot \Lambda_{mg} \tag{6.3}$$

Ideally, the control of a PMSM would produce a three-phase sinusoidal current waveform; thus, the expressions for the three currents can be written as in (6.4), where a certain displacement (ψ) with respect to the back emfs is considered, along with a variable peak current value ($I_M(t)$) decided by the controller.

$$\begin{cases} i_a = I_M(t) \cdot \cos(\vartheta_{me} + \pi/2 - \psi) \\ i_b = I_M(t) \cdot \cos(\vartheta_{me} + \pi/2 - 2\pi/3 - \psi) \\ i_c = I_M(t) \cdot \cos(\vartheta_{me} + \pi/2 + 2\pi/3 - \psi) \end{cases} \tag{6.4}$$

Therefore the torque equation in (5.18) can be explicitly written considering (6.2) and (6.4) as it follows:

$$\begin{aligned} m = p \cdot \Lambda_{mg} (& \cos(\vartheta_{me} + \pi/2) \cdot \cos(\vartheta_{me} + \pi/2 - \psi) + \\ & \cos(\vartheta_{me} + \pi/2 - 2\pi/3) \cdot \cos(\vartheta_{me} + \pi/2 - 2\pi/3 - \psi) + \\ & \cos(\vartheta_{me} + \pi/2 + 2\pi/3) \cdot \cos(\vartheta_{me} + \pi/2 + 2\pi/3 - \psi)) \end{aligned} \tag{6.5}$$

developing the product between the sinusoidal functions leads to the following result:

$$m = \frac{3}{2} \cdot p \cdot \Lambda_{mg} \cdot I_M(t) \cdot \cos(\psi) \tag{6.6}$$

It is important to notice that if the current is controlled in such a way that $\psi = 0$, i.e. the current and back-emf of a given phase are in-phase with each other, then the maximum motor torque can be achieved; this type of control is also known as Maximum Torque Per Ampere (MTPA). From the same equation, the torque constant Km (defined as torque in $[Nm]$ per phase current in $[A_{rms}]$) can be defined as:

$$K_m = \frac{3}{\sqrt{2}} \cdot p \cdot \Lambda_{mg} = \frac{3}{\sqrt{2}} \cdot K_e \tag{6.7}$$

It is already clear that the control would need an accurate and, most importantly, continuous speed/position detection of the rotor, in order for the inverter to set the

correct current reference for each phase at any switching interval. This means that Hall effect sensors are no longer enough for speed/position sensing. Typically the sensors used for this type of control are either encoders or resolvers, both of which ensures higher resolution if compared to Hall effect sensors; however they also represent a more expensive and bulky solution.

6.2 PMSM Model in a Rotating Reference System

If the system to be controlled was the one explained beforehand, then the control would deal with time varying currents (sinusoidal); this means that the reference values that the PI or PID currents controllers are called to handle, are no longer constant (as it was for the BLDC control); in this regard, the design of the controllers gets more tedious [28].

When studying three-phase electrical systems, the introduction of *Clarke* and *Park* transformations represents a useful way for simplifying the system analysis. With the former transformation one is able to represents the three quantities (being them currents or voltages) into a vector with two components, rotating synchronously with the electrical frequency of the original quantities (as explained in appendix C).On the other hand, the Park transformation takes a further step for defining the same three quantities as a vector in a reference system which is rotating synchronously with the electrical quantities. In this way the vector appears to be fixed and the magnitude is decided by the peak of the three-phase quantities to be represented (as proved in appendix D). In particular, considering the voltage equation for a three-phase PM machine in (5.13) with the magnet flux that now is sinusoidal, by means of the Clarke transformation it can be rewritten as:

$$\begin{cases} v_\alpha = R \cdot i_\alpha + L\frac{di_\alpha}{dt} + \frac{d\lambda_{\alpha,mg}}{dt} = R \cdot i_\alpha + L\frac{di_\alpha}{dt} - \omega_{me}\Lambda_{mg}\sin(\theta_{me}) \\ v_\beta = R \cdot i_\beta + L\frac{di_\beta}{dt} + \frac{d\lambda_{\beta,mg}}{dt} = R \cdot i_\beta + L\frac{di_\beta}{dt} + \omega_{me}\Lambda_{mg}\cos(\theta_{me}) \end{cases} \tag{6.8}$$

which can be written in vector form as:

$$\mathbf{v}_{\alpha\beta} = R \cdot \mathbf{i}_{\alpha\beta} + L \cdot \frac{d\mathbf{i}_{\alpha\beta}}{dt} + j\omega_{me}\boldsymbol{\lambda}_{mg,\alpha\beta} \tag{6.9}$$

the latter equation can be easily referred to a rotating reference frame synchronous with the electrical frequency ω_{me}(considering (D.3)):

$$\begin{aligned} \mathbf{v}_{\alpha\beta} = \mathbf{v}_{dq}e^{j\theta_{me}} &= R \cdot \mathbf{i}_{dq}e^{j\theta_{me}} + L \cdot \frac{d}{dt}(\mathbf{i}_{dq}e^{j\theta_{me}}) + j\omega_{me}\boldsymbol{\lambda}_{mg,dq}e^{j\theta_{me}} \\ &= R \cdot \mathbf{i}_{dq}e^{j\theta_{me}} + L \cdot \frac{d\mathbf{i}_{dq}}{dt} \cdot e^{j\theta_{me}} + j\omega_{me}L \cdot \mathbf{i}_{dq}e^{j\theta_{me}} + j\omega_{me}\boldsymbol{\lambda}_{mg,dq}e^{j\theta_{me}} \end{aligned} \tag{6.10}$$

and the magnets flux in the dq system becomes:

$$\boldsymbol{\lambda}_{mg,dq} = \boldsymbol{\lambda}_{mg,\alpha\beta} e^{-j\theta_{me}} = \Lambda_{mg} e^{j\theta_{me}} e^{-j\theta_{me}} = \Lambda_{mg} \tag{6.11}$$

Therefore, the two voltage components in the dq reference frame can be expressed as:

$$\begin{cases} v_d = Ri_d + L\dfrac{i_d}{dt} - \omega_{me} L i_q \\ v_q = Ri_q + L\dfrac{i_q}{dt} - \omega_{me}(L i_d + \Lambda_{mg}) \end{cases} \tag{6.12}$$

it can be proved that the torque equation in the dq reference frame can be written as:

$$m = \frac{3}{2} \cdot p \cdot \Lambda_{mg} \cdot i_q \tag{6.13}$$

which shows that the only q component of the current is relevant for the torque generation; therefore, for a given current value, having the current in phase wit the back-emf lead to the maximum torque (MTPA operation).
It is worth to notice that now both currents and voltages are constant values if the dq system is kept synchronous with the electrical quantities. This means that the PI controllers can be designed with the same procedure adopted for the BLDC machine. This is a relevant advantage when comparing a control in the rotating reference frame with respect to the control in the time domain. However, this advantage is not "price-less" in fact a microcontroller is called to perform more operations (considering the transformations needed to pass from time domain, where the quantities are measured, to the different reference systems -$\alpha\beta$ and dq-), and, as already mentioned, the speed/position detection needs to be fast enough in order for the algorithm to be effective.

6.2.1 PI Controllers Design in the *dq* System

Before describing the design procedure adopted for the PI controllers in the dq domain, an intermediate step should be taken, in order to use the same approach which was adopted for the BLDC machine. In *Figure 6.1* the representation of the PMSM in the dq domain is shown (accordingly to (6.12) and (6.13)). The existence of the multiplication blocks (in the coupling section) makes the system non linear; moreover, the coupling between the d loop and the q loop makes the definition of two independent loop not possible.

The operation to define a model without cross-coupling between the two axes is called dq decoupling control and there are different ways of implementing it [21]. Assuming a decoupling technique applied to the case study, than the two open loops can be represented as depicted in *Figure 6.2* for the q-axis and *Figure 6.3* for the d-axis;

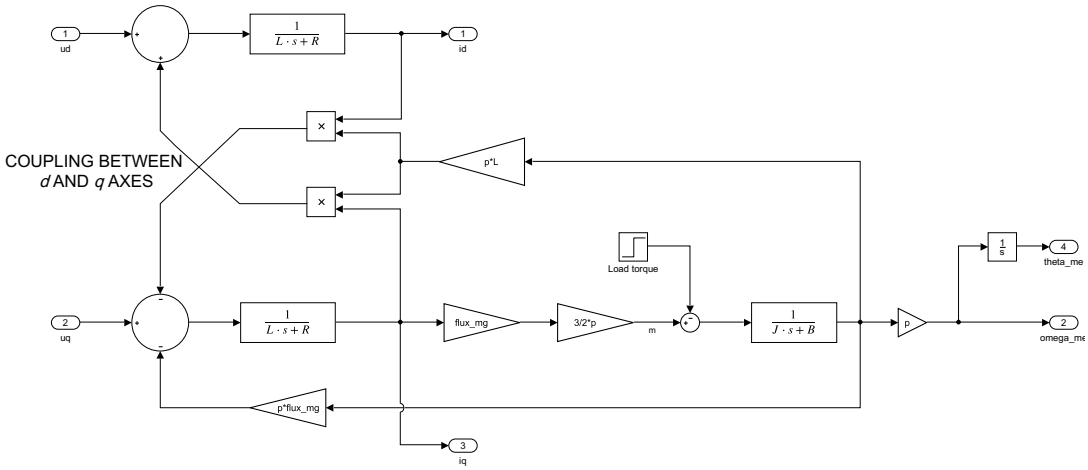

Figure 6.1: *Transfer function based model of a PMSM in the dq domain*

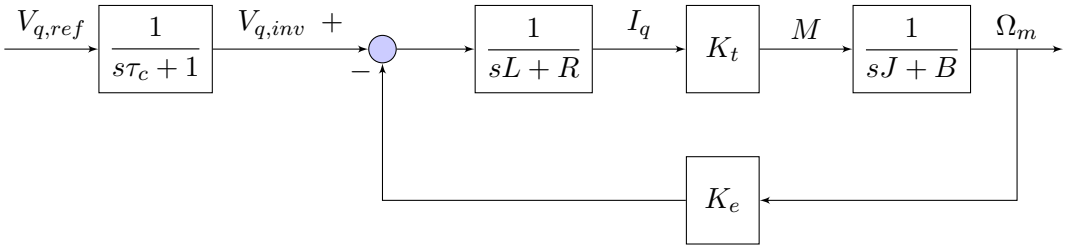

Figure 6.2: *Open loop q-axis model after decupling*

the speed loop interacts only with the q axis (as long as a MTPA operation is ensured); therefore, the design of both speed controller and the q-axis current controller follows the same procedure adopted for the BLDC machine (5.2.1,5.20) by conveniently adapting the parameters to define each transfer function block. The same procedure is also used for designing the d-axis current controller; in this case, the plain expression of the open loop non-controlled transfer function $GH_{R,d}$ (explicitly reported in (6.14)), simplifies the design procedure.

$$GH_{R,d} = \frac{1}{s\tau_c + 1}\frac{1}{sL + R} \tag{6.14}$$

The PMSM model is used in this work as a comparison with experimental results. The experimental setup includes connections for current measurements that affect mainly the inductance value seen from the inverter. For this reason the "phase" inductance of the motor is increased up to $7.75[\mu H]$ from the original $5.75[\mu H]$ reported in Table 4.3; this choice will be explained when describing the experimental setup.

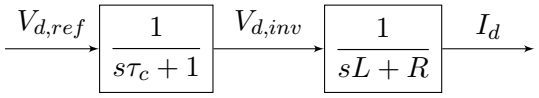

Figure 6.3: *Open loop d-axis model after decupling*

Parameter	Speed loop		q-axis current loop		d-axis current loop	
	Without additional inductors	With additional inductors	Without additional inductors	With additional inductors	Without additional inductors	With additional inductors
Bandwidth [rad/s]	7137	595	36720	3035	36720	3035
Phase margin [deg]	70.9	75.4	60	60	60	60
Proportional coefficient [-]	8.09	0.67	0.3791	0.627	0.3794	0.63
Integral coefficient $[s^{-1}]$	0.3	0.025	8044	1102	8043	1103

Table 6.1: *PMSM PI controllers parameters*

The design of the PI controllers as explained has been implemented in an automatic code and the results are addressed in Table 6.1; as done for the BLDC implementation, the code gives the step response for the different loops. Being the systems of the same type and the specifications for Bandwidth and phase margin equal to the BLDC case, the step responses for the different loops are the same. It is worth to notice that the PI gains for both the d and q current loops are almost equal; this is due to the slow mechanical dynamic, which does not affect the design the design of the current controllers, and also the low back-emf constant (K_e) gives a contribution which is negligible in the q loop.

6.3 MATLAB-Simulink® Implementation -*PMSM Space Vector Modulation*-

The control of a power inverter, in order to obtain a sinusoidal current as an output, is usually explained by means of the first type of implementation for this type of control where the firing signals for the switches where given as a result of an analogue comparison between two signals: the *reference* (sinusoidally varying at the frequency wanted as an output) and the carrier (typically a triangular wave varying at the switching frequency). Starting from that implementation different control algorithms have been introduce with in order to achieve distinct goals such as: reducing the number of commutation in time, reducing the harmonic content in the output current, and being more adequate for digital systems.
The Space Vector Modulation (SVM) is named after the fact that the three legs at the power inverter are control independently in order to get a certain voltage vector as an output in the transformed $\alpha\beta$ domain, as such, having three legs with two possible states each leads to the capability of representing $2^3 = 8$ different vectors.
In order to understand the values that these vectors can assume the general circuit represented in *Figure 3.2* needs to be considered. Taking as a reference firing signal the one which is sent to the upper switch of each leg (S1,S2,S3) and knowing that the lower ones are controlled in a complementary manner; considering as an example the state (1,0,0),this will produce:

$$v_{aO} = V_{DC} \quad ; \quad v_{bO} = 0 \quad ; \quad v_{cO} = 0 \tag{6.15}$$

these three voltages can be represented as a vector $\boldsymbol{v}_1$ in the transformed domain

Space vector	Switching state	On state switch	Vector definition
V_1	(1,0,0)	S1,S5,S6	$\frac{2}{3}V_{DC}e^{j0}$
V_2	(1,1,0)	S1,S2,S6	$\frac{2}{3}V_{DC}e^{j\pi/3}$
V_3	(0,1,0)	S4,S2,S6	$\frac{2}{3}V_{DC}e^{j2\pi/3}$
V_4	(0,1,1)	S4,S2,S3	$\frac{2}{3}V_{DC}e^{j\pi}$
V_5	(0,0,1)	S4,S5,S3	$\frac{2}{3}V_{DC}e^{j4\pi/3}$
V_6	(1,0,1)	S1,S5,S3	$\frac{2}{3}V_{DC}e^{j5\pi/3}$
V_7	(1,1,1)	S1,S2,S3	0
V_0	(0,0,0)	S4,S5,S6	0

Table 6.2: *Inverter output voltages in the transformed $\alpha\beta$ domain*

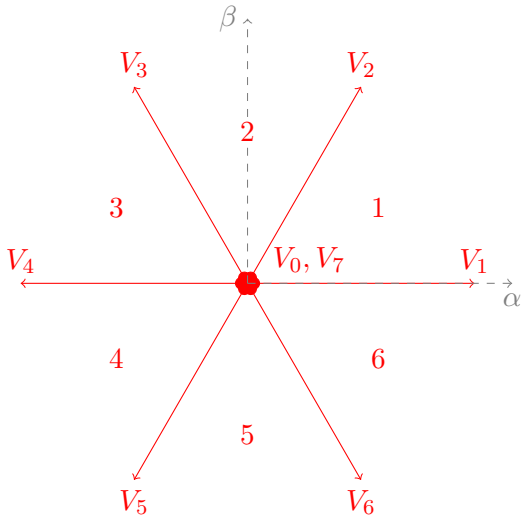

Figure 6.4: *Inverter output voltages in the transformed $\alpha\beta$ domain*

$\alpha\beta$ by means of the Clarke transformation (C.1) as:

$$\begin{aligned} \boldsymbol{v}_1 = v_\alpha + jv_\beta &= \frac{2}{3}\left(v_{aO} - \frac{1}{2}v_{bO} - \frac{1}{2}v_{cO}\right) + j\frac{2}{3}\left(\frac{\sqrt{3}}{2}v_{bO} - \frac{\sqrt{3}}{2}v_{cO}\right) \\ &= \frac{2}{3}V_{DC} + j0 \end{aligned} \tag{6.16}$$

in a similar manner considering all the different states (among the eight possible) one can define eight vectors in the $\alpha\beta$ domain as summarised in Table 6.2 and graphically in *Figure 6.4*

In so far as at any instant a three-phase voltage can be represented as a vector in $\alpha\beta$, then it means that the inverter can receive a reference voltage as a vector in the same domain, and translate it conveniently into a sequence of commutations with the aim of representing that very vector. The latter statement is the logic behind the SVM technique.

In particular, the inverter is called to represent the reference vector in within any switching period. This means that in this time interval, the inverter will switch between some different states in order to place the output vector anywhere in the $\alpha\beta$ domain within the inverter limits. If, for instance, the reference vector is placed in between two vectors (i.e. in one of the six sections in *Figure 6.4*) in $\alpha\beta$ the inverter will switch between the two bounding vectors and the zero voltage vectors (V_0, V_7) in order to satisfy both position and amplitude at any instant. The order in which the different vectors are placed in a switching period defines different SVM techniques; with respect to the different implementations described in [30], the one implemented in this work is named Synchronous PWM (SYPWM), in which, for each switching period the zero voltage vectors (V_0, V_7) are applied for te same amount of time. Furthermore, the position of the zero voltage vectors is decided so that the minimum amount of commutations is needed in a switching period.
The SVM technique described before is implemented in a MATLAB® function linked to the Simulink® model that represents the drive system. The PI controllers operate in the dq domain and therefore the reference dq voltage coming out of the current controllers is transformed according to (D.4) to define the reference vector in $\alpha\beta$.
The inverter output is given directly in the three-phase time domain, and hence, given as an input to the state space model of the PMSM (5.23). From the motor model the resulting output currents are transformed in the dq domain by means of (D.5) and sent as a feedback for the PI controllers.

6.3.1 Simulation Results of the PMSM Drive System

The simulation was performed under the same condition as for the BLDC drive i.e. giving a reference speed of $2500[rpm]$ and a reference torque of $0.2[Nm]$ at around $0.12[s]$.
The simulation without additional inductors does not give reasonable results if the transformed output currents are given directly as a feedback. It has been noticed that filtering the signal with a low-pass filter tuned around the switching frequency solves the problem. Therefore the Starting problem can be explained as it follows:

"the fast current variation due to the low time constant of the motor makes the current varying very quickly when a chopped signal, such as the output voltage of an inverter is considered as a supply voltage. Under this conditions, having a fast current controller leads to an inherent instability. The fast current variation is detected by the controller, which sets a new reference voltage for the following switching period at the power inverter; this new reference is such that the system should recover from the previous fast variation, and therefore at the next switching state the current varies even faster on the other direction causing instability."

As a matter of fact, the addition of a low pass filter in the current feedback, makes the model resembling more a real case in which the current sensors, along with the analogue to digital converter are characterized by a certain bandwidth and sampling time respectively. This inherent behaviour can be approximated as a low-pass filter.

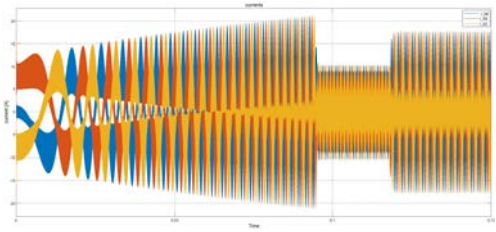

(a) Three-phase current waveform,

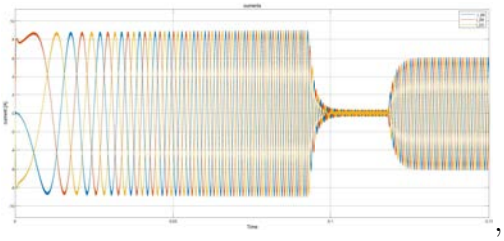

(b) Three-phase current waveform with additional inductors

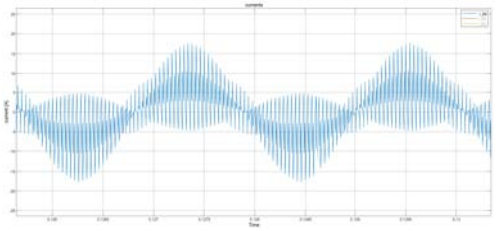

(c) Phase current in steady state condition

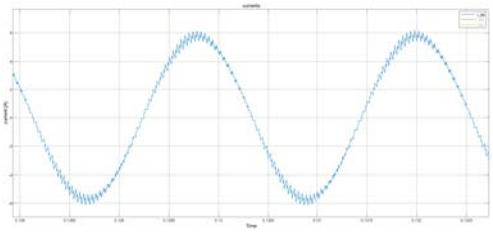

(d) Phase current in steady state condition with additional inductors,,

Figure 6.6: *Current waveforms with and without additional inductors*

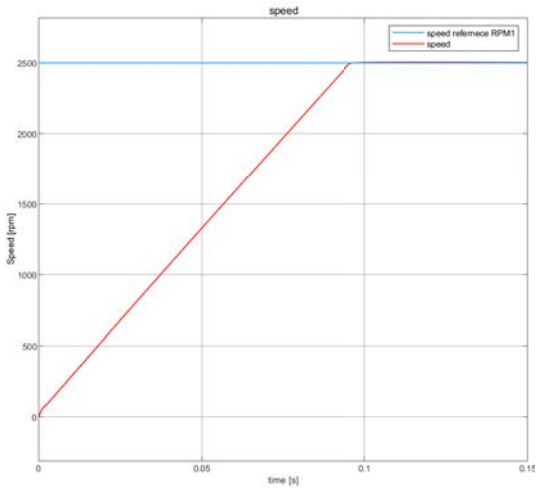

Figure 6.5: *Speed response*

In *Figure 6.5* the speed profile followed by the motor, when the input step reference is applied, is shown; the current waveforms resulting from this dynamic are depicted in *Figure 6.6*. From the latter one, the improvement in terms of harmonic content given by the additional inductors filtering effect, is remarkable. Even though, the additional inductance value was not optimized for this case study, it must be pointed out that this solution might not be applicable in those applications where a low volume and light-weight solution is of paramount importance.
As a comparison between the BLDC trapezoidal control, and the sinusoidal control of a PMSM, it can be noted that the torque ripple without and with additional inductors tends to be notably lower under sinusoidal control

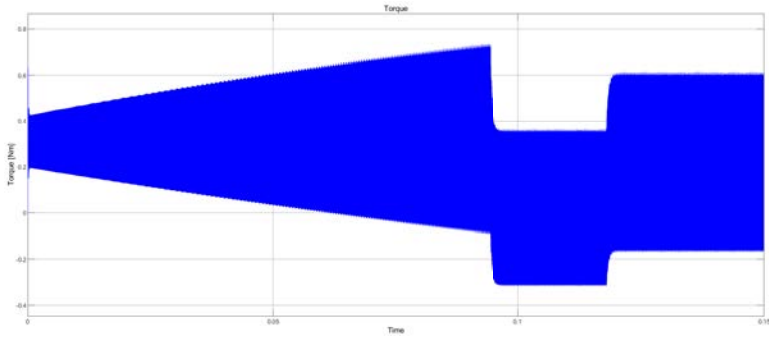

(a) Resulting torque,

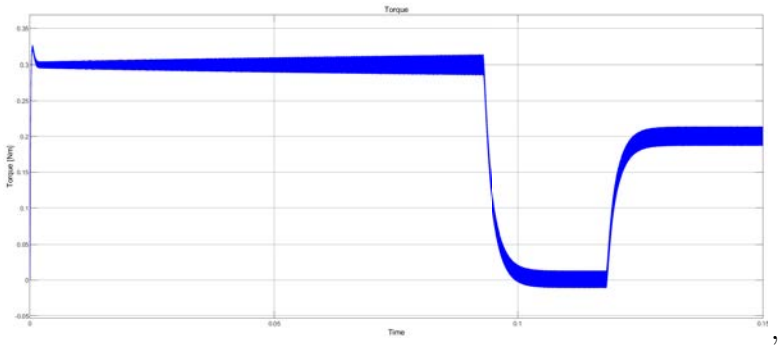

,

(b) Resulting torque with additional inductors

Figure 6.7: *Torque profiles with and without additional inductors*

Results Post-processing

A further code has been developed to work in series with the previous Simulink® model, in order to make the results useful for the application discussed in 7.
The aforementioned code, starts with some data that needs to be stored when the Simulink® simulation is completed, and performs a Fourier analysis (which was conveniently adapted) of the output current in steady state conditions (e.g.*Figure 6.6c* or *Figure 6.6d*). One of the results that are obtained from this analysis is the Total Harmonic Distortion (THD) of the current given as an input.
The THD is defined as:

$$THD = \sqrt{\frac{\sum_h I_h^2 - I_1^2}{I_1^2}} \quad \Rightarrow \quad THD^2 = \frac{\sum_h I_h^2}{I_1^2} - 1 \tag{6.17}$$

The latter equation can be used to compute the increase in the conduction losses due to a certain THD as:

$$\frac{P_h}{P_1} = \frac{\sum_h I_h^2}{I_1^2} = THD^2 + 1 \tag{6.18}$$

the trend of the latter function is shown in *Figure 6.8*.

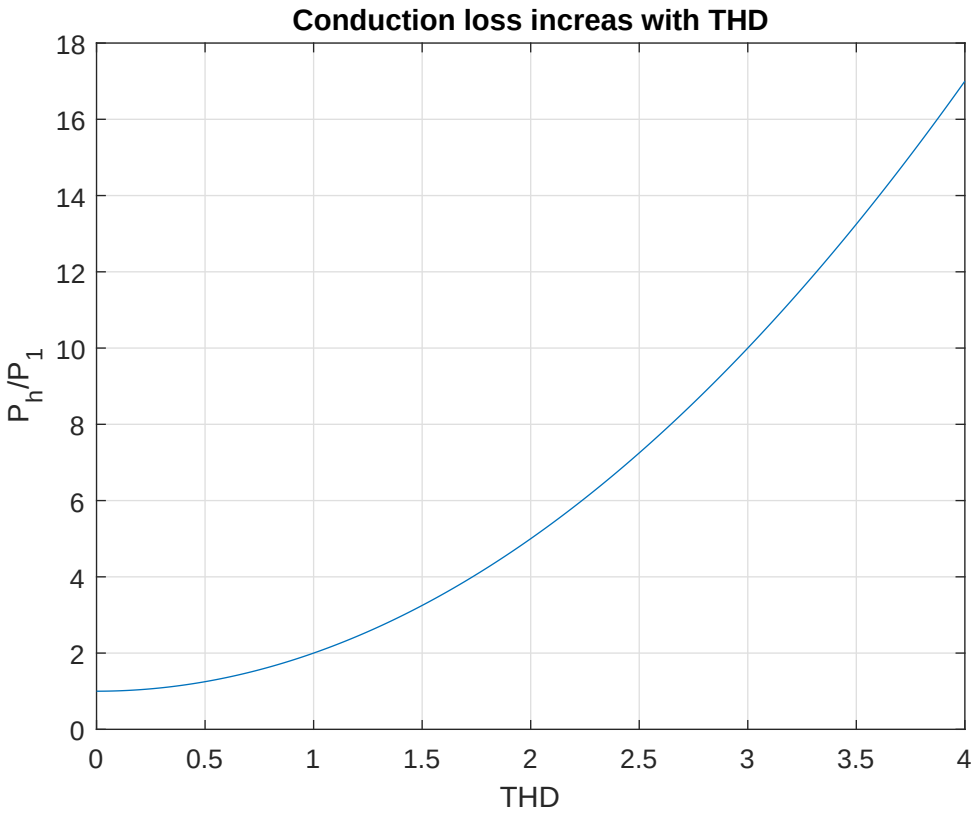

Figure 6.8: *Conduction loss increase with the harmonic content*

The harmonic analysis applied to the waveform shown in *Figure 6.6c* brought to $THD = 1$, which means (according to *Figure 6.8*) that the conduction losses are doubled with respect to a case with sinusoidal current.

Chapter 7

Finite Element Loss Analysis With non-Sinusoidal Current

The aim of this chapter is to present a possible procedure for estimating the speed dependent losses in an electrical machine by means of a FEA when the current given as a source for the coil domains is not sinusoidal. The approach resembles the so called "Circuit-coupled FEA" implemented in some commercial software, where the FE model of any kind of electrical machine or device, is connected to a circuit problem. The solution of the circuit is dependent on the finite element model itself being it either the load or part of it. In [25] a thorough loss analysis is performed by means of a circuit-coupled FE analysis; however the high computational cost is also highlighted, claiming up to 80 hours needed for a loss analysis at 37 kHz switching frequency.
It is worth to point out the fact the analysis of electromagnetic losses by means of a FE code, considering the impact of the switching behaviour on the current waveforms, has an inherently high computational cost; in fact the code should solve a FE problem with a time step which is small enough to catch the minimum current variation, and therefore, the higher the switching frequency, the higher the time needed for the loss analysis. For this reason the implementation of analytical models for the loss prediction (such as [10]) could be more suitable for this purpose.
The method proposed in this work takes advantage of the implementation suggested in [20] where the speed dependent electromagnetic losses in a SPM motor are estimated by means of FEMM.
The code has been conveniently adapted to work with both the portion of machine shown in *Figure 4.1b* and with the output current from the Simulink® model as a source of the stator coil domains. Some indications regarding the theory behind the operation of this code are addressed in the following:

Main Idea:

The code aims to control the FE analysis in order to solve the problem according to a time-stepping (temporal discretization) procedure. The current waveform (as a result from the Simulink® model) is conveniently post-processed in order to define the highly distorted three-phase current waveforms. In this step the Simulink® output itself is conveniently resampled in order to have the minimum amount of samples needed to keep

the original harmonic content. At this point the time distance between two samples in the rebuilt current waveform, defines the time step required for the FEA. This time step corresponds to an angle of which the rotor is rotate at each step.
For any rotor position, the equivalent current sample of the three currents is set as a source of the stator winding. It is worth to point out that the initial rotor position and stator currents are such that for the whole simulation the fundamental stator field is directed along the q-axis (ensuring a MTPA control).
The FE model is solved for any rotor position as a magnetostatic problem and the solution for each time step in each mesh element is conveniently stored.
The loss analysis is entirely developed as a post-processing procedure. In this phase, the different solutions in each element of the mesh are treated as a time varying function; the Fourier analysis such a solution is performed in order to develop the following loss analyses.

Magnet Loss:

The existence of high frequency harmonics in the current waveforms introduces harmonics fields in the air-gap that rotates asynchronously and/or in the different direction with respect to the rotor rotation. In this context, according to the Maxwell-Faraday equation:

$$\begin{gathered}\nabla \times \mathbf{E} = -\frac{\partial \mathbf{B}}{\partial t} = -\frac{\partial}{\partial t}(\nabla \times \mathbf{A}) = \nabla \times (-\frac{\partial \mathbf{A}}{\partial t}) \\ \Downarrow \\ \mathbf{J} = \sigma_m \mathbf{E} = -\sigma_m \frac{\partial \mathbf{A}}{\partial t}\end{gathered} \tag{7.1}$$

the current density $\mathbf{J}$ in the magnets can be found as the time derivative of the magnetic vector potential $\mathbf{A}$ multiplied by the conductivity of the magnet material (set to $0.625 \cdot 10^6$ for NdFeB magnets). In a 2D magnetic problem the magnetic vector potential holds only the z component (orthogonal to the working plane), and so does the current density. Having the all harmonics fro the post-processing allows to define the current density for each harmonic in each element belonging to the magnets as:

$$J_m = -\sigma_m j\omega A - J_c \tag{7.2}$$

where J_c is the average current flowing through the magnet for each harmonic; its contribution to the expression ensures that the net current flowing through the magnet is zero. At this point J_m is a matrix with a number of rows decided by the number of harmonics (h_max) and number of columns given by the number of elements (N_{elem}) defined in the mesh; and therefore, the total losses in the magnets can be computed as:

$$P_{mag} = \frac{1}{2}\sigma_m \sum_{n=1}^{N_{elem}} vol_n \sum_{k=0}^{h_{max}} (\omega_k^2 \cdot J_m^2(n,k))$$

where vol_n is the volume of the n-th element and ω_k the frequency of the k-th harmonic

Iron Losses

The prototype considered in this work makes use of non laminated iron on both sides; this design choice is coherent with the fact that the iron itself is rotating synchronously with the main magnetic field and thus the losses would be negligible if the stator current was perfectly sinusoidal. However, also in this case, the harmonic fields existing in the air-gap because of the stator current ripple will lead to iron losses (especially in the inner ring, being it closer to the stator).
For the iron losses estimation the iron core is assumed to be laminated in order to use typical loss data given by laminations manufacturer. It is worth to notice that the method neglects any eddy currents effect in the magnetic field solution; and as long as the iron is not laminated in the real case, then the assumption tends to be quite forced.
The method adopted for the iron loss estimation is addressed in [12] as the "traditional technique". In this case study, the losses are assumed to be split in two terms: the hysteresis loss (P_h) and the eddy current loss (P_{ec}); as it follows:

$$P_{iron} = P_h + P_{ec} = C_h \omega B^2 + C_{ec} \omega^2 B^2 \tag{7.3}$$

the latter equation can be used for each and every the harmonics of the flux density B computed in the post processing.
The loss coefficient C_h and C_{ec} are estimated from the loss data of the M330-50A laminations; in particular from the specific loss data at a given frequency and flux density it was assumed that the hysteresis loss accounts for 75% the total loss data, and the remaining 25% loss is related to the eddy currents term. The estimated coefficient are:

$$\begin{aligned} C_{ec} &= 1.183 \left[\frac{W}{m^3 T^2 H z^2} \right] \\ C_h &= 137.984 \left[\frac{W}{m^3 T^2 H z} \right] \end{aligned} \tag{7.4}$$

7.0.1 Results from the Loss Analysis

The loss analysis has been carried out with respect to the current waveform depicted in *Figure 7.3*; in particular it represents the steady state current of a simulation producing a reference torque of 0.1 [Nm] at 1500 [rpm].
In order for the method to be effective (within its theoretical based limitations), the mesh in which the domain is discretized was quite dense *Figure 8.5b* resulting in a 7397 elements mesh.

The output power used for computing the efficiency is estimated by means of the average torque coming out as a FE result. Remembering that the current given as an

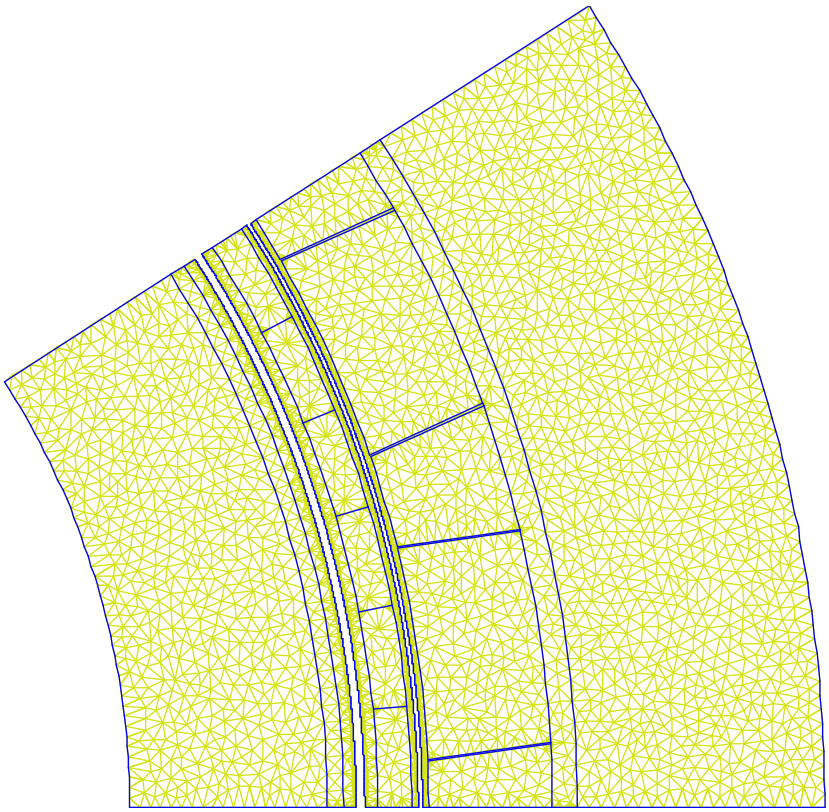

Figure 7.1: *Detail of the mesh adopted for the simulation*

input for the FEM, is the one coming out from the Simulink® model when a reference torque of 0.1 [Nm] is assigned, by looking at the torque result from the FEA *Figure 7.2* it can be noticed how the FE representation resembles the Simulink® one (which is based on measured parameters), this is useful to prove the validity of the two models.

The loss analysis has been performed as explained beforehand. The frequency related to each harmonic was then considered to be proportional with the speed; in this way representing the losses versus the mechanical speed of *Figure 7.4* was possible. It is worth to notice that the latter representation considers the harmonic content of the time varying quantities, moving up in frequency with the speed; however by increasing the speed the current harmonics are fixed around the switching frequency, this means that the harmonic order of the current harmonics diminishes with the increase of the speed; it is also true that the amplitude of the harmonics would tend to increase with the speed as well (because of the higher impact of the back-emf). Therefore, it it has been proved that the losses *Figure 7.4* and the efficiency *Figure 7.3* would not look much different from the ones shown. From the loss figure it can be noted how iron and magnets losses overtake the conduction losses already at 2000 [rpm]

The efficiency is depicted in *Figure 7.5* as a comparison between a loss analysis using sinusoidal currents as a FE source and the one using highly distorted current waveform; in both the cases the output torque is the same.

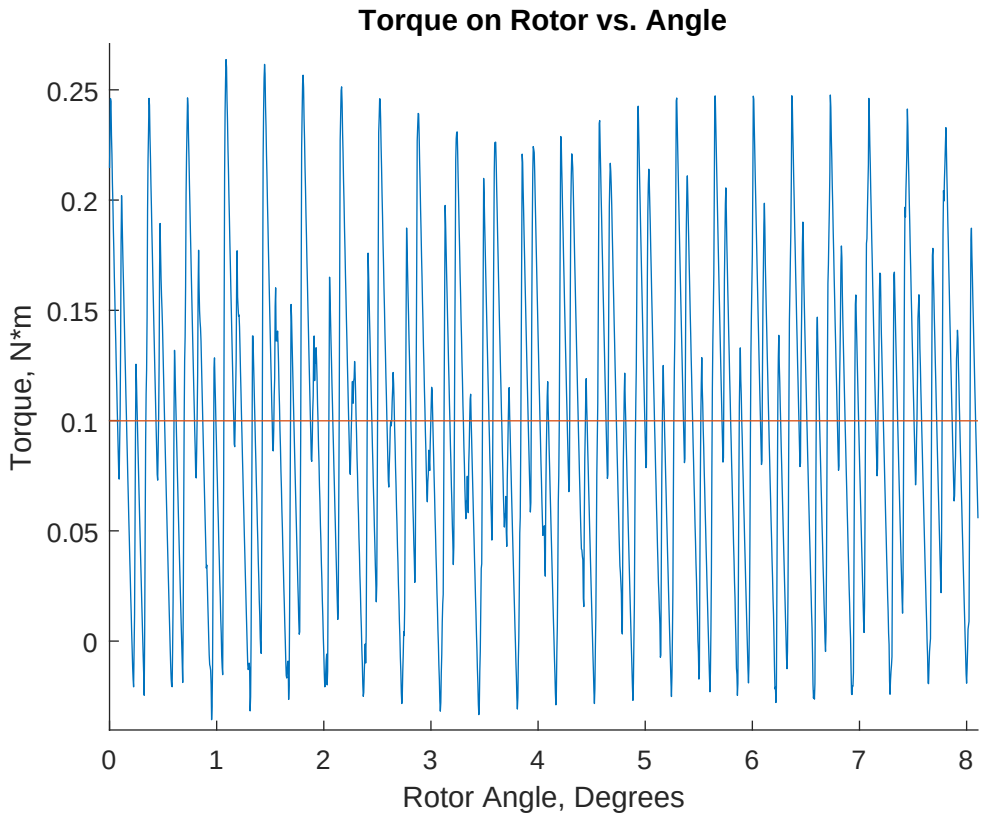

Figure 7.2: *Torque from FEA with distorted current*

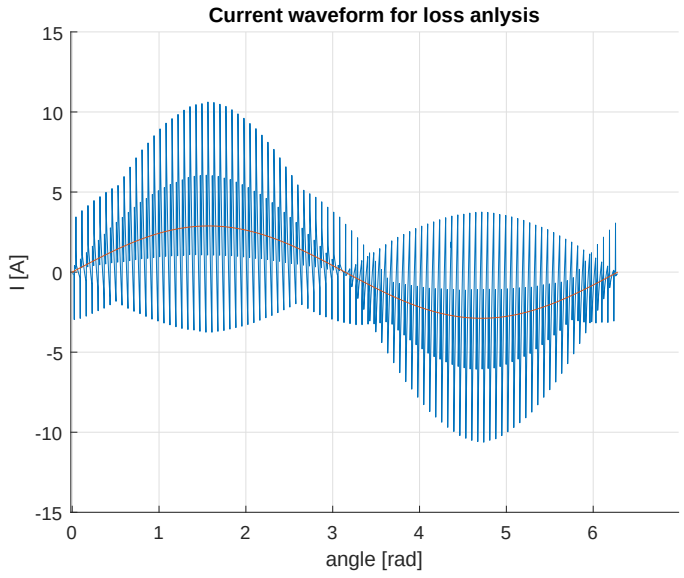

Figure 7.3: *Output current from Simulink® used for the FE analysis -*

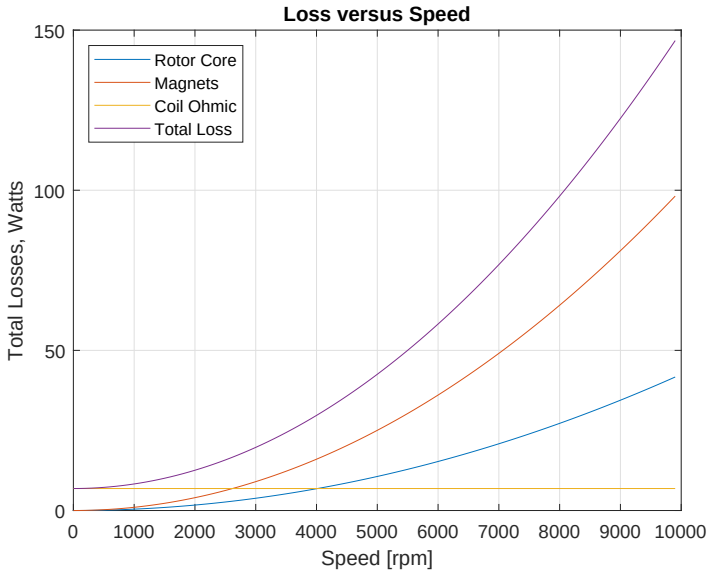

Figure 7.4: *Variable speed losses with high ripple current source*

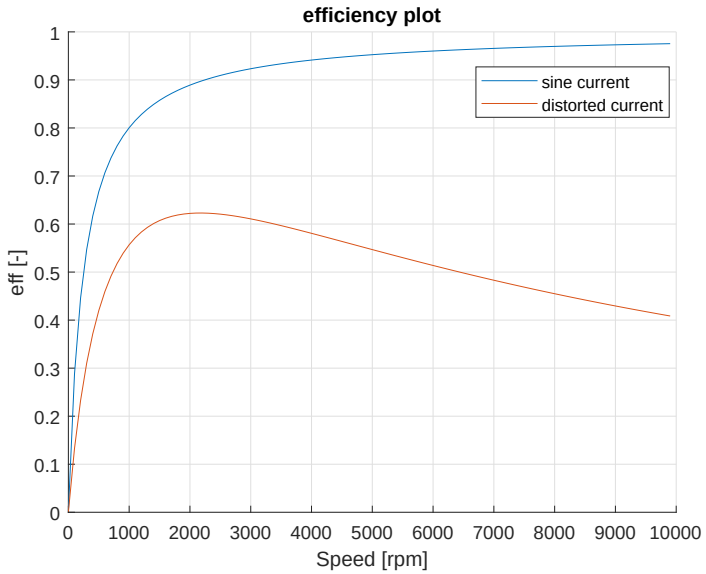

Figure 7.5: *Efficiency comparison with sinusoidal and distorted current source*

Chapter 8

Experimental Validation

The test-bench adopted for the experimental validation is shown in *Figure 8.1*. The simulated load condition is represented as it follows:

- The motor in the upper right (*Figure 8.1*) is is a brushed DC motor controlled as a brake to maintain a speed, which is varied along the measurement phase. This means that mechanical losses are all in charge of the brake motor.
- The brake motor is connected to the prototype by means of a belt-pulley system with 1:3 gear ratio. Meaning that the tested motor spins at three times higher speed then the brake one.
- The tested prototype motor (left of *Figure 8.1*) is controlled with a 25 kHz switching frequency motor controller in order to maintain a torque of 0.1 [Nm] for the whole experiment

Given the latter operating setup, the absence of a torque transducer led to a torque estimation by means of the torque constant. The latter one was estimated from the back-emf constant (according to (6.7)) measured by means of an oscilloscope, by spinning the motor with the open terminals and measuring the output voltage.
Another information needed for the torque measurement is the fundamental component of the stator current (which is responsible for the average torque production) and this is done by means of a suitable power analyser.

The complete measurement setup is shown in *Figure 8.2*. And the different choices described below:

- The three-phase input power to the motor is measured by means of a power analyser (WT1800). The 5 MHz bandwidth of this instrument ensures an accurate power measurement, also under the highly distorted operating condition of the electrical quantities, related to this case study. The embedded harmonic analysis of the input signals allows the measurement of the fundamental current directly from the instrument. The letter information is used in order to keep the torque at a fixed value for the whole measurement process. The inductance of each wire

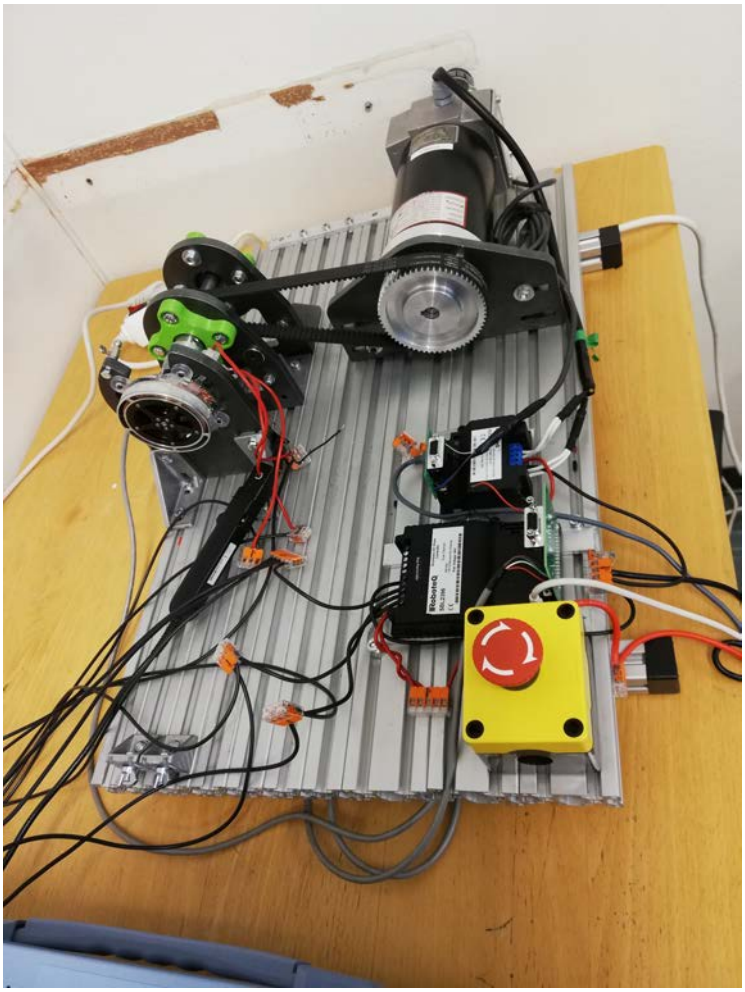

Figure 8.1: *Test-bench setup*

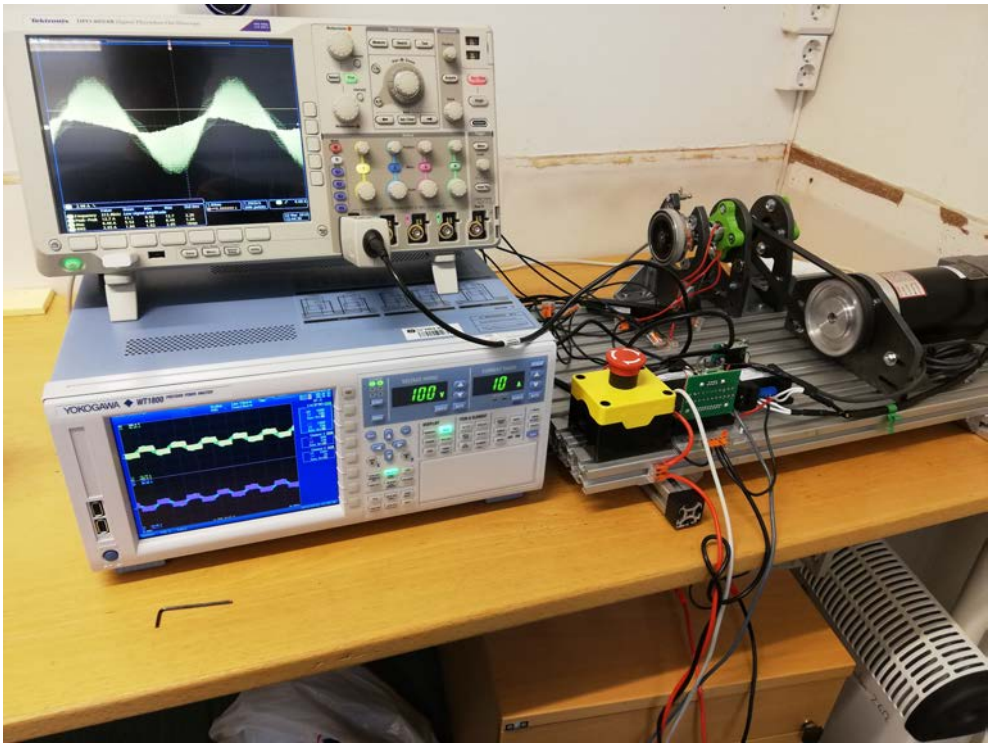

Figure 8.2: *Test-bench setup*

connecting the motor to the power inverter, passing through the power analyser, was measured by means of an LCR-meter which gave an inductance value of about 1 [μH] per wire (the wire length was around 65 [cm]). For this reason the phase inductance in the models was conveniently increased in order to account for these connections.
Even though for the three-phase power measurement of a three wire system only two currents are needed, the third phase was also connected to a current input channel of the power analyser for balancing the system.
As a matter of fact, the third current assumed a paramount importance in the power measurement phase without additional inductors. In fact the power analyser needs a stable and smooth signal to be taken as a reference for all the internal measurements; particularly important, is the frequency of the signal to be measured (which is used for both power and harmonic measurements). The latter information was not detected, at all, if the input signals were to be processed (internally in the instrument) including all the harmonic content; for this reason the third current was only used as a synchronisation source for the measurement by means of embedded filtering features applied only to that channel.

- An oscilloscope (DPO 4054B) was also used, along with a current probe (P6021) with the aim of visualising the current waveform to be compared with models results. The 60 [MHz] bandwidth of the current probe ensured a fairly perfect current visualisation

The power measurements were taken from the power analyser, along with the RMS value of the fundamental current used to compute the output torque. The electrical frequency was also measured from the power analyser to estimate the mechanical speed.

Figure 8.3: *Additional inductors*

This procedure was performed for both cases (with and without additional inductors) at speed steps of some 300 [rpm] up to 2400[rpm] the upper limit was mainly due to system control instability on the motor side when operating without additional inductors. The efficiency results are graphically depicted in *Figure 8.4*, along with the model results in the same speed range for a comparison. The results with additional inductors shows a slight overestimation of the efficiency with the method proposed. This might be due to additional losses not considered in the model such as additional conduction losses due to wires and connections in the test-setup.
On the other hand one would expect a higher difference in the results without additional inductors given the fact that any sort proximity effect loss in the winding is neglected. Considering that the experimental validation does not consider any method for separating the different loss sources it gets hard to say in which direction the method is overestimating the losses; a possible assumption (if any source of error during the measurement phase is neglected) could be related to the fact that, even though the model is assuming a laminated iron core, the physics behind the iron losses under non sinusoidal excitation is much more complicated than just applying the superposition principle assuming all the harmonics as independent sinusoids, and the interaction of the harmonics themselves with the non-linear BH curve of the iron should be considered [1]. This might have led to an overestimation of the losses with the FE model.

As a final verification *Figure 8.5* the current waveforms from the model and from the oscilloscope and from the model with 0.1[Nm] torque reference and 300 [rpm] rotational speed, showing a good correspondence of the results.

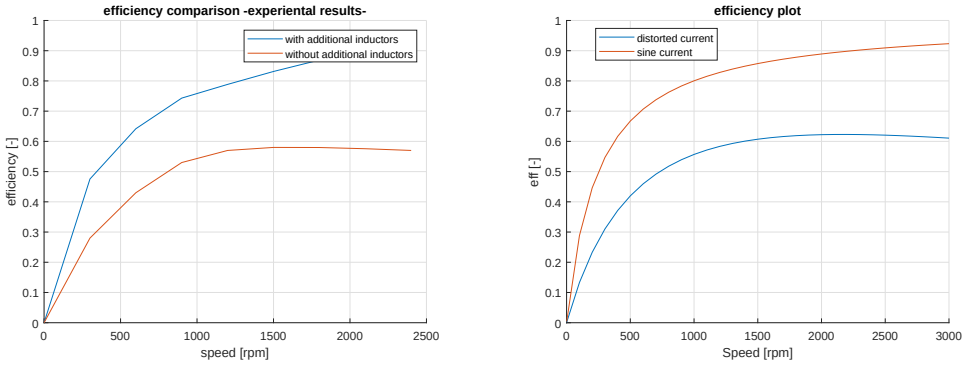

(a) Experimental efficiency results, ***(b)*** Efficiency results from loss model,

Figure 8.4: *Efficiency results comparison*

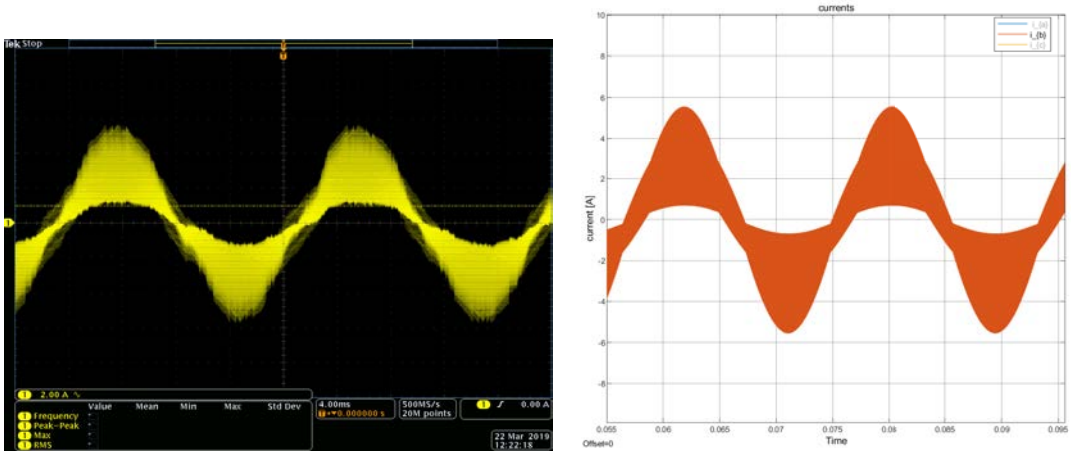

(a) Current waveform at the oscilloscope, ***(b)*** Current from the Simulink® model,

Figure 8.5: *Current waveform comparison*

Chapter 9

Conclusions

In this work two MATLAB-Simulink® implementations for electric drives are proposed in order to compare two widespread control techniques in industrial applications. The simulation results, along with the inherent higher resulting efficiency for the sinusoidal control, make this control algorithm preferable over the trapezoidal one. The latter statement holds as long as all the drawbacks related to the sinusoidal control are considered to be not relevant.
A further step was taken for considering the critical issues related to the control of slotless machines with either one of the two control algorithms. The intrinsic low inductance for this type of machine should be considered already in the design phase of the machine itself, in order to find the most suitable solution for reducing the current ripple when the machine is controlled by means of a power inverter.
The solution adopted in this work was adding inductors in series with each phase of the motor in order to increase the electric time constant; the Simulink® models developed in this work represent a powerful tool for verifying the performance of the drive system also when alternative solutions with respect to the additional inductor one, need to be checked.
The design of the PI controllers based o the Bode plot analysis for both the drive systems is proposed. In this regard it was shown that during mechanical acceleration phase the fact of having fast control algorithm along with a small electric time constant and not high enough switching frequency can lead to a current drift towards high peak values. Such a behaviour should be considered especially when intermittent fast accelerations are needed.
In the last part of the work a method for evaluating the electromagnetic losses in the motor is proposed. The method makes use of a FE analysis coupled indirectly with the Simulink® models; the method gives promising results, and some improvements should be investigated in future works in order to include a proximity loss estimation, which should be able to include the adoption of any type of conductor, the method should also be suitable for high frequency problems as the one described in this work.
The experimental results are provided in the last chapter as a "partial" validation of the model results; a further step would be to develop a system for separating the different loss contributions and carry out thorough comparison between test-rig and computer model.

Acknowledgement

The whole project was conducted in close cooperation with Alva Motor Solutions. This new group did not only offer the prototype, object of this work, but also an environment in which personal growth and development, come as a consequence from the day-to-day work. In particular, I would like to thank Sivert Hatletveit as the main developer of the test-rig used in this work, and the electric team (Kasper Kvinnesland and Ravindra Ummaneni) as a rich source of information for this project.

I am also grateful to the NTNU Department of Electric Power Engineering for having made the measurement equipment available during the testing phase.

A special mention goes to my University (Università degli Studi di Padova) for having made possible in the last years to cultivate my interests and make them growing thanks to the enviable experience which identifies the Department of Industrial Engineering. Furthermore, I would like to thank my supervisor at NTNU Marta Molinas for her remarkable willingness and support offered during this project.

Finally, last but not least, I am grateful to my family, who supported me in any direction and decision I have taken so far in my life. A special mention goes to my nephew Lorenzo, to whom I dedicate this work, wishing you the best future that this life could ever offer.

Appendix A

Air-gap flux density for surface-mounted permanent magnets

If the magnetic circuit depicted in *Figure 2.3* is considered, the air-gap reluctance and the magnet reluctance can be expressed as:

$$\mathcal{R}_m = \frac{t_m}{\mu_{rec} \cdot \mu_0 \cdot S_m} \quad , \quad \mathcal{R}_g = \frac{g}{\mu_0 \cdot S_g} \tag{A.1}$$

where S_m and S_g are respectively the magnet and the air-gap surfaces, μ_{rec} is the relative permeability of the magnet on the operating condition and t_m and g are respectively the magnet and air-gap thicknesses. The air gap flux can then be computed as:

$$\begin{aligned} \Phi_g = B_g \cdot S_g = \Phi_{rem} \cdot \frac{\mathcal{R}_m}{\mathcal{R}_m + \mathcal{R}_g} &= B_{rem} \cdot S_m \cdot \frac{\frac{t_m}{\mu_{rec} \cdot \mu_0 \cdot S_m}}{\frac{t_m}{\mu_{rec} \cdot \mu_0 \cdot S_m} + \frac{g}{\mu_0 \cdot S_g}} \\ &= B_{rem} \cdot \frac{1}{\frac{g \cdot \mu_{rec}}{t_m \cdot S_g} + \frac{1}{S_m}} \end{aligned} \tag{A.2}$$

where B_{rem} is the remanent flux density of the magnet.
Therefore, the air gap flux density (maximum value of the blue waveform shown in *Figure 6.1*) results to be:

$$B_g = \frac{B_{rem}}{\frac{S_g}{S_m} + \mu_{rec} \frac{g}{tm}} \tag{A.3}$$

Appendix B

Air-gap flux density for Halbach array arrangement

In *Figure B.1* the resulting flux lines from a FE simulation of a single pole of the tested machine under no load condition is shown. The same section, is considered to build a magnetic network for the air-gap flux density estimation; specifically, the section considers a tangentially magnetised magnet, and the two halves of the radial magnets located on its sides.

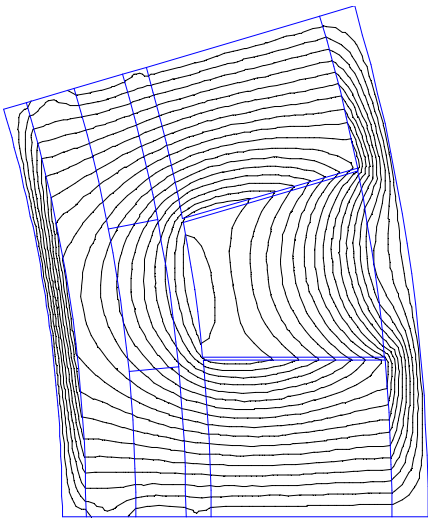

Figure B.1: *Flux density map over a pole*

The flux density map *Figure B.1* can be translated into the equivalent magnetic network depicted in *Figure B.2*; where: $\mathcal{R}_g$ is the air-gap reluctance considering the series of the reluctances of the two air-gaps and the winding over half a pole;$\mathcal{R}_L$ is the leakage reluctance considering those flux lines that are not crossing the stator; $\mathcal{R}_{m,r}$ and $\mathcal{R}_{m,t}$ are respectively the reluctance of half the radial magnet and the tangential magnet. In particular, it is assumed that the useful flux crossing the stator is the one coming out radially from the radial magnet (so that the air-gap reluctance is computed with respect to the radial magnet surface), and the leakage reluctance consider the flux path above the tangential magnet up to the middle of the stator; furthermore the

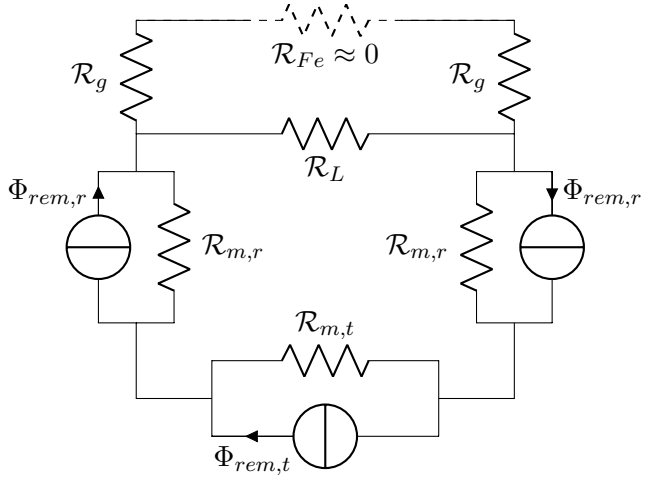

Figure B.2: *Equivalent network for a Halbach array*

magnets are assumed to span fixed angle with respect t the radial coordinate which is set as the average angle with respect to the real configuration (65% of the pole angle for the radial one and 35% for the tangential one) . Considering all these assumptions, the expressions for the different reluctances can be written as it follows:

$$\mathcal{R}_L = \frac{\pi \cdot \frac{(D_{s,o} + g_o)}{2 \cdot p} \cdot \alpha_t}{\mu_0 \cdot g_o \cdot l_a}$$

$$\mathcal{R}_g = \frac{2 \cdot (g_o + s_t + g_i)}{\mu_0 \cdot \pi \cdot \frac{D_{m,i} - (g_o + s_t + g_i)}{2 \cdot p} \cdot \alpha_r \cdot l_a}$$

$$\mathcal{R}_{m,t} = \frac{\alpha_t \cdot \pi \cdot \frac{D_{m,i}+t_m}{2 \cdot p}}{\mu_0 \cdot t_m \cdot l_a}$$

$$\mathcal{R}_{m,r} = \frac{2 \cdot t_m}{\mu_0 \cdot \pi \cdot \frac{D_{m,i}+t_m}{2 \cdot p} \cdot \alpha_r \cdot l_a}$$

$$\Phi_{rem,r} = B_{rem} \cdot \pi \cdot \alpha_r \cdot \frac{D_{m,i} + t_m}{2 \cdot p} \cdot l_a$$

$$\Phi_{rem,t} = B_{rem} \cdot t_m \cdot l_a$$

where: $D_{s,o}$ is the outer stator diameter, g_o is the outer air-gap thickness, g_i is the inner air-gap thickness, s_t is the stator thickness, t_m is the magnets radial thickness, α_r and α_t are the pole fraction occupied respectively by the radial and the tangential magnets, l_a is the axial length, $D_{m,i}$ is the inner diameter of the magnet ring.
The circuit can be solved according to the superposition principle by keeping only one of the three current sources active at a time. The solution is found by means of a

dedicated code, which receives all the useful data as an input, in order to build the FE model of the motor and solve the circuit. In this way a direct comparison between a FE solution and the circuit solution can validate the latter one.

Appendix C

Clarke transformation

The aim of the *Clarke* transformation is to represent a three-phase time varying quantities ($g_a(t)$,$g_b(t)$,$g_c(t)$) as a vector ($\mathbf{g}(t)$) in a complex reference system (α, β) as shown in *Figure C.1* , according to the following definition:

$$\begin{aligned}\mathbf{g}(t) &= \frac{2}{3}\left[g_a(t) + g_b(t)e^{j\frac{2}{3}\pi} + g_c(t)e^{j\frac{4}{3}\pi}\right] \\ &= g_\alpha(t) + jg_\beta(t) = |\mathbf{g}(t)|e^{j\gamma(t)}\end{aligned} \tag{C.1}$$

Considering the exponential terms in their explicit form:

$$e^{jf} = \cos(f) + j\sin(f) \tag{C.2}$$

Then the two components of the vector from (C.1) can be explicitly written as:

$$\begin{cases} g_\alpha(t) = \frac{2}{3}\left[g_a - \frac{1}{2}g_b - \frac{1}{2}g_c\right] \\ g_\beta(t) = \frac{2}{3}\left[0 + \frac{\sqrt{3}}{2}g_b - \frac{\sqrt{3}}{2}g_b\right] = \frac{1}{\sqrt{3}}[g_b - g_c] \end{cases} \tag{C.3}$$

which is typically written in matrix form as it follows:

$$\begin{bmatrix} g_\alpha(t) \\ g_\beta(t) \end{bmatrix} = \frac{2}{3}\begin{bmatrix} 1 & -\frac{1}{2} & -\frac{1}{2} \\ 0 & \frac{\sqrt{3}}{2} & -\frac{\sqrt{3}}{2} \end{bmatrix}\begin{bmatrix} g_a(t) \\ g_b(t) \\ g_c(t) \end{bmatrix} \tag{C.4}$$

Of particular interest is the case in which the starting system is represented by a three-phase direct and balance system as:

$$\begin{cases} u_a(t) = U_M\cos(\omega t + \theta_0) \\ u_b(t) = U_M\cos(\omega t + \theta_0 - \frac{2}{3}\pi) \\ u_c(t) = U_M\cos(\omega t + \theta_0 + \frac{2}{3}\pi) \end{cases} \tag{C.5}$$

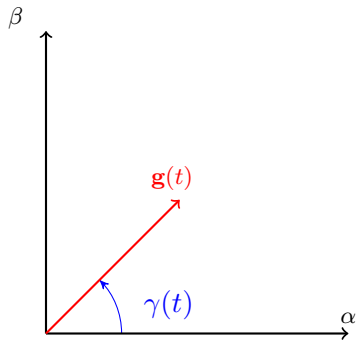

Figure C.1: *Vector definition in the complex domain*

which, by means of (C.4), can be transformed in the $\alpha\beta$ reference frame, giving the following result:

$$\begin{cases} u_\alpha(t) = U_M \cos(\omega t + \theta_0) \\ u_\beta(t) = U_M \sin(\omega t + \theta_0) \end{cases} \quad \Rightarrow \quad \mathbf{u}_{\alpha\beta}(t) = U_M e^{j(\omega t + \theta_0)} \tag{C.6}$$

the resulting vector is rotating at a frequency ω along a circumference of radius U_M in the plane $\alpha\beta$

Appendix D

Park transformation

Differently from the Clarke transformation, the Park transformation aims to represent the three-phase time varying quantities in a reference frame (dq) which is rotating synchronously with respect to the frequency of the original quantities (*Figure D.1*). In this reference frame, the angle θ_{dq} between the dq and $\alpha\beta$ reference frames can be expressed as:

$$\theta_{dq}(t) = \theta_{dq}(0) + \int_0^t \omega_{dq} dt \tag{D.1}$$

Now since the vector $\mathbf{g}(t)$ in the dq reference frame can be generally addressed as:

$$\mathbf{g}_{dq} = |\mathbf{g}| e^{j\gamma_{dq}} \tag{D.2}$$

being: $\gamma_{\alpha\beta} = \gamma_{dq} + \theta_{dq}$; then the vector in the rotating reference frame can be written as:

$$\mathbf{g}_{dq} = |\mathbf{g}| e^{j(\gamma_{\alpha\beta} - \theta_{dq})} = \mathbf{g}_{\alpha\beta} e^{-j\theta_{dq}} \tag{D.3}$$

and vice versa: $\mathbf{g}_{\alpha\beta} = \mathbf{g}_{dq} e^{j\theta_{dq}}$

Also in this case, a matrix form transformation is typically adopted:

$$\begin{bmatrix} g_d(t) \\ g_q(t) \end{bmatrix} = \begin{bmatrix} \cos(\theta_{dq}) & \sin(\theta_{dq}) \\ -\sin(\theta_{dq}) & \cos(\theta_{dq}) \end{bmatrix} \begin{bmatrix} g_\alpha(t) \\ g_\beta(t) \end{bmatrix} \tag{D.4}$$

Furthermore, the direct transformation from the three-phase system to the dq rotating system can be found by combining the two transformations. The resulting trans-

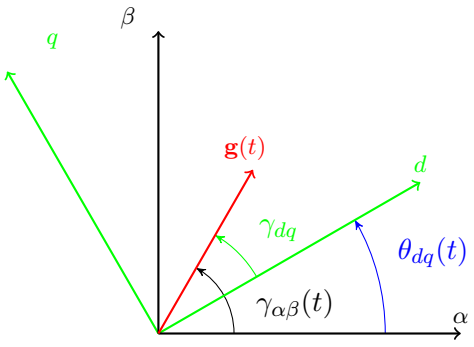

Figure D.1: *Vector definition in the rotating (dq) reference frame*

formation is addressed in matrix form in the following:

$$\begin{bmatrix} g_d(t) \\ g_q(t) \end{bmatrix} = \frac{2}{3} \begin{bmatrix} \cos(\theta_{dq}) & \cos(\theta_{dq} - \frac{2}{3}\pi) & \cos(\theta_{dq} + \frac{2}{3}\pi) \\ -\sin(\theta_{dq}) & -\sin(\theta_{dq} - \frac{2}{3}\pi) & -\sin(\theta_{dq} + \frac{2}{3}\pi) \end{bmatrix} \begin{bmatrix} g_a(t) \\ g_b(t) \\ g_c(t) \end{bmatrix} \tag{D.5}$$

Considering again the case addressed in (C.5) starting from its representation in the fixed reference frame $\alpha\beta$ (**??**), the Park transformation allows to represent the starting system (considering (D.3)) as:

$$\mathbf{g}_{dq}(t) = U_M e^{j\omega t + \theta_0} e^{-j\omega t} = U_M e^{j\theta_0} \tag{D.6}$$

which means that the three-phase system is represented as a fixed vector in the rotating reference system (dq).

Bibliography

[1] MUHAMMAD SOHAIL Ahmed. *Effect of harmonics on iron losses*. PhD thesis, Ph. D. Thesis, Chalmers University of Technology, Göteborg, Sweden, 2007.

[2] Kristina O Armstrong, Sujit Das, and Joe Cresko. Wide bandgap semiconductor opportunities in power electronics. In *2016 IEEE 4th Workshop on Wide Bandgap Power Devices and Applications (WiPDA)*, pages 259–264. IEEE, 2016.

[3] Z Azar, ZQ Zhu, and G Ombach. Influence of electric loading and magnetic saturation on cogging torque, back-emf and torque ripple of pm machines. *IEEE Transactions on Magnetics*, 48(10):2650–2658, 2012.

[4] Stefan Baldursson. Bldc motor modelling and control-a matlab®/simulink® implementation. 2005.

[5] Todd D Batzel and Kwang Y Lee. Slotless permanent magnet synchronous motor operation without a high resolution rotor angle sensor. *IEEE Transactions on energy conversion*, 15(4):366–371, 2000.

[6] Nicola Bianchi and Silverio Bolognani. Design techniques for reducing the cogging torque in surface-mounted pm motors. *IEEE Transactions on industry applications*, 38(5):1259–1265, 2002.

[7] Norman Borchardt and Roland Kasper. Nonlinear design optimization of electric machines by using parametric fourier coefficients of air gap flux density. In *2016 IEEE International Conference on Advanced Intelligent Mechatronics (AIM)*, pages 645–650. IEEE, 2016.

[8] Norman Borchardt and Roland Kasper. Analytical magnetic circuit design optimization of electrical machines with air gap winding using a halbach array. In *2017 IEEE International Electric Machines and Drives Conference (IEMDC)*, pages 1–7. IEEE, 2017.

[9] Jess Brown. Power mosfet basics: Understanding gate charge and using it to assess switching performance. *Vishay Siliconix, AN608*, 2004.

[10] Ping Chen, Renyuan Tang, Wenming Tong, Xueyan Han, Jianguo Jia, and Xiaofeng Zhu. Analysis of losses of permanent magnet synchronous motor with pwm supply. In *2014 17th International Conference on Electrical Machines and Systems (ICEMS)*, pages 1119–1124. IEEE, 2014.

[11] Stijn Derammelaere, Michiel Haemers, Jasper De Viaene, Florian Verbelen, and Kurt Stockman. A quantitative comparison between bldc, pmsm, brushed dc and

stepping motor technologies. In *2016 19th International Conference on Electrical Machines and Systems (ICEMS)*, pages 1–5. Ieee, 2016.

[12] Emad Dlala. Comparison of models for estimating magnetic core losses in electrical machines using the finite-element method. *IEEE Transactions on Magnetics*, 45(2):716–725, 2009.

[13] George P Gogue and JJJ Stupak. Theory and practice of electromagnetic design of dc motors and actuators. *Oregon, USA: G2 Consulting*, 1993.

[14] Ingenia. Everest xcr, 2018.

[15] MG Jayne, SR Bowes, and BM Bird. Developments in sinusoidal pwm inverters. In *Control in Power Electronics and Electrical Drives*, pages 145–154. Elsevier, 1978.

[16] Ping Jin, Yue Yuan, Heyun Lin, Shuhua Fang, and SL Ho. General analytical method for magnetic field analysis of halbach magnet arrays based on magnetic scalar potential. *Journal of Magnetics*, 18(2):95–104, 2013.

[17] Achim Kampker, Peter Burggräf, and Carsten Nee. Costs, quality and scalability: Impact on the value chain of electric engine production. In *2012 2nd International Electric Drives Production Conference (EDPC)*, pages 1–6. IEEE, 2012.

[18] Ramu Krishnan. *Permanent magnet synchronous and brushless DC motor drives*. CRC press, 2009.

[19] Parag Kshirsagar and R Krishnan. Efficiency improvement evaluation of non-sinusoidal back-emf pmsm machines using field oriented current harmonic injection strategy. In *2010 IEEE Energy Conversion Congress and Exposition*, pages 471–478. IEEE, 2010.

[20] DC Meeker. Rotating losses in a surface mount permanent magnet motor, 2017.

[21] Mirjana Milosevic. Decoupling control of d and q current components in three-phase voltage source inverter. In *Power Systems Conference and Exposition (PSCE)*. Citeseer, 2003.

[22] Ned Mohan and Tore M Undeland. *Power electronics: converters, applications, and design*. John wiley & sons, 2007.

[23] Yuancheng Ren, Ming Xu, Jinghai Zhou, and Fred C Lee. Analytical loss model of power mosfet. *IEEE transactions on power electronics*, 21(2):310–319, 2006.

[24] K Sakai, Y Tabuchi, and T Washizu. Structure and characteristics of new high speed machines with two or three rotor discs. In *Conference Record of the 1993 IEEE Industry Applications Conference Twenty-Eighth IAS Annual Meeting*, pages 19–26. IEEE, 1993.

[25] Athanasios G Sarigiannidis and Antonios G Kladas. Switching frequency impact on permanent magnet motors drive system for electric actuation applications. *IEEE Transactions on Magnetics*, 51(3):1–4, 2015.

[26] Keiji Wada and Kent Taguri. Switching-frequency limitations of a three-phase pwm inverter using si-mosfets and sic-sbds. In *CIPS 2014; 8th International Conference on Integrated Power Electronics Systems*, pages 1–5. VDE, 2014.

[27] Xing Hua Wang, Ming Hui Li, Xin Yi Zhang, Yu Chen, and Cheng Hui Zhang. The calculation of winding inductance in slotless permanent magnet brushless dc motor. In *Advanced Materials Research*, volume 694, pages 1537–1540. Trans Tech Publ, 2013.

[28] Nuan Wen, Zhenghua Liu, Fang Zhang, and Yan Ren. Dynamic tracking performance of servo mechanisms based on compound controller. *Advances in Mechanical Engineering*, 8(10):1687814016671443, 2016.

[29] Changliang Xia, Liyan Guo, and Huimin Wang. Modeling and analyzing of magnetic field of segmented halbach array permanent magnet machine considering gap between segments. *IEEE Transactions on Magnetics*, 50(12):1–9, 2014.

[30] Keliang Zhou and Danwei Wang. Relationship between space-vector modulation and three-phase carrier-based pwm: a comprehensive analysis [three-phase inverters]. *IEEE transactions on industrial electronics*, 49(1):186–196, 2002.